UNIVERSITY OF CALIFORNIA,
IRVINE

Performance and Simulation of the ARIANNA Pilot Array, with Implications for Future Ultra-high Energy Neutrino Astronomy

DISSERTATION

submitted in partial satisfaction of the requirements
for the degree of

DOCTOR OF PHILOSOPHY

in Physics

by

Christopher Robert Persichilli

Dissertation Committee:
Professor Steven Barwick, Chair
Professor Stuart Kleinfelder
Professor Gaurang Yodh

2018

DEDICATION

To Lizz, for being at my side through all the most challenging and rewarding moments of my life. I love you, and am looking forward to the day when I can be home with you for Thanksgiving; instead of in a tent on a sea of ice, eating defrosted deli meat.

TABLE OF CONTENTS

LIST OF FIGURES

LIST OF TABLES

ACKNOWLEDGMENTS

It is my honor to present this work, which is built off of the cumulative effort of individuals too numerous to mention.

Firstly I must thank all the outstanding men and women of the United States Antarctic Program, without whose incomparable support the scientific mission in Antarctica would simply not be possible. Such achievements belong to you, just as much as us beakers.

I also wish to thank all of my companions during my last 4 years of Antarctic field seasons: Steve Barwick, Corey Reed, Joilien Tatar, James Walker, Anna Nelles, Hans Bernhoff, Lisa Unger, Shih-Hao Wang, and Geoffrey Gaswint. Thanks for braving the cold and the wind and snow with me, to help make the HRA a reality.

A particular thanks to my advisor and mentor Professor Steve Barwick. Thanks for supporting me when I sometimes faltered, and for trusting me with responsibilities that allowed me to grow in ways I would never have thought I could.

This work was supported by the United States National Science Foundation under grant # NSF-1607719. I would also like to thank the UCI Chancellor's Club, for their generous support through the Chancellor's Club Fellowship, which recognizes the contributions of first generation college students and was of tremendous financial relief during the final months of writing this dissertation.

CURRICULUM VITAE

Christopher Robert Persichilli

EDUCATION

Doctor of Philosophy in Physics — **2018**
University of California, Irvine — *Irvine, California*

Master of Science in Physics — **2013**
Rensselaer Polytechnic Institute — *Troy, New York*

Bachelor of Science in Physics — **2010**
Rensselaer Polytechnic Institute — *Troy, New York*

RESEARCH EXPERIENCE

Graduate Research Assistant — **2013–2018**
University of California, Irvine — *Irvine, California*

Masters Research Project — **2011–2013**
Rensselaer Polytechnic Institute — *Troy, New York*

Undergraduate Research Project — **Fall 2010**
Rensselaer Polytechnic Institute — *Troy, New York*

NSF Summer REU — **Summer 2010**
University of South Florida — *Tampa, Florida*

TEACHING EXPERIENCE

Competitive Edge Program Mentor — **Summer 2017**
University of California, Irvine — *Irvine, California*

Teaching Assistant — **2013–2014 & Winter 2016**
University of California, Irvine — *Irvine, California*

Teaching Assistant — **2011–2013**
Rensselaer Polytechnic Institute — *Troy, New York*

CONTRIBUTIONS to REFEREED JOURNAL PUBLICATIONS

Observation of classically forbidden electromagnetic wave propagation and implications for neutrino detection **2018**
Journal of Cosmology and Astroparticle Physics

Radio detection of air showers with the ARIANNA experiment on the ross ice shelf **2017**
Astroparticle Physics

A first search for cosmogenic neutrinos with the ARIANNA hexagonal radio array **2015**
Astroparticle Physics

Structural fingerprints and their evolution during oligomeric vs. oligomer-free amyloid fibril growth **2013**
The Journal of Physical Chemistry

CONFERENCE PUBLICATIONS

Radio search for EHE neutrinos with the ARIANNA pilot array, and ARIANNA performance projections **2017**
Proceedings of the International Cosmic Ray Conference

Livetime and sensitivity of the ARIANNA hexagonal radio array **2015**
Proceedings of the International Cosmic Ray Conference

TALKS

The ARIANNA detector **2017**
Talk Presented at TeVPA, Columbus, Ohio

ARIANNA: A new way to do astronomy using neutrinos and antarctic ice **2017**
Talk presented at the UCI AGS Graduate Research Symposium, Irvine, California

ARIANNA: Searching for neutrinos and finding cosmic rays. **2015**
Talk Presented at the Computing in High-Energy AstroParticle Research (CHEAPR) workshop, Columbus, Ohio

Does thioflavin-t detect oligomers formed during amyloid fibril assembly **2011**
Talk presented at the APS March Meeting, Dallas, TX

ABSTRACT OF THE DISSERTATION

Performance and Simulation of the ARIANNA Pilot Array, with Implications for Future Ultra-high Energy Neutrino Astronomy

By

Christopher Robert Persichilli

Doctor of Philosophy in Physics

University of California, Irvine, 2018

Professor Steven Barwick, Chair

The ARIANNA pilot Hexagonal Radio Array (HRA), a seven station test-bed for the development of an ultra-high energy (UHE) neutrino telescope, using Antarctica's Ross Ice Shelf as a detector, was completed during the 2014-2015 Antarctic summer season. In the more than three years since, the HRA has demonstrated remarkable resilience and stability, operating with a typical 90% uptime during the summer months using solar energy, and surviving multiple Antarctic winters. Novel wind turbine design has, for the first time, enabled the operation of an autonomous station in Moore's Bay over winter. The ARIANNA data acquisition system, built on the Synchronous Sampling plus Triggering (SST) circuitry developed at UCI, has proven to be capable and cost/power efficient. Beyond the HRA, hardware research and development has been ongoing, with a new revision of the SST system seeing service in a variety of specialized stations. Dedicated cosmic ray stations have successfully self-triggered and measured the flux of UHE cosmic ray air showers in broadband radio frequencies, which serves as an important calibration source for the neutrino analysis. In an international collaboration with the National Taiwan University, the ARIANNA Horizontal Cosmic Ray station, designed to measure air showers resulting from the interaction of ν_τ in the surrounding mountains, was deployed and deployed.

The sensitivity of this fully autonomous array was simulated using the *ShelfMC* Monte Carlo, which has been developed to version 2.0, with significant improvements to accuracy and flexibility. A prototype analysis is presented which achieves 84.63% analysis efficiency while rejecting all measured non-cosmic ray backgrounds over a 1.5 year dataset for all HRA stations. The actualized livetime of 145 days per year per station is used to to construct a 5 year projection for an array of 300 ARIANNA stations. Results indicate that reasonable optimizations will allow such an array to probe or measure all but the most pessimistic models of the GZK neutrino flux. Lessons learned from the deployment and operation of the HRA will inform the design of the next generation of UHE radio neutrino detectors, which will provide insight into long standing questions on the nature and origin of the Universe's highest energy particles.

Chapter 1

Introduction

1.1 Cosmic Rays & The Motivation for Neutrino Astronomy

Despite decades of investigation and tremendous progress in the detection of cosmic rays, the sources of ultra high energy cosmic rays (UHECRs), which can have energies in excess of 10^{20} eV, remain largely enigmatic. The capacity to accelerate protons to ultra-high energies is determined by a product of the magnetic field strength and the distance over which the particles can be accelerated. A variety of known objects, ranging over 20 orders of magnitude in size, could serve as the sources of the most energetic cosmic rays (see Figure 1.1). Determining which (or which combination) of these possible candidates is the source of the measured UHECR flux is at the heart of one of the most fundamental unsolved problems in astronomy.

Charged cosmic rays face several drawbacks as a cosmic messenger. UHECRs with energies in excess of 10^{20} eV interact with the cosmic microwave background through a Δ resonance (the

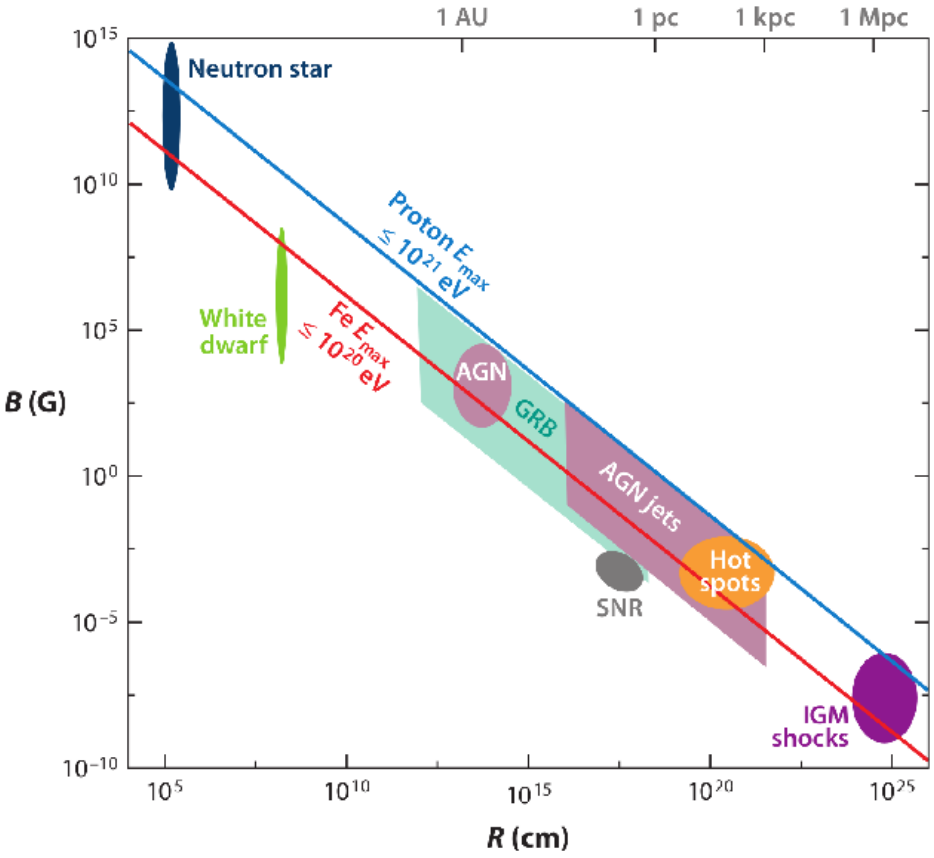

Figure 1.1: Hillas diagram [1] showing astrophysical candidates for UHECR's. For a given maximum cosmic ray energy, a horizontal line can be drawn such that only objects which lie above the line can be considered viable accelerators. Figure from [2].

GZK mechanizm) [26, 27] with an interaction length of about 50 Mpc, producing ultra high energy (UHE) neutrinos in excess of 10^{18} eV in the process (the GZK flux) [28] which have interaction lengths greater than the diameter of the observable universe. Additionally, the surviving cosmic rays have their trajectories bent by both galactic and intergalactic magnetic fields, complicating the search for their sources, while the neutrinos are free to propagate from source to detector unimpeded. This positions neutrinos as a promising candidate for the study of UHECR sources.

The chain reaction by which the GZK flux is produced is given by

$$p + \gamma_{CMB} \rightarrow \Delta^{+} \rightarrow \pi^{+} + n \rightarrow p + \nu_{\mu} + \bar{\nu_{\mu}} + \nu_{e} \tag{1.1}$$

Over cosmological distances, the 1:2:0 ratio of $\nu_e : \nu_\mu : \nu_\tau$ produced near the source oscillates to a 1:1:1 ratio as measured at the detector [29].

The delta also has a decay branch through neutral pions $\Delta^{+} \rightarrow \pi^{0} + p \rightarrow p + 2\gamma$, and as such, gamma-ray and UHE neutrino production are closely linked.

1.2 Prospects for Multi-messenger Astronomy

The minuscule cross-section of UHE neutrinos ensures that they will propagate across intergalactic distances without their direction being altered. This opens the door for a neutrino telescope to identify the position of point sources on the sky directly from the arrival direction at the detector. In particular, very large in-situ detectors such as the proposed ARIANNA array (see Chapter 2) are uniquely powerful tools for detecting luminous transient events, by virtue of their tremendous effective volume. This capability is brought into particular fo-

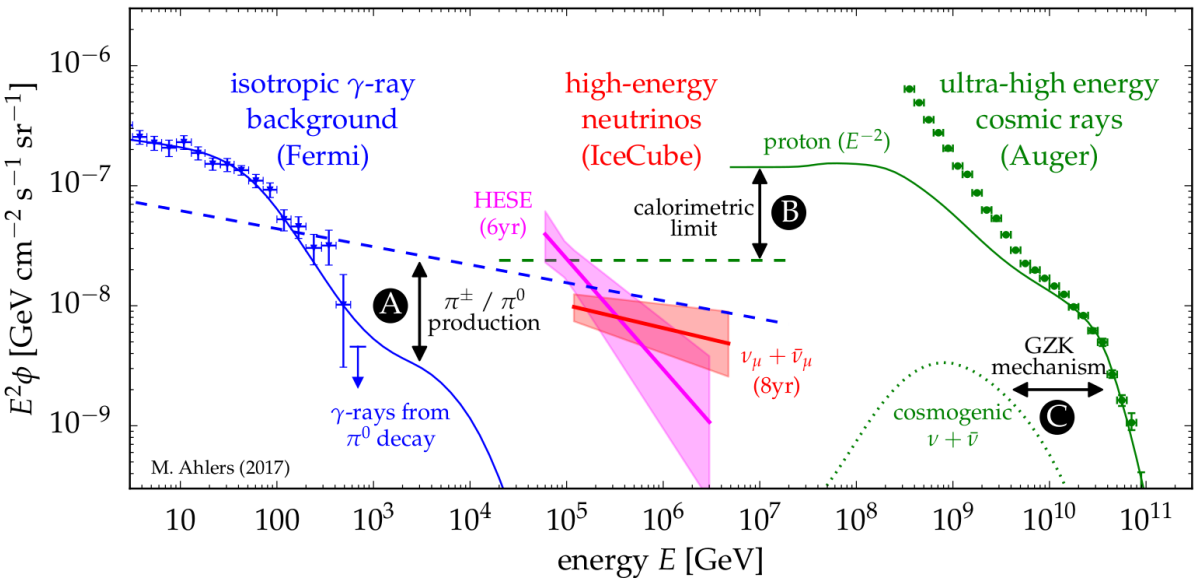

Figure 1.2: Spectral flux of gamma-rays, high-energy neutrinos, and UHE cosmic rays, from [3]. (A) The joint production of gamma-rays and neutrinos from cosmic ray induced pion decays implies a relationship between their fluxes (solid and dashed blue lines respectively). (B) Models of cosmic ray emission (solid green line) predict a certain maximum neutrino flux due to calorimetric conversion of CR's through pp and $p\gamma$ interactions (known as the Waxman-Bahcall limit [4]). (C) Interactions of the highest energy cosmic rays with CMB photons produces the, as-of-yet unmeasured, GZK neutrino flux. Diffuse gamma-ray and UHE neutrino flux measurements from [5] and [6], respectively.

cus by the insurgence of multi-messenger astronomy, and the goal of detecting astronomical events across neutrinos, gravitational waves, and photons of various energies.

The intriguing correlation of neutrinos measured in IceCube with the blazar, TXS 0506+056 [30, 31], prompted renewed interest in the role of neutrinos in multi-messenger astronomy. Theories of UHE cosmic ray production predict a deep relationship between gamma-rays, astrophysical neutrinos, and UHE charged cosmic rays. The measured astrophysical neutrino flux from IceCube [14, 15] is helping to form a unified picture of the non-thermal universe, with a key role to be played by the future measurement of the GZK neutrino flux (see Figure 1.2).

The measurement of gravitational waves from a neutron star/neutron star merger by the Advanced LIGO and Advanced Virgo detectors, coincident with a gamma-ray burst detected

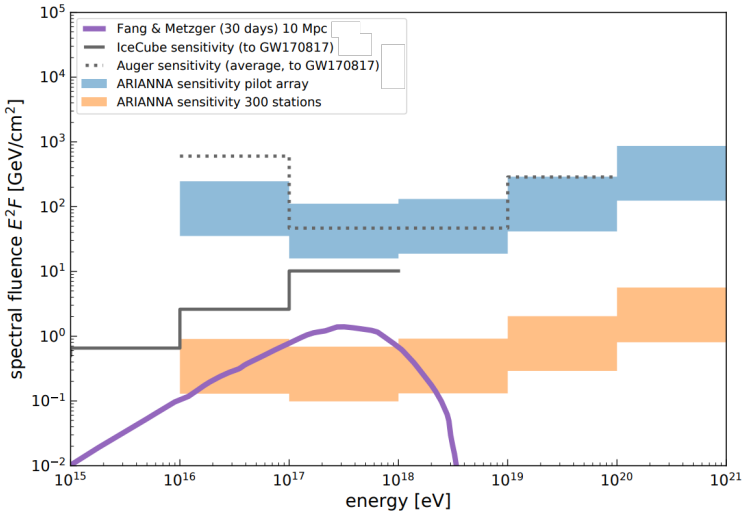

Figure 1.3: Expected spectral fluence of neutrinos from gravitational wave event GW170817 (purple line)[7], as well as sensitivities of the IceCube neutrino observatory and Pierre Auger observatory [8]. The effective volume from an array of 300 ARIANNA style radio surface stations is expected to be sufficiently high to have expected an observation for this event. From [9].

by the Fermi Gamma-ray Burst Monitor on August 17, 2017 was a watershed moment for multi-messenger astronomy [32]. Such events are also thought to be potential cosmic ray accelerators, and therefore, sources of UHE neutrinos [7].

While current experiments such as IceCube and the Pierre Auger observatory lacked the sensitivity to measure the expected neutrino flux from this event [8], the significantly larger volumes required to construct an in situ UHE neutrino detector would lead to significantly greater sensitivity. Figure 1.3 shows results from a preliminary study, suggesting that an array of 300 ARIANNA surface stations would have the required sensitivity to expect a flux measurement from the GW170817 event [9]. It may take such a detector to realize the ambitious goal of measuring a single astronomical object using three fundamental messengers.

1.3 Radio Emission from Neutrino Induced Showers

The likely path forward to a cost-effective gigaton neutrino detector relies on radio detection methods. The orders of magnitude longer effective lengths at radio frequencies, as opposed to optical, allows for many cubic kilometers of ice to be instrumented with sparse detectors. The fact that radio frequency emission is expected for UHE neutrino interactions in ice is quite an interesting phenomenon, and worthy of explanation.

The primary neutrino interacts via deep inelastic scattering mediated through W^{+-} (charged current (CC)) or Z bosons (neutral current (NC)). The energy transferred to the nucleon generates a hadronic cascade which develops over a few meters. For a shower where these particles are contained within some radius r_m (the Molière radius), radio emission where the wavelength $\lambda > r_m$ sums coherently such that the electric field amplitude will scale linearly with the shower energy. Since the particles in the cascade have ultra-relativistic momenta, they will be traveling faster than the speed of light in the media, compressing the coherent power along the Cherenkov cone angle. This process relies on the macroscopic separation of charges, which is achieved by two separate mechanisms.

Geomagnetic emission, which is of primary concern for air showers, arises from the time dependent currents which are induced via the Lorentz force of the Earth's magnetic field acting on the individual charged particles in the shower. Both the strength and polarization of the resulting radio emission is determined by the relative orientation of the shower axis to the magnetic field, with the polarization given by $\vec{v} \times \vec{B}$, where $\vec{v}$ gives the propagation direction of the shower. Since the direction of the magnetic field is known, the measurement of the polarization direction can be used as a powerful background filter.

In dense dielectric media, such as ice, salt, or sand, matter effects lead to a time dependent longitudinal separation of electric charge along the shower axis, which is the dominant method of emission in these media. This process, known as the Askaryan effect [33], depends

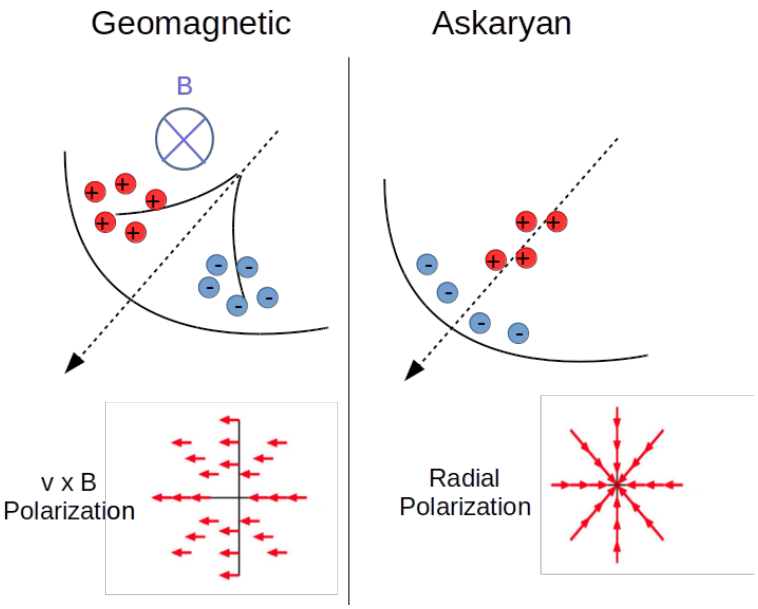

Figure 1.4: Diagram of the two main methods for coherent radio emission in particle showers. The geomagnetic mechanism (left) relies on the time dependent transverse currents induced by the Earth's magnetic field. Geomagnetic emission has a characteristic polarization in the $\vec{v} \times \vec{B}$ direction. Askaryan emission arises due to charge separation along the shower axis, leading to a radial polarization profile.

on a combination of the positron annihilation cross-section and scattering of electrons form the media into the developing shower. The nature of the charge excess leads to a radial polarization pattern (see Figure 1.4).

Both of these emission mechanisms have been experimentally verified in multiple regimes. The radio footprint of UHE cosmic ray air showers have been measured by the LOFAR collaboration [10], and is found to be in extremely good agreement with Monte Carlo simulations from CoREAS [34]. While the geomagnetic emission is typically dominant in air showers, the Askaryan effect is also a contributing factor, particularly for geometries where the shower is aligned with the Earth's magnetic field. This leads to an interesting interference between the two polarization patterns, resulting in a characteristic "bean-shaped" footprint (see Figure 1.5)

Askaryan emission has been experimentally verified through laboratory measurements in a number of media [35, 36, 37, 38]. The effect was measured in ice by the ANITA collaboration

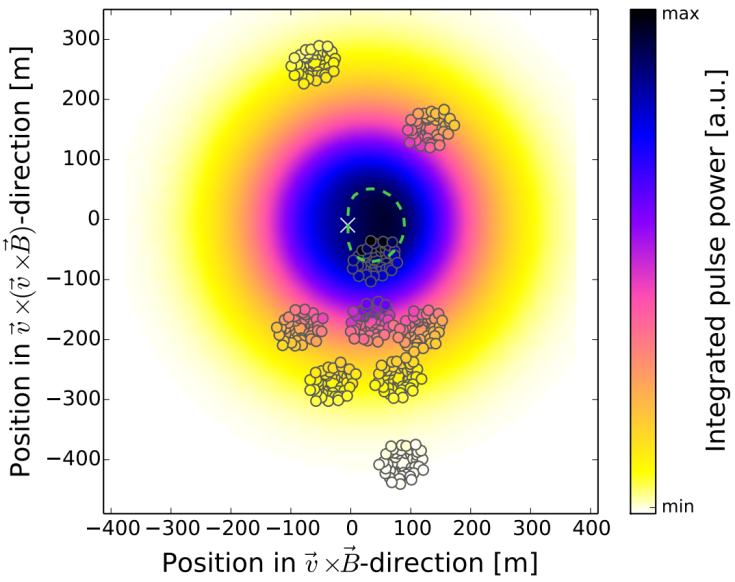

Figure 1.5: Comparison of integrated pulse power measured by the LOFAR array (colored circles), as compared to a fit derived from CoREAS simulations (background color). Positions are transformed in to the shower plane, with the shower axis at the origin. The dashed green line shows a line of constant amplitude, highlighting the "bean-shaped" profile which arises from the interplay of geomagnetic and Askaryan effects. From [10].

in the SLAC T486 experiment [11], by striking an ≈ 7 ton target with 10 ps bunches of 28.5 GeV electrons, which typically contained a billion particles. The coherent radio emission of the developed showers, which had a total composite energy of 3×10^{19} eV, was measured in detail, including both the frequency and angular profiles of the emission. This sets a solid foundation for the use of radio detection methods in search of UHE neutrinos.

1.4 Design Requirements of an UHE Neutrino Telescope

A main goal of an UHE neutrino telescope would be to measure or rule out models for the diffuse flux predicted by various cosmogenic models. Such models cover a wide parameter space, which is as-of-yet relatively unconstrained, and depends on such factors as UHE cosmic

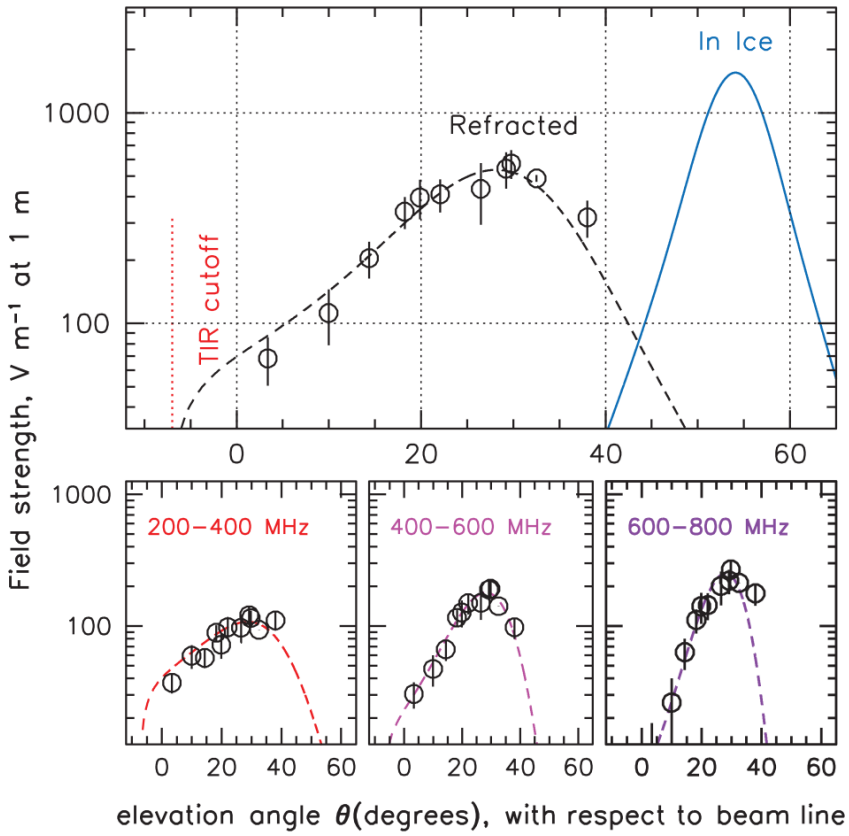

Figure 1.6: Electric field strength measured as a function of angle from the shower axis over frequencies from $200 - 800\,\mathrm{MHz}$ (top) and various sub-bands (bottom) from SLAC T486. Dashed lines represent the prediction, accounting for refraction out of the target ice, while the solid blue line represents the in-ice profile. From [11].

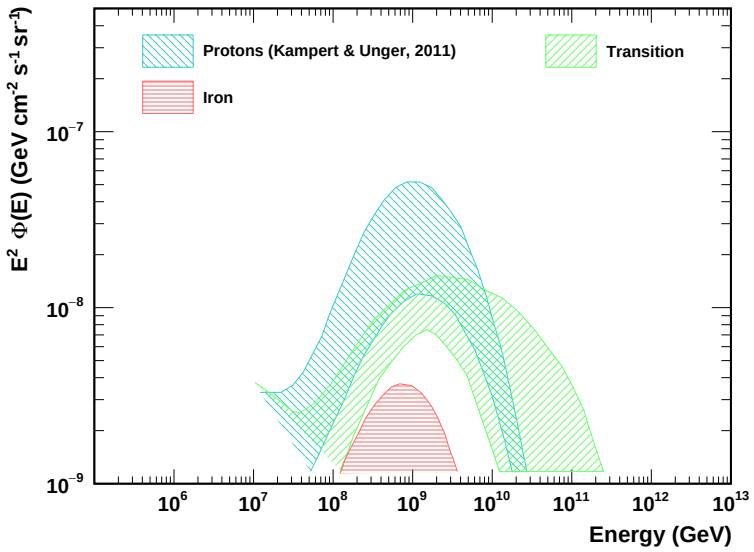

Figure 1.7: Selected models of the GZK UHE neutrino flux for various compositions, source evolutions, etc. [12].

ray composition, source evolution, and the high energy cosmic ray cutoff. A typical trend in these models is a higher proton fraction corresponds to a greater peak flux, since the energy per nucleon is higher in this case. The most pessimistic models, which correspond to an iron only composition, have peak values of $E^2\Phi \approx 10^{-9}\,\mathrm{Gev}\cdot\mathrm{cm}^{-2}\cdot\mathrm{s}^{-1}\cdot\mathrm{sr}^{-1}$ at $E = 10^9\,\mathrm{GeV}$ (see Figure 1.7) [1].

Probing these minuscule fluxes is an ambitious challenge, requiring a detector with an effective volume of $> 1000\,\mathrm{km}^3\mathrm{sr}$ a 5 year run to achieve the required sensitivity. The details of such calculations are presented in Section 5.4.1.

Making the jump from detection to astronomy requires extraction of more information from neutrino events than simple counting. For radio techniques, measurement of the signal arrival direction is straightforwardly accomplished by using the relative timing between antennas at different locations. The arrival direction of the neutrino, however, requires additional information. Since the radio emission from a neutrino induced shower in ice is concentrated within a few degrees about th Cherenkov cone, a measurement of signal arrival direction

[1] In perhaps more intuitive units, this corresponds to a flux of $\approx 2.28/km^2/year$ in a half-decade bin centered at 10^9 GeV, most of which will pass through the detector.

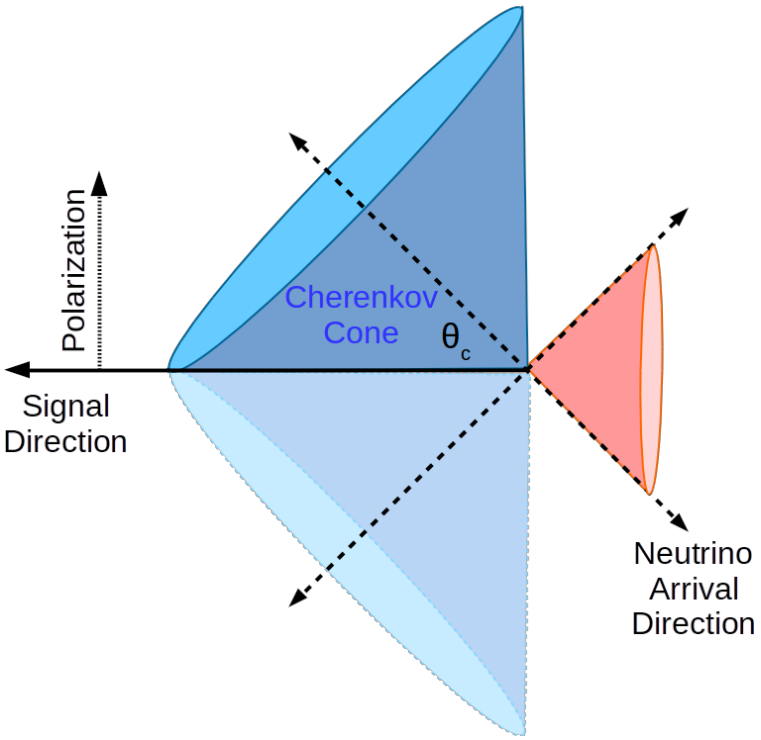

Figure 1.8: Diagram for neutrino direction reconstruction. Without a polarization measurement, the signal can be assumed to be near the Cherenkov cone (blue cone) and the neutrino arrival direction can be confined to a cone (red cone). Given the radial polarization of Askaryan emission (Section 1.3), the combination of signal direction and polarization gives a unique neutrino arrival direction.

constrains the neutrino arrival direction to a cone. To break this symmetry and discern a unique arrival direction for the neutrino, a polarization measurement is also required (see Figure 1.8). This requires some combination of antennas which are sensitive to different polarizations.

Energy reconstruction brings additional challenges. Fundamentally, the fraction of neutrino energy which is deposited into the initial hadronic shower depends on the statistical distribution of the inelasticity (see Chapter 3). Depending on the interaction channel (CC vs NC) and the neutrino flavor, the energy of the secondary lepton may be practically impossible to measure using radio techniques. See Section 3.6 for a discussion of the various flavor effects.

It is possible to use the results of Monte Carlo simulations to place statistical bounds on

the shower energy based on signal arrival direction, as was done in [24], but event-by-event energy reconstruction requires vertex reconstruction in order to establish the path length between the vertex and the detector.

For nearby events is is possible to reconstruct the event vertex by measuring the sphericity of the wavefront at the detector. For this method, the maximum distance for vertex reconstruction is related to the baseline distance between antennas as well as timing precision. Larger antenna spacing leads to a larger reconstructible distance but, beyond a certain point, the geometrical constrictions of Askaryan emission limit the measurable signal in some of the channels, and the reconstruction breaks down.

Since the frequency content of the Askaryan emission is highly dependent on the viewing angle relative to the Cherenkov cone (see Figure 1.6 and Section 3.4), it is possible to leverage the measured frequency spectra to reconstruct the vertex location. By measuring the spectra at multiple viewing angles, a measure of the cone width can be made, and used to estimate the distance to the vertex.

A preliminary "strawman"[2] design which was presented in [13] is shown in Figure 1.9. In this design, pairs of horizontally polarized LPDA's, along with vertically polarized dipole antennas near the surface, provide a measurement of signal arrival direction, as well as the 3D polarization measurement which is required to to perform neutrino direction reconstruction. A string of deeper dipole antennas sample the frequency spectra at different viewing angles relative to the Cherenkov cone, allowing for vertex reconstruction. This can serve as a starting point towards the design of a fully capable neutrino telescope.

[2]The term "strawman" is meant to denote the preliminary nature of the design, designed to provoke critical analysis and feedback. It will surely be picked apart and optimized as further detailed simulations are carried out.

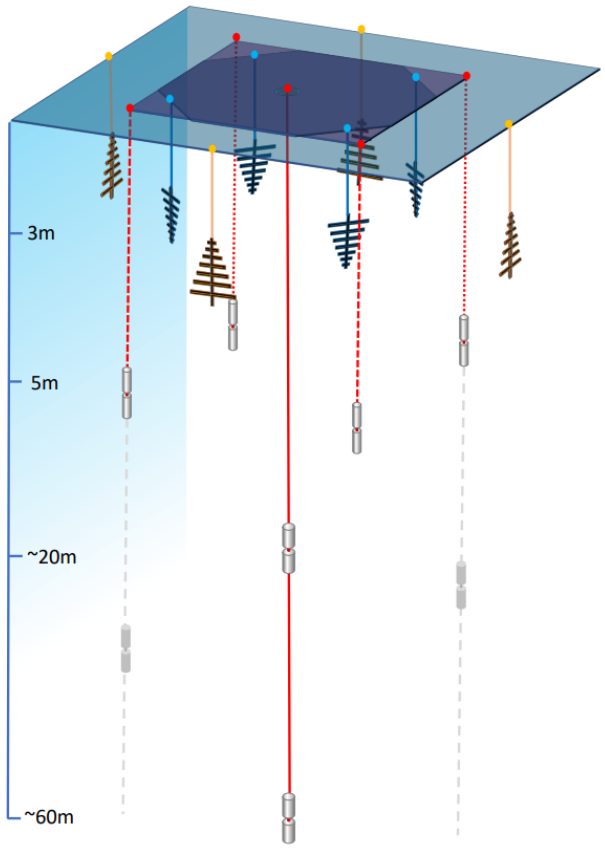

Figure 1.9: A proposed "strawman" design for a fully capable neutrino detector station, as was presented in [13]. The combination of LPDA's and dipole antennas near the surface allows for directional reconstruction based on signal arrival direction and 3D polarization measurement. The string of deeper dipole antennas can sample the frequency spectrum at multiple depths, so that the distance to the neutrino vertex (thus, shower energy) can be reconstructed. Upward facing LPDA's provide a reliable tag for cosmic ray air showers.

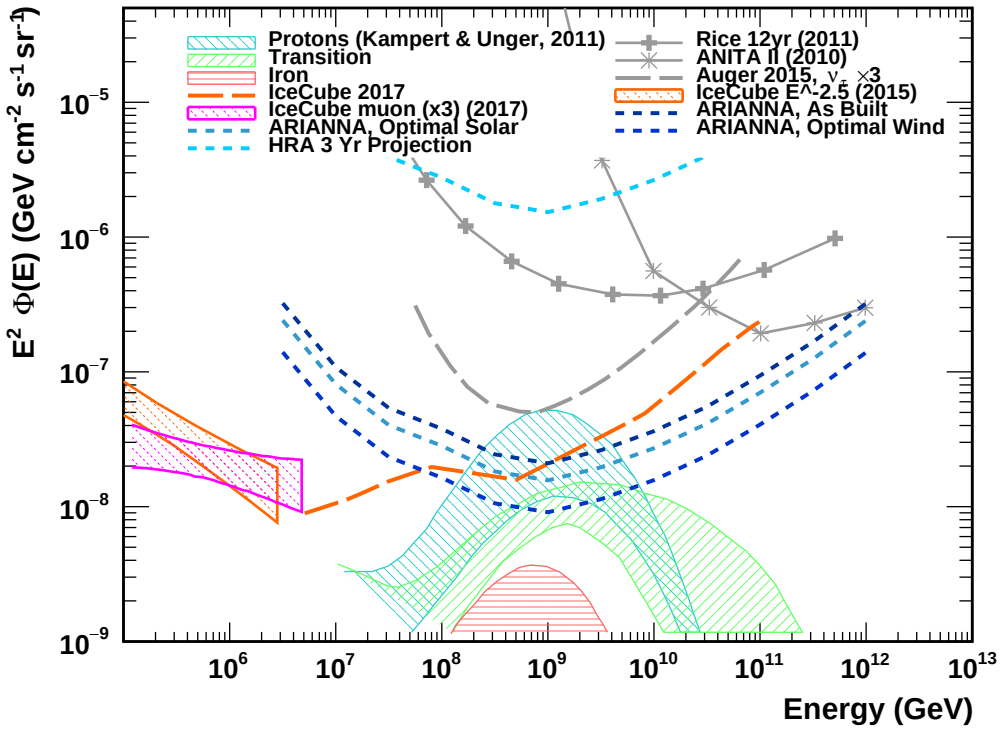

Figure 1.10: Current status of measured fluxes and 90% confidence upper limits on the flux of astrophysical and cosmogenic neutrinos. Experiments are continuing to probe models for the GZK flux, but predictions at 10^{18} eV span over an order of magnitude. IceCube spectra from [14, 15]. Icecube limit from [16]. RICE, Auger, and ANITA limits from [17, 18, 19]. GZK flux models from [12]. For details of the calculation see section 5.4.1.

1.5 Current Limits on the Cosmogenic Neutrino Flux

Great progress has been made experimentally in probing the flux of UHE neutrinos. Measurement of astrophysical neutrinos have been made up to energies of $> 1\,\mathrm{PeV}$, and sensitivities are probing deeper into the parameter space of the GZK flux predictions near $10^{18}\,\mathrm{eV}$. While this represents a tremendous achievement, there is clearly a great challenge in probing down to the most pessimistic iron-only GZK models, which have peak values of $10^{-9}\,\mathrm{GeVcm^{-2}s^{-1}sr^{-1}}$ or less (see Figure 1.10).

The experiments shown in 1.10 represent a variety of detection methods, with their own unique advantages.

The IceCube Neutrino Observatory represents the state of the art for the optical detection of astrophysical neutrinos. This detector consists of a cubic kilometer of ice, 1450 m below the surface of the South Pole, instrumented with 5160 digital optical modules (DOM's) which consist of highly sensitive photomultiplier tubes (PMT's) [3]. The detector density and timing information is such that the development of particle showers within the detector can be tracked in detail, and tracks of individual charged particles can be reconstructed from the timing of the emitted Cherenkov light.

Two separate analysis of the IceCube data have measured fluxes of astrophysical neutrinos up to $> 1\,\mathrm{PeV}$. The ν_μ only flux [15] relies on the single particle tracks generated by the Cherenkov radiation of muons in ice. This allows for sensitivity to neutrinos which do not interact within the physical volume of the detector, but sensitivity is mostly limited to upward going neutrinos which pass through the Earth, since atmospheric muons represent a significant background. The all flavor flux [14] includes "cascade" events in which the primary neutrino interaction takes place within the detector volume, which reduces background for downward going neutrinos.

IceCube's upper confidence limit [16] is the current best constraint on the all flavor flux of neutrinos from GZK neutrinos at $10^{18}\,\mathrm{eV}$.

The Pierre Auger Observatory is an array of instrumented water tanks and fluorescence detectors to search for cosmic ray air showers [39]. The neutrino limit [18] is based on a ν_μ only analysis. This analysis makes use of the τ double bang phenomenon (see Section 3.6) to search for the τ decay induced air showers which result from the interaction of ν_τ within the Earth.

ANITA (ANtarctic Impulsive Transient Array) is a long duration balloon experiment which uses a multitude of radio antennas to overlooks the Antarctic continent from an altitude of 37 km [19]. By virtue of the tremendous volume of ice which is observed, ANITA currently

sets the most restrictive limit on the neutrino flux above 10^{20} eV.

The RICE (Radio Ice Cherenkov Experiment) experiment serves as a prototype for a radio based in situ neutrino array [17]. This experiment consists of an array of 16 dipole antennas within a 200 m cube of ice centered 140 m below the surface of the South Pole. It relies on the same Askaryan emission as ARIANNA to detect UHE neutrino induced showers in the ice.

Chapter 2

The ARIANNA Experiment: Design, Testing, and Performance

2.1 The ARIANNA Station

The Antarctic Ross Iceshelf ANtenna Neutrino Array (ARRIANNA) concept depends on a grid of individual and autonomously functioning radio detector stations. In addition to the data acquisition (DAq) electronics and antennas, each station has its own self-contained power and communication systems. This allows the array to be scaled iteratively, without the need to build up complicated infrastructure for power and data delivery. Since each station operates as an autonomous neutrino detector, capable of transmitting data back to servers at UCI in near real-time, useful detector livetime can be accumulated during a multi-season construction of the full ARIANNA array.

Most of the station electronics are housed in a 9 x 12 x 9 inch brazed aluminum housing, which provides approximately 60 dB or RF attenuation. This main DAq box contains the system motherboard, as well as wifi, and Iridium satellite radios, and a 20 Ah lithium iron

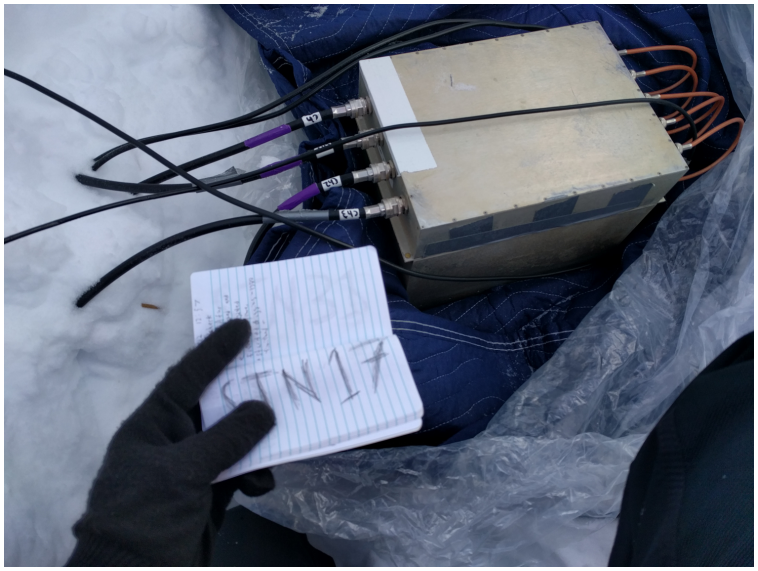

Figure 2.1: Photo of ARIANNA DAq box as deployed in Moore's Bay, showing the protective plastic bag and thermal blanket.

phosphate ($LiFePO_4$) battery with a custom configured battery management unit (BMU). Four low-power amplifiers are contained within a separate metal housing which is bolted to the main DAq box. This whole arrangement is installed near the center of the station, just below the snow, wrapped in an insulating blanket and plastic bag.

Each station consists of four log-periodic dipole antennas (LPDA's) which are directional by design, and have an effective bandwidth of $80 - 1000\,\mathrm{MHz}$ when buried in the snow. Since ARIANNA antennas are deployed just beneath the snow surface, there is some flexibility regarding the layout of the antennas. Some purpose-built cosmic ray stations contain upward facing LPDA's (Section 2.4). However, for the standard neutrino detecting station, the LPDA's are buried facing downward, arranged in two co-polarized pairs with a 6 m separation (see Figure 2.2). This arrangement makes the antennas sensitive to the upward traveling radio signals generated by neutrino interactions in the ice.

Additionally, there is a fifth LPDA antenna 50 feet northwest of station center, which is oriented in the horizontal plane facing the station. This antenna can be used to send a calibrated heartbeat pulse for monitoring of the station.

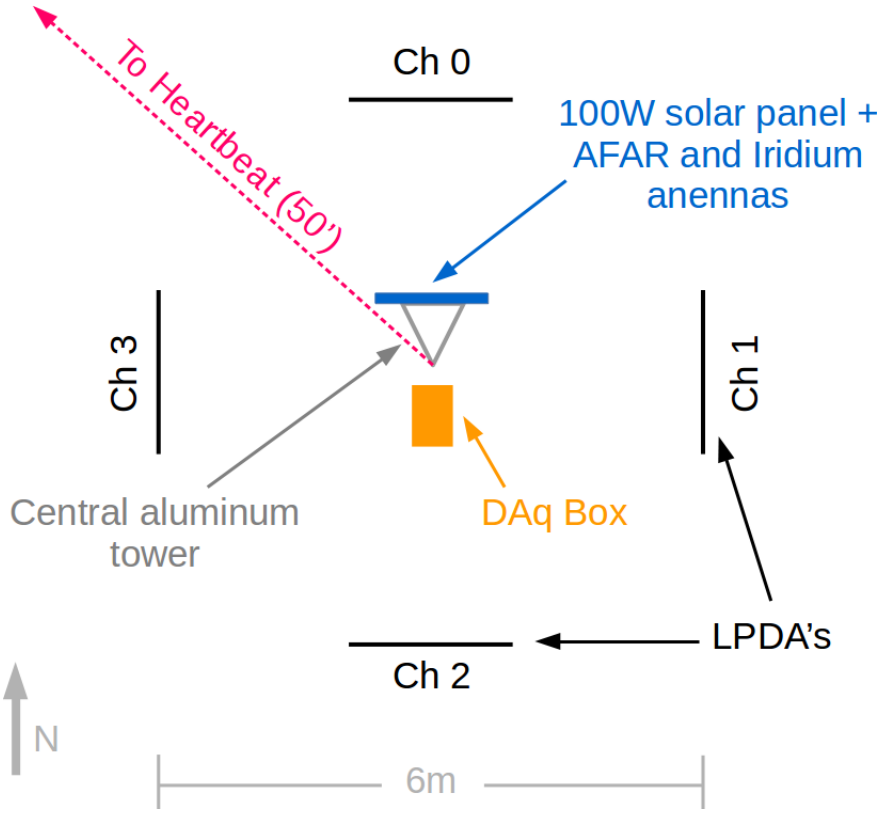

Figure 2.2: Top-down view of the ARIANNA HRA station layout. The southern vertex of the triangular tower acts as a reference for station center.

A 100 W solar panel, as well as antennas for AFAR and Iridium communications are mounted on a central aluminum tower. A group of 4 physicists with hand tools can install a new station in about four hours (Section 2.3.4).

2.1.1 Overall Design and Operation

The ARIANNA station can be broken down into several key subsystems; signal capture and amplification, data acquisition, power, and communications. How these subsystems are implemented follows the design principles of an autonomous and independent detector which must operate for extended periods without human intervention. Since the stations rely on solar power, they are designed to minimize power consumption and insure self-recovery after extended periods without power. Various software safety-nets are also implemented to ensure that stations can not be placed in a useless state.

High level control of the station is managed by an MBED micro-controller. The MBED controls the DAq and storage systems, as well as controlling communications and monitoring voltage and power consumption. A wide range of operational parameters can be configured remotely, allowing operators to react to information received by real-time monitoring. ARIANNA relies on a pull-only paradigm, whereby the remote station initiates communication with a central server to receive configurations and commands.

2.1.2 Data Acquisition System

For the 2014-2015 season, ARIANNA underwent a major revision of the data acquisition board. The new board, which is based around the Synchronous Sampling plus Triggering (SST) chip developed by Prof. Klienfelder's electrical engineering lab at UCI, offers more robust power protections, lower power consumption, and a simplified calibration procedure

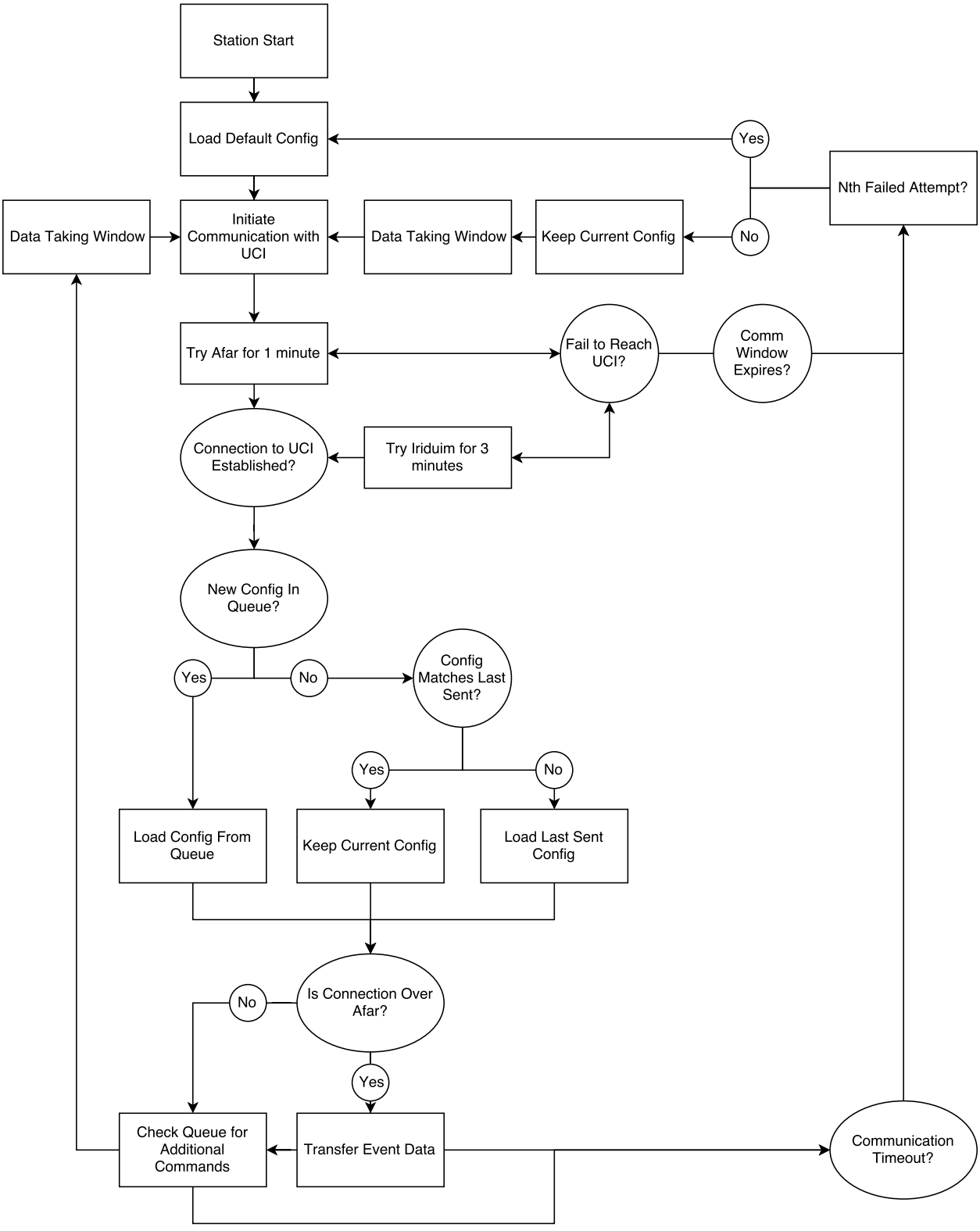

Figure 2.3: Control flow for ARIANNA station communication window.

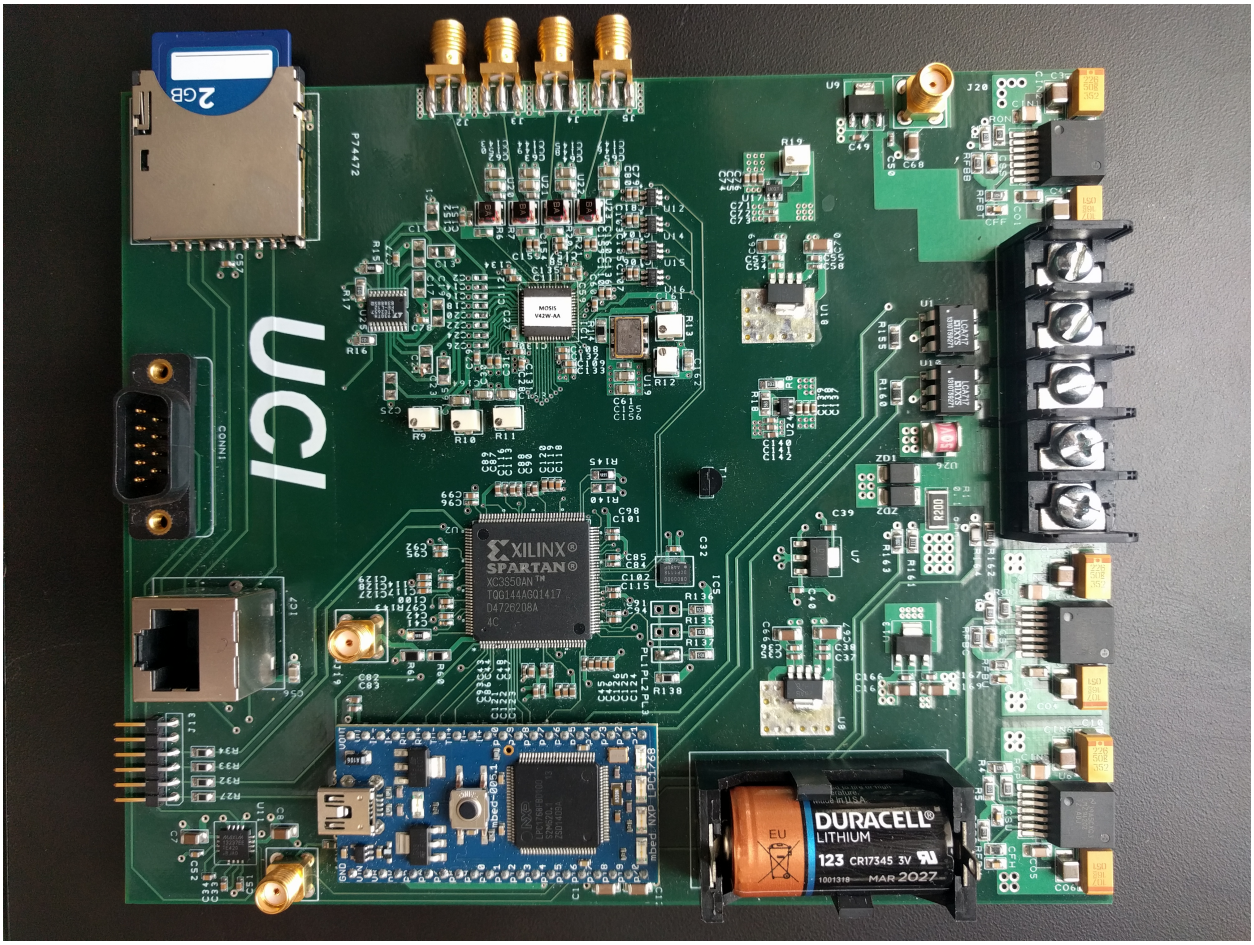

Figure 2.4: The SST Board.

[40, 41, 42]. The SST chip takes the place of four individual daughter cards (one for each input channel), and allows data acquisition to be incorporated on a single main-board, along with power regulation, data storage, etc. This has reduced the DAq power consumption (not including amps or communication peripherals) from $\approx 5.8\,\mathrm{W}$ to $\approx 1.7\,\mathrm{W}$.

The record for each DAq channel consists of 256 samples, with a sampling rate of $2\,\mathrm{GSa/s}$. Voltages are held on a circular buffer until a trigger signal is received, and then the record for each channel is read out and digitized by a $2.5\,\mathrm{V}$, 12 bit ADC. The signal input is AC coupled through a bias tee so that the ADC will not see a negative voltage from the bi-polar signal. The SST on the ARIANNA main board is controlled by a Xilinx Spartan 4 FPGA, which determines the trigger logic and manages the event readout.

Triggering of the SST is performed in analog using dedicated circuitry. Individual high and low trigger thresholds are set to comparators for each input channel. A channel's high and low thresholds must both be satisfied within a 5 ns window in order to form a trigger. This "high and low" coincidence imposes a strong constraint which significantly reduces the trigger rate from thermal noise. This constraint is analogous to a high pass filter, requiring signal power at frequencies greater than 100 MHz in order to trigger. This trigger logic was designed by my colleague Tarun Prakash, and is described in detail in his thesis [41].

We also impose an additional majority logic requirement between input channels, wherein two or more of the 4 channels must trigger within a 30 ns window. This takes advantage of the expectation that parallel LPDAs should see highly correlated signals from a plane wave source to further reduce thermal trigger rates. The value for the 30 ns majority logic coincidence window ($\Delta t_{coincidence}$) is informed by the maximum light propagation time across the antennas of an ARIANNA detector (Δt_{prop}) which, for an antenna separation of 6 m and a surface index of refraction $n = 1.3$, is roughly 26 ns. The constraint that $\Delta t_{coincidence} > \Delta t_{prop}$ avoids the unintentional veto of potential signal events.

High level control of the system board is managed by the an MBED LPC1768 micro-controller. The MBED sets trigger thresholds, switches power to the various peripherals, and monitors voltage, current, and temperature. Additional level one (L1) trigger tests can be performed real-time on the MBED. Currently, the L1 trigger vetoes events which are strongly peaked in the frequency domain, which is typical of constant wavelength (CW) anthropogenic noise. The L1 trigger will be discussed in more detail in Section 5.2.2.

After a trigger is formed and an event is read out, it is saved to an on-board SD card and transferred to UCI during the station's next communication window. Stations are typically configured to send up to 300 events per communication. In the case of very high event rates, or some other circumstance which prevents complete data transfer (such as a dropout in the WiFi link), stations can be instructed to transmit specific data files after-the-fact.

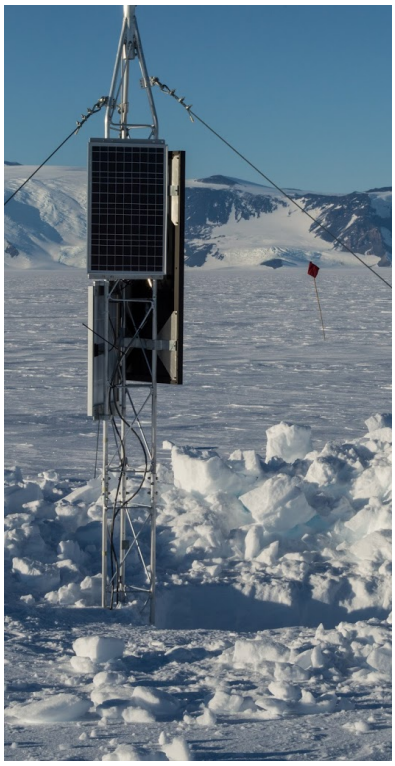

Figure 2.5: An ARIANNA power/communications tower. The configurations shown consists of a 100 W panel on the northward side, and 30 W panels on the other two sides.

2.1.3 Power Systems

Since the ARIANNA stations are not connected to a power grid [1], they rely completely on local and renewable power generation. The stations of the ARIANNA HRA are primarily powered by solar panels, which are elevated above the snow on triangular aluminum towers (see Fig. 2.5). A few solar panel configurations have been deployed on various stations, including some with panels on all three sides of the tower, as well as with a single 100 W panel on the northward side. Results have shown that the additional solar panels have a marginal effect on the overall station livetime on stations with a functioning battery system.

In order to maintain stable operation during the shoulder seasons when the sun begins to dip below the horizon, as well as during weather events, the ARIANNA stations also employ

[1] While stations deployed in Moore's Bay do not have the luxury, an ARIANNA station can operate off of grid power if it is available, as is the case with the South Pole pilot station (Section 2.4.5).

Paremeter	Value
High Voltage Cutoff Value	3600 mV per cell maximum
High Voltage Recovery Value	3300 mV per cell maximum
Low Voltage Cutoff Value	2700 mV per cell minimum
Low Voltage Recovery Value	3100 mV per cell minimum
Recovery Delay	2 s
Charging Voltage	14.7 V
Maximum Current	2000 mA

Table 2.1: Configuration Parameters of the BMU, as deployed for the ARIANNA HRA stations. See Fig. 2.6 for an overview of the BMU charging algorythm.

a rechargeable battery system. Each DAq box contains a 20 Ah (264 Wh) battery pack constructed of 36 (4 cells in series) $LiFePO_4$ cells manufactured by A123 Systems. The nominal voltage of the battery pack is 13.2 V (3.3 V per cell)

Power management between the solar panels, battery, and system board is handled by a Texas Instruments bq40z60EVM charge controller, hereafter referred to as the Battery Management Unit (BMU). The BMU is responsible for maintaining power to the station while ensuring that the cells of the battery pack are kept within safe operating voltages. This charge controller is highly configurable, allowing for customizable high and low voltage cutoffs, as well as high and low recovery voltages.

The "recovery" voltages are necessary to prevent hysteresis loops in the BMU's operation. For instance, in the absence of solar power, the station will be powered by the battery until one of the battery cells falls below the Low Voltage Cutoff Value. At this point, the station will be disconnected from the battery. In the absence of a load, the battery voltage will asymptotically relax to some value higher than the Low Voltage Cutoff, with the relaxed voltage being a function of the current before disconnect and the temperature of the battery. If we require the voltage on all cells to raise above some Low Voltage Recovery Value before the battery can resume powering the station, we can avoid a control loop which can lead to repeated power cycling of the station. See Figure 2.6 for a graphical representation of the BMU control flow.

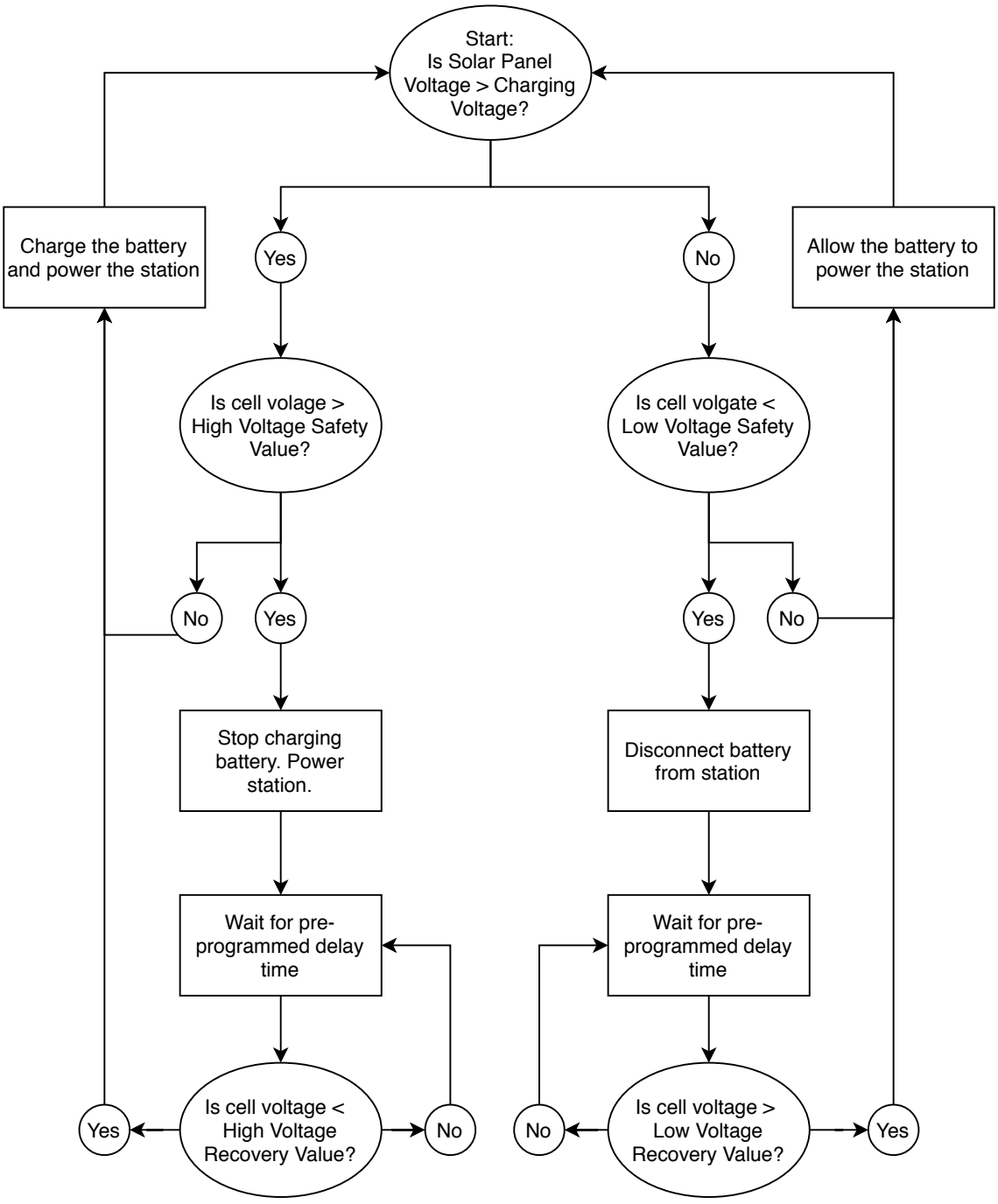

Figure 2.6: Control flow of BMU, which keeps the battery cells within safe operational voltages while the station is powered. See Table 2.1 for a list of parameters.

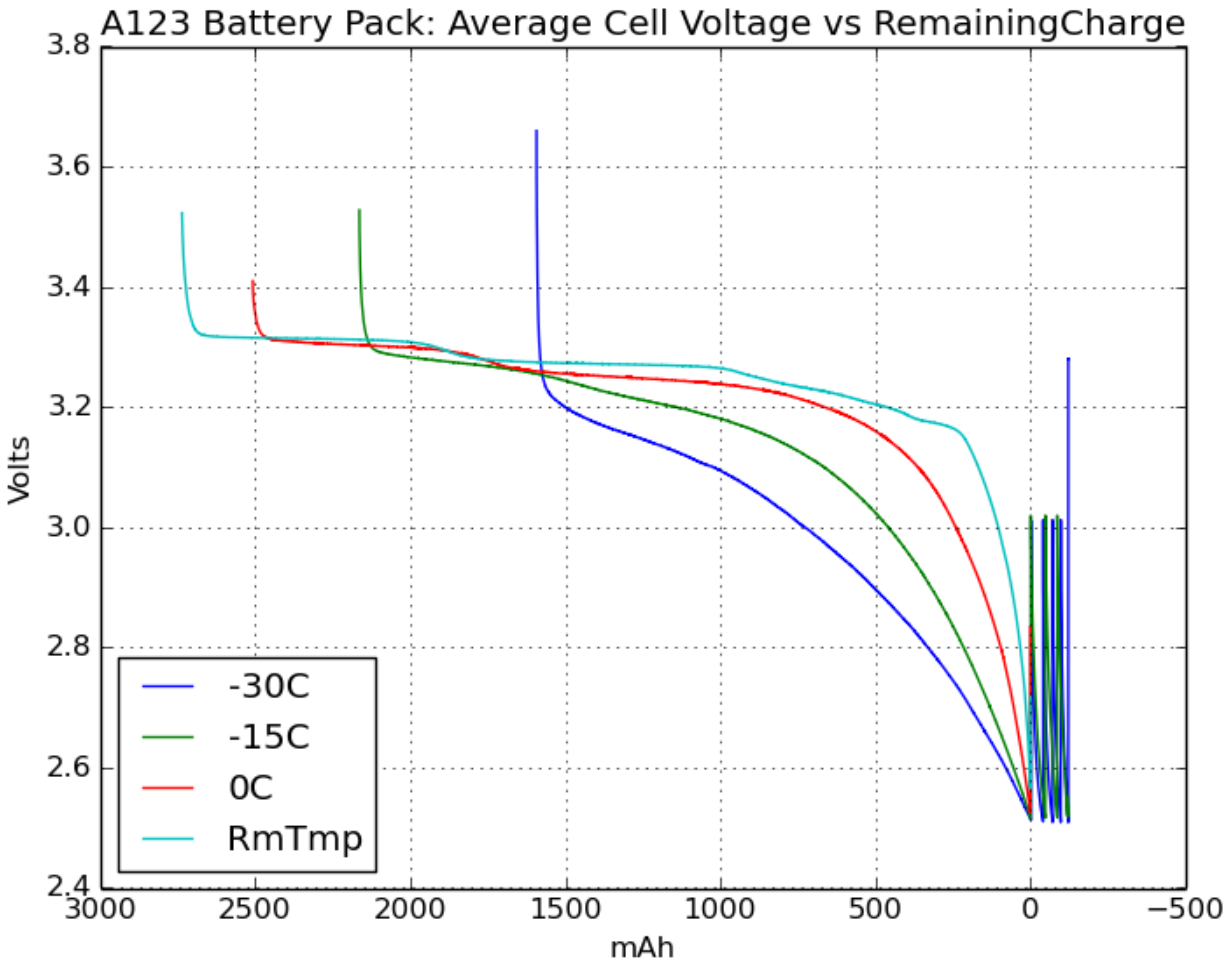

Figure 2.7: Average cell voltage vs remaining capacity at various temperatures for 4-cell battery pack of A123 systems $LiFePO_4$ cells with a rated capacity of 2500 mAh. Measurements were taken as the battery was discharged from full at a rate of ≈ 115 mA (0.046 C), so time flows left to right. Current discharged after the initial low voltage cutoff is not considered in the useful capacity.

The BMU also performs the important task of balancing the cell voltages. When more than one battery cell is connected in series, there is a tendency for the voltages on the individual cells to drift over time. Since the charging algorithm depends on the cells with the most extreme voltages (only one cell needs to fall below the Low Voltage Cutoff Value to shutdown the station, for instance) any discrepancy in the individual cell voltages amounts to a reduction in the useful capacity of the battery. The BMU actively provides additional current to lower voltage cells in order to maintain balance.

Since ARIANNA stations operate in sub-freezing temperatures (typically between $0°C$ and $-15°C$), the low temperature performance of the battery cells is of particular interest. Not only is capacity negatively impacted by decreasing temperatures, but hysteresis effects of charging/discharging also become exaggerated. This means that charging algorithm parameters must be carefully chosen to avoid control loops and maximize station livetime, while protecting battery health.

The discharge capacity of the A123 $LiFePO_4$ cells was measured at various temperatures using a 4-cell (in series) test pack. The pack was discharged to the Low Voltage Cutoff, held at temperature several hours to reach equilibrium, charged to the High Voltage Cutoff, and measured while discharging to the Low Voltage Cutoff at the desired temperature. Results (Fig. 2.7) show that the $LiFePO_4$ cells maintain more than 85% of their design capacity for temperatures above $-15°C$, and greater than 60% at $-30°C$.

2.1.4 Amplifiers

Each ARIANNA DAq input channel has a separate amplifier board, which provides approximately 60dB of amplification. These amps were custom designed for the ARIANNA project by Thorsten Stezelberger at Lawrence Berkley National Laboratory, with fabrication managed by UCI's engineering lab. Power efficiency was a main design criterion for these amplifiers, which consume $\approx 0.25\,\mathrm{W}$ each. Each amp is individually shielded to prevent cross-talk through radio frequency pickup, and the amps for each ARIANNA station are placed in an aluminum box, separate from the DAq. Power to the amps and signals from the amp box to the DAq box are carried by co-ax cables.

There are two revisions of this amplifier board currently deployed in the ARIANNA HRA, referred to as the "100 series" and "200 series". These amplifiers have an effective bandwidth of $\approx 100\,\mathrm{MHz}$ - $1\,\mathrm{GHz}$ (See Fig 2.10). A third revision, "300 series" was also developed and

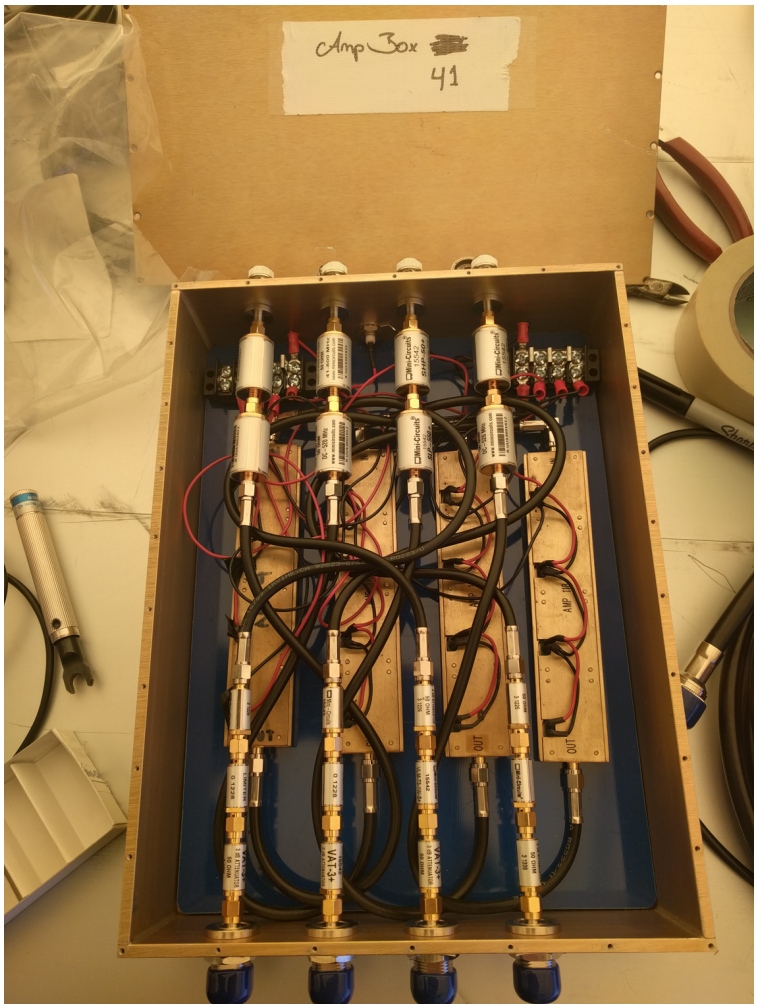

Figure 2.8: Photo of an assembled ARIANNA amp box, using 100 series amps.

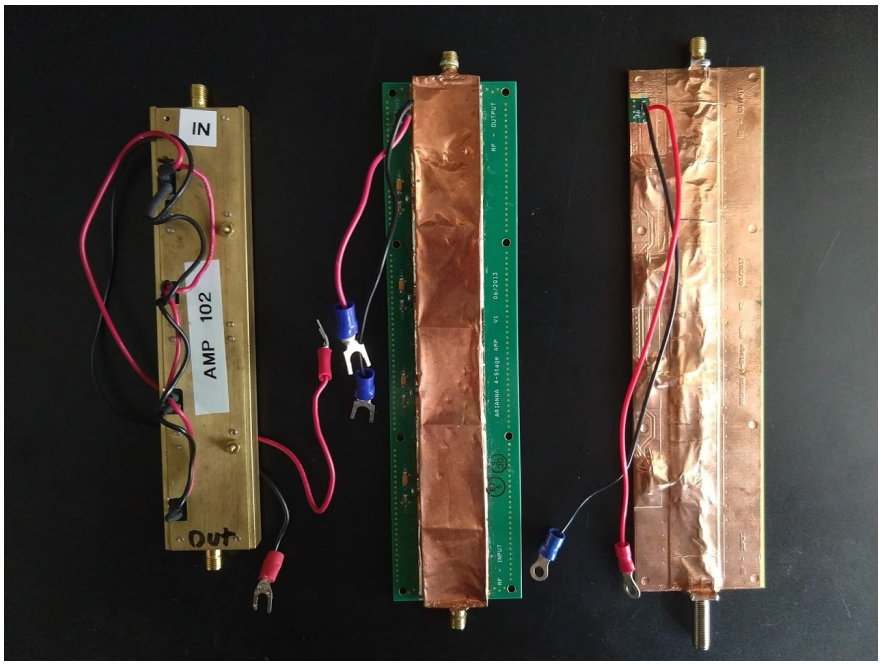

Figure 2.9: Visual comparison of 100, 200, and 300 series ARIANNA amplifiers (left to right).

is in deployment with the latest 8Ch ARIANNA SST boards in the specialized cosmic ray stations (see Section 2.4). These amps are based on the same amp board as the 200 series amps, but with a few modifications. Since the 8Ch DAq's are operated at a 1 GHz sampling rate, different filtering components are used to bring the bandwidth down to 500 MHz. The gain was also reduced, in order to increase the overall dynamic range of the system for improved reconstruction of high amplitude events.

All amplifiers are limited to ≈ 800 mV maximum output in order to protect the DAQ electronics. For the 100 series amps, this was accomplished using a combination of coaxial SMA attenuators and a 1V limiter (3 dB attenuator $\rightarrow$ 1 V limiter $\rightarrow$ 3 dB attenuator) on the amp output. The 100 series amps are also deployed with 100 MHz high pass and 1 GHz low pass filters on the input to reduce low frequency background and prevent aliasing. For the 200 and 300 series amps, all filtering and limiting is handled by on-board circuitry.

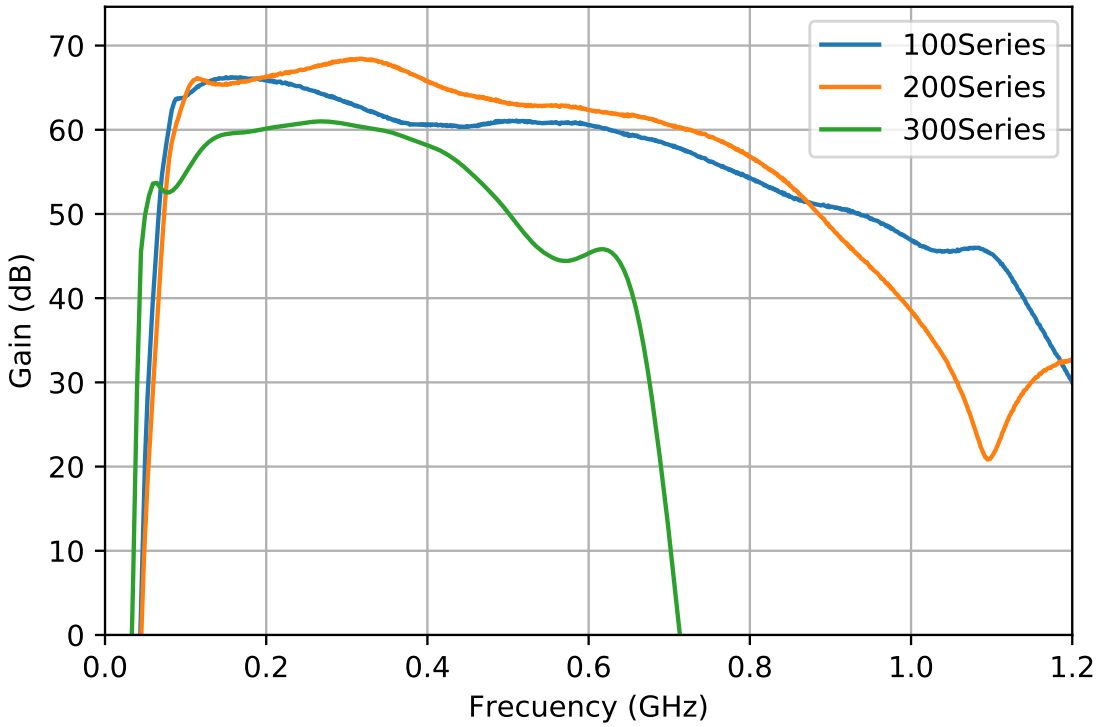

Figure 2.10: Gain vs frequency for various ARIANNA amplifier revisions. 100 series response includes 100 MHz high pass and 1 GHz low pass filters on the input, as well as (3 dB attenuator → 1 V limiter → 3 dB attenuator) on the output.

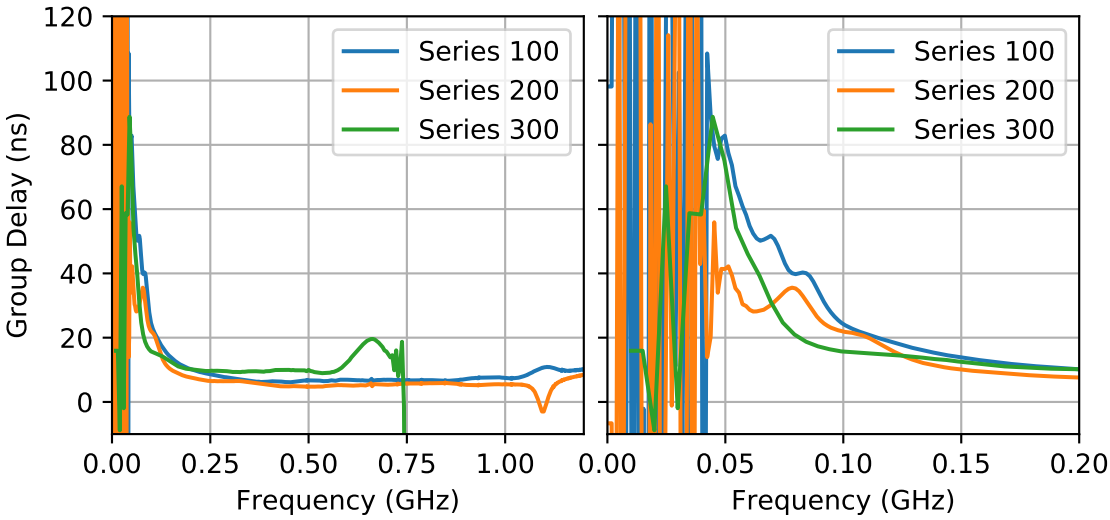

Figure 2.11: Group delay for various ARIANNA amplifier revisions.

Amplifier Type	Measured V_{RMS}	Calculated T_{eff}
Series 100	17.6 mV	336 K
Series 200	23.2 mV	326 K
Series 300	9.1 mV	531 K

Table 2.2: Measured room temperature V_{RMS}, along with the effective noise temperature calculated from 2.2, for the various amp types.

Thermal noise fluctuations of the amps provide the fundamental floor which determines the detector thresholds. These thermal fluctuations closely follow a Gaussian distribution in voltage

$$\rho(V) = \frac{1}{\sqrt{2\pi\sigma^2}} e^{-\frac{V}{2\sigma^2}} \tag{2.1}$$

where $\sigma = V_{RMS}^{amp}$, the root-mean-square voltage after amplification. Ideally, the thermal noise power P from a resistor (the LPDA antennas in this case) over a matched load is given by $P = k_B B T_{eff}$ where B is the bandwidth, T_{eff} is the effective noise temperature in Kelvin, and k_B is the Boltzmann constant. Using Ohm's Law, this can be rearranged to calculate the root-mean-square voltage of the pre-amplification noise signal $V_{RMS}^{noise} = \sqrt{PR} = \sqrt{k_B B T_{eff} R}$ where $R = 50\,\Omega$ is the load impedance. For an amplifier with frequency dependent gain, this can be generalized to calculate V_{RMS}^{amp}

$$V_{RMS}^{amp} = \sqrt{k_B T_{eff} R} \left(\int g^2(f) df \right)^{1/2} \tag{2.2}$$

where $g(f)$ is the linear gain of the amps.

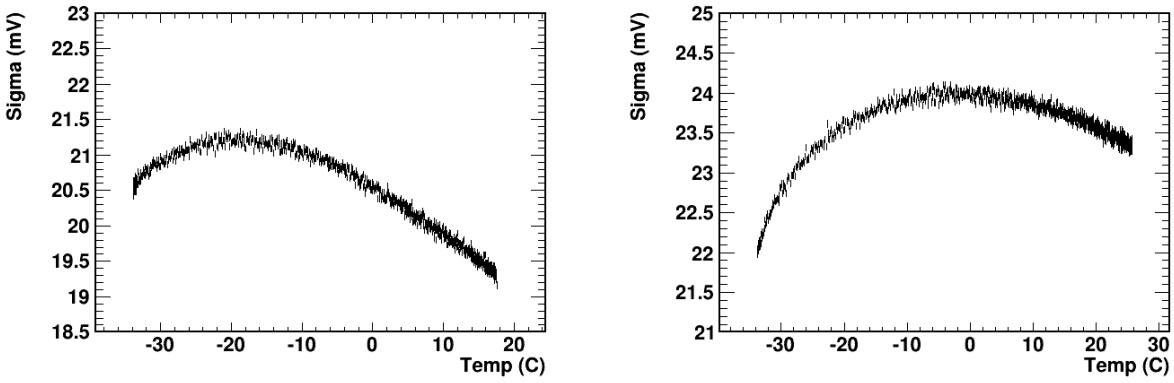

(a) 100 Series (b) 200 Series

Figure 2.12: Temperature dependence of thermal noise V_{RMS} for 100 and 200 series amplifiers as measured on the ARIANNA DAq. This test was performed in the lab, with the DAq taking forced triggers at 10 Hz as the system slowly returned from 30 °C to room temperature over about 20 hours. Values are not gain calibrated, so systematic error $\approx 10\%$.

Since the raw thermal noise power pre-amplification is a monotonically increasing function of temperature, one might be temped to assume that the thermal noise V_{RMS} of the amps would decrease with decreasing temperatures. This is, however, not the case; as shown in Figure 2.12. As temperatures are lowered, the lower thermal noise power is offset by an increase in the amplifier gain. The net effect is that the thermal noise V_{RMS} measured by the DAq peaks at some particular temperature, depending on the amp type.

2.1.5 Antennas

Each channel of the ARIANNA HRA stations are fed by Create Design Corp. CLP5130-2 LPDA antennas which have an effective bandwidth of $80 - 1000$ MHz when embedded in the firn of the Ross Ice Shelf. These antennas are buried facing downward in the snow, forming two co-polarized pairs of 6 m separation in a square pattern (see Figure 2.2).

These antennas have been well studied, both measured in anechoic chambers [23] and simulated in the WIPL-D antenna simulation software suite [43, 20]. WIPL-D is a robust antenna

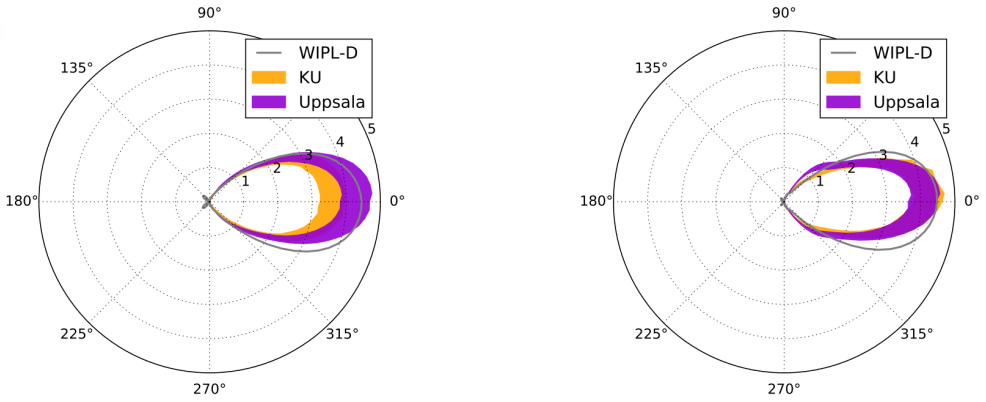

Figure 2.13: Comparison of antenna patten for WIPL-D simulation and anechoic chamber measurements (colored bands) for 330 MHz (left) and 400 MHz. Antennas are oriented in the plane, with 0° representing the boresight of the antenna. From [20].

simulator, able to model antennas in embedded in various media as well as near interfaces, making it an important tool for a detector like ARIANNA that has antennas near the surface. Simulations have been shown to be fairly consistent with lab measurements, with average gain agreeing to within 10% [20]. For the simulations in this work, we use a model for the LPDA based on WIPL-D simulation in infinite firn with index of refraction $n = 1.3$, unless otherwise noted.

2.1.6 Communication Systems

Each ARIANNA station contains two independent communication peripherals, in order to provide redundancy. This is vital to the autonomous operation of the stations, since after a re-boot the station must communicate to UCI to receive a data taking configuration (see Figure 2.3).

The primary communication mode is a high speed 2.4 GHz wireless ethernet connection through an Afar Communications PulsAR bridge, capable of transfer speeds of 200 kB/s. ARIANNA stations communicate with an Afar relay near the summit of nearby Mt Discovery, which in turn links to a root Afar in McMurdo Station which is connected to the Internet.

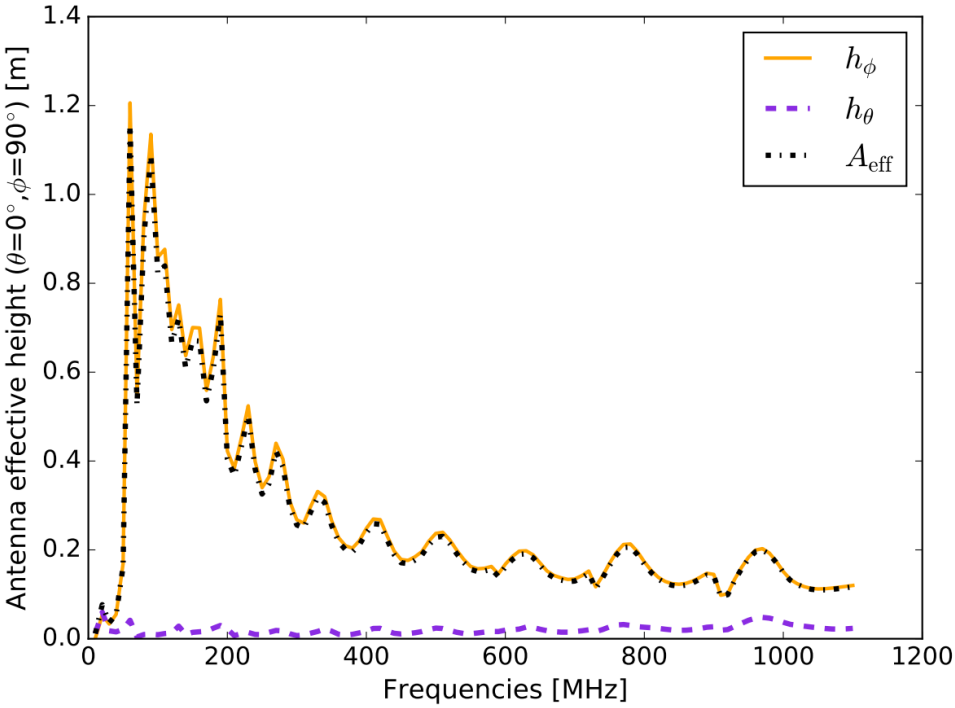

Figure 2.14: Effective height or the Create Design Corp. CLP5130-2 LPDA as simulated in WIPL-D, emersed in infinite firn ($n = 1.3$). From [20].

Stations can either connect directly to the Mt Discovery relay, or mesh through another station's Afar, if that connection is stronger. Communications via Afar are handled by a constantly running listener script on the SnowFlake server at UCI.

When ARIANNA stations connect through Afar, they transmit the last data file recorded during the previous data taking window, which can contain up to 300 events (though it is often less during stable, low rate operation). Data which is not collected in real-time can be transferred in bulk over Afar at a later date.

Communication via Iridium Satellite is used as a backup method of communication, and it has been found to be extremely reliable, and less prone to weather interruptions than Afar communication. Iridium communication is handled through the Short Burst Data (SBD) protocol, wherein the stations on-board SBD modem uploads individual 300 byte messages to the Iridium network, which are delivered to UCI via email. A constantly running listener

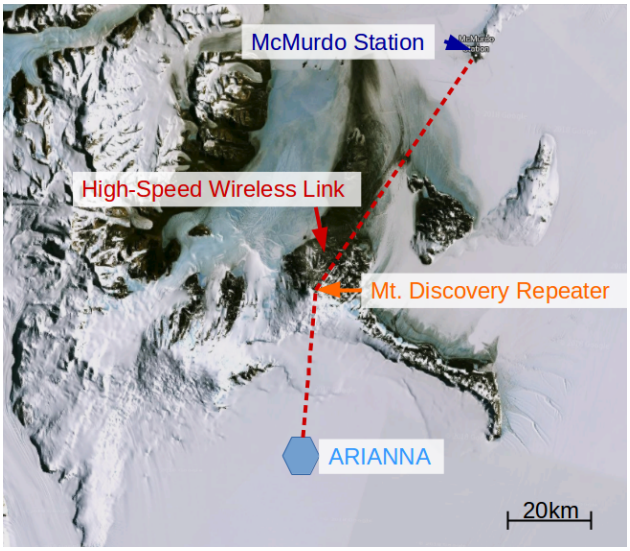

Figure 2.15: Image of ARIANNA's AFAR wifi link to McMurdo Station. Imagery courtesy of the U.S. Geological survey, via Google Maps [21].

script on the Snowflake server at UCI combines these messages into status updates, data files, etc., and sends commands to the station via the same protocol.

2.2 Calibration of Data Acquisition Systems

2.2.1 Fixed Patten Noise

Each sample of the SST's circular buffer can be thought of as an individual device, with an offset that must be calibrated. Uncorrected, these offsets produce a consistent null-signal, known as Fixed Pattern Noise (FPN), on the order of 7 mV RMS [40]. Each board has a unique FPN, but since this pattern is very stable, it can be measured in the lab before deployment and subtracted as part of data calibration.

In the lab, the FPN is measured by terminating all channel inputs at 50 Ω and taking 1000 forced triggers. The ADC values for each sample are averaged in order to calculate the FPN for each channel.

The FPN can also be calculated in-situ using min-bias events. Since thermal noise measured from the amps strongly obeys a symmetric Gaussian distribution, the average ADC values for each sample over many min-bias events should be equivalent to the null signal. By definition, this procedure also accounts for any DC offset.

In our data production, the FPN subtraction algorithm also performs an uncalibrated scaling of ADC counts to approximate voltage using the slope in Eqn. 2.3.

2.2.2 DAq Gain Calibration

As with any analog-to-digital converter (ADC), the device produces a unitless number which must be calibrated to represent a quantity with physical units. The waveform digitization of the ARIANNA DAq uses a 2.5 V, 12 bit ADC, with a +900 mV offset provided by a bias tee. This relationship is given by:

$$V_{uncalibrated} = \frac{ADC}{2^{N_{bits}} - 1} \times range - offset = \frac{ADC}{4095} \times 2500\,\text{mV} - 900\,\text{mV} \tag{2.3}$$

To improve accuracy and properly account for individual part variations, it is necessary to compare the measured signal on the DAq with a source of well known amplitude. In order to do this, pure sine-wave output from a signal generator was sampled by the DAq over several thousand forced triggers, with the process being repeated for several input amplitudes.

A note here on procedure: it is important for this measurement that the period of the input sine-wave and the sampling period have a large least common multiple (LCM), to ensure a complete sampling at all phases of the input. For example: with a 1 GHz input sine-wave and a 2 GHz sampling rate, at most two unique voltages will be sampled, making amplitude

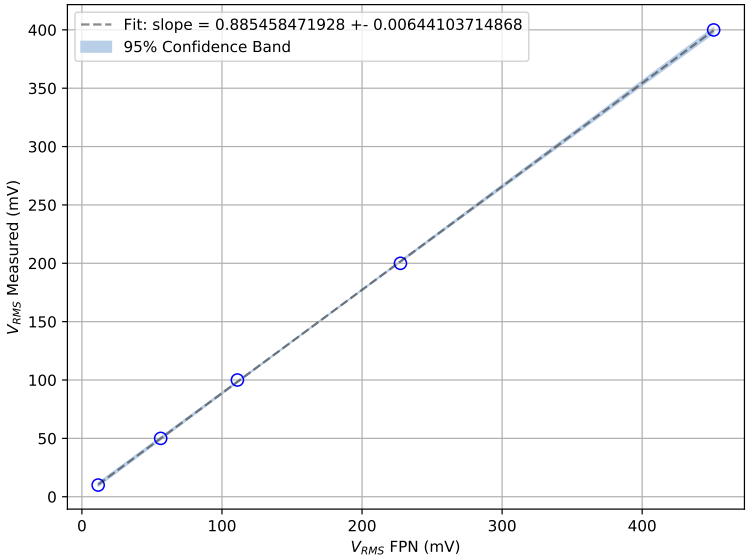

Figure 2.16: Example data and best linear fit for the ARIANNA gain calibration procedure. The x axis indicates the FPN subtracted voltage from Equation 2.3, while the y axis is the measured V_{RMS} from the oscilloscope. The shaded region represents the 95% confidence bound on the fit parameters.

reconstruction very difficult. Ideally, the ratio of the signal frequency and sampling rate f_{sig}/f_{samp} should be irrational.

For each input channel, a separate linear fit is made relating the V_{RMS}^{sig} of the signal generator to the V_{RMS}^{FPN} of the FPN subtracted ADC values scaled according to the slope in Eqn. 2.3. Since, by construction, the FPN subtraction removes any DC offset, the y-intercept of the fit is neglected, and the linear relationship between FPN subtracted voltage (V_{FNP}) and signal voltage (V_{sig}):

$$V_{sig} = G \times V_{FNP} \tag{2.4}$$

is used. The gain correction factor G is unique for each input channel of each ARIANNA

DAq board. Typical values for G are ≈ 0.9, indicating a roughly 10% systematic error on the non-calibrated voltages one would naively calculate from Eqn. 2.3. We find that for voltages below 500 mV, the linear relationship is quite good, with a $\approx 1\%$ error on the slope.

2.2.3 Threshold Calibration

Since triggering of the SST is done in analog by dedicated circuitry (see Subsection 2.1.2 for details), the trigger thresholds for each input channel must be calibrated separately from the DAq. For this procedure, the SST is set to either high-only or low-only triggering at a specified digital-to-analog converter (DAC) value. The DAq is provided with 50 ns wide square pulses from an arbitrary pulse generator, and the trigger rate is measured as a function of pulse amplitude. This data is fit to a Gaussian CDF such that the voltage at which the station triggers for 50% of pulses, corresponding to a trigger rate of 500 Hz, is taken to be the threshold voltage corresponding to the programmed DAC value. The comparators are demonstrated to have a very sharp turn-on of well less that 1 mV (Figure 2.17).

This procedure must be repeated for the high-only and low-only thresholds, since these are handled by separate comparators. Linear best fits are calculated separately for the high and low thresholds such that:

$$V_{thresh} = a + b \times DAC \tag{2.5}$$

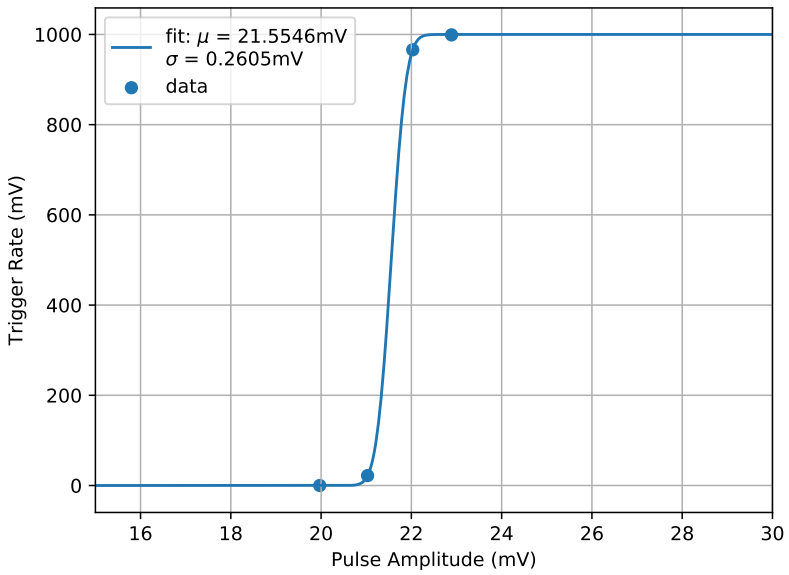

Figure 2.17: Trigger rate as a function of input pulse amplitude for a single high-only trigger of the ARIANNA DAq. Here the pulse rate was set to 1 kHz.

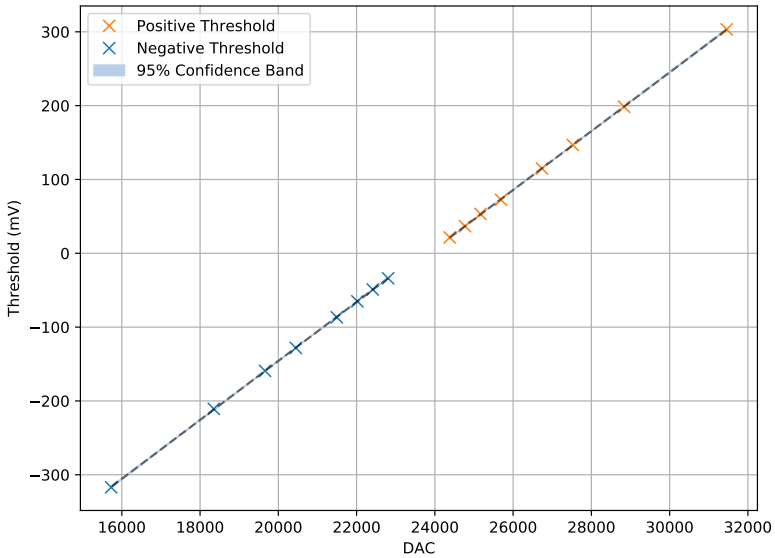

Figure 2.18: Example result from the ARIANNA threshold calibration. This particular example is for an 8ch SST board, which has a 16 bit DAC. The shaded region represents the 95% confidence bound on the fit parameters.

2.2.4 Setting Trigger Rates

In the field, thresholds are tuned by adjusting the high and low threshold DAC counts on each channel to attain a desired trigger rate. We typically desire a thermal trigger rate of $1-10\,\mathrm{mHz}$ such that events can be transferred to UCI in real time. Currently, this process is somewhat complicated by the limitation in our event readout rate of $\approx 1.2\,\mathrm{kHz}$. This means that we can only remotely measure trigger rates for a single channel high-only or low-only trigger which corresponding to a threshold of about 5σ above thermal noise V_{RMS}, which is well above our desired threshold.

This hurdle is overcome by a multi-step process. First, DAC counts corresponding to $\approx 5\sigma$ thresholds are found by tuning each channel's high-only and low-only rates to be in the range $550-600\,\mathrm{Hz}$. Since the thermal noise follows a symmetric Gaussian distribution, matching the high-only and low-only rates ensures that thresholds are set symmetrically about the DC baseline. Next, the DAq is set to require a high-and-low coincidence to trigger and the DAC thresholds are symmetrically restricted to achieve a single channel trigger rate of $50-60\,\mathrm{Hz}$, which corresponds to a threshold of $\approx 4\sigma$. Finally, once all channels are individually tuned, the majority logic trigger requirement is imposed and the station is set to normal running operation.

This process is automated by a script running on the Snowflake server at UCI, and takes a couple hours to fully tune a station (all stations can be tuned in parallel). The main time constraint comes from the requirement that each new tested threshold corresponds to a new configuration which must be sent to the station (see Fig. 2.3), and the time between communications being capped above $120\,\mathrm{s}$ for operational safety. While the process is somewhat cumbersome, thermal trigger rates are sufficiently stable that this tuning only needs to occur a few times a season.

With additional development, it should be possible to sample the trigger rates from the comparators without reading out the SST, which should increase the maximum measurable in situ trigger rates sufficiently to directly set 4σ high-only and low-only trigger thresholds for each channel. This would likely reduce the threshold tuning process from hours to seconds, and is a necessary improvement for a future array of many hundred stations.

2.3 Performance of the ARIANNA HRA

2.3.1 Station Livetime

The ARIANNA hardware has shown itself to be highly reliable over multi-season operation in Antarctica. Long term operation of the HRA stations has been documented in [44], [45], [24], and [46], with stations regularly achieving 90% livetime for extended periods (See Figure 2.19).

The useful livetime for analysis is easily calculated from the recovered data. Each data sequence contains a record of the trigger start and trigger stop times, which are simply subtracted to measure the livetime for that sequence. Sequences where triggering is disabled, communication peripherals are active during the data taking window, or heartbeat pulses are active during the data taking window are not counted towards the useful livetime. As an additional correction, a penalty is imposed to account for the deadtime due to DAq readout and event storage. The 4 channel SST based DAq can trigger and save events at a maximum rate of $\approx 75\,\mathrm{Hz}$, so we impose deadtime $\delta t_{store} = 1/75\,\mathrm{Hz} = 13.33\,\mathrm{ms}$ for each saved event. During normal operation, when trigger rates are stably below $10^{-2}\,\mathrm{Hz}$, this is a $< 0.02\%$ effect.

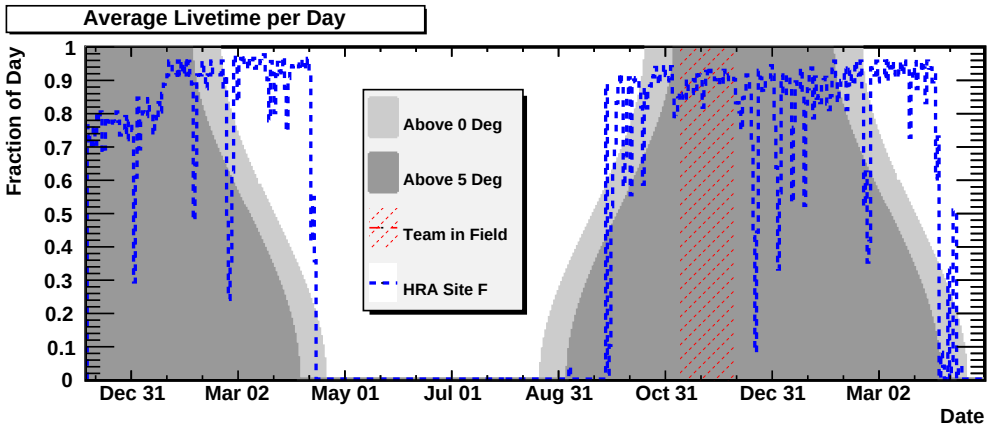

Figure 2.19: Livetime fraction per day for an HRA station at Site F, from December 2015 to April 2017. The grey shaded region shows the fraction of time the sun is above a certain elevation per day. The blue dashed line represents useful data taking time for analysis, adjusted for data transmission time and DAq deadtime due to event readout. Station operation configurations were optimized for livetime in mid January 2016. Large dips are due to a combination of bulk data transfers and some particularly stormy periods. Stations typically show livetimes near 90%, with stations averaging 145 days of total lifetime per station in the 2016-2017 season.

There are two main contributors to the deadtime of ARIANNA stations (besides the lack of power during the winter). Firstly, any time a station spends communicating over its wireless radios it is not taking data. With a proper setting of the communication period, this deadtime can be kept to a minimum. However, due to it's nature as a pilot array, the HRA is often configured to communicate more often then would be optimal from a livetime perspective, in order to allow for easier monitoring and quicker response to changes in detector status. As a result, HRA stations are not typically operating at maximum livetime efficiency.

The second main contributor to deadtime is caused by intermittent issues with AFAR communication. Due to the asynchronous nature of the HRA stations, communication windows of multiple stations often do not overlap, which makes it difficult for stations with weaker connections to the Mt Discovery repeater to successfully mesh through stations with a stronger link. The result is that some data is not transferred in real time. Additionally, in the default operating mode (See Figure 2.3), stations that are unable to connect to the repeater will spend a full minute trying to connect before falling back to Iridium comms. Much of the

data that is not collected in real time can be collected remotely through bulk data transfers, wherein the afars in stations which are branches in the network are held on so that stations with weaker connections can reach the repeater. This process can take several hours a day over a few days, depending on the amount of data that needs to be recovered.

2.3.2 Sources of Noise and Background

ARIANNA's Moore's Bay site is remarkably radio quiet, but there still exist some sources of background which must be considered. The bulk of triggered events are random in nature, either generated by thermal noise in our amplifiers, or from galactic radio emission. This type of background is easily discriminated from neutrino signal by a template matching procedure (Section 5.2.1), and trigger rates are managed by requiring multi-channel trigger coincidence (Section 2.1.2).

The stations also record occasional short bursts of narrow-band anthropogenic noise from air traffic control, and similar sources (Figure 2.20). Since the neutrino signal is broad-band in nature, a simple cut against highly peaked frequency spectra is effective at removing this background. We find that the $L1$ single frequency suppression parameter is effective at reducing these backgrounds while maintaining a signal efficiency of $1 - 1.8 \times 10^{-5}$ (see Section 5.2.2).

Another source of noise are events which are associated with periods of storm and high winds at the ARIANNA site. These stormy periods generate bursts of high events rates, which are somewhat pulsed in nature, and match neutrino templates more closely than thermal noise. The exact mechanism behind this RF noise is not yet understood, however, we will show that they can be efficiently vetoed based on their waveform properties (Section 5.3).

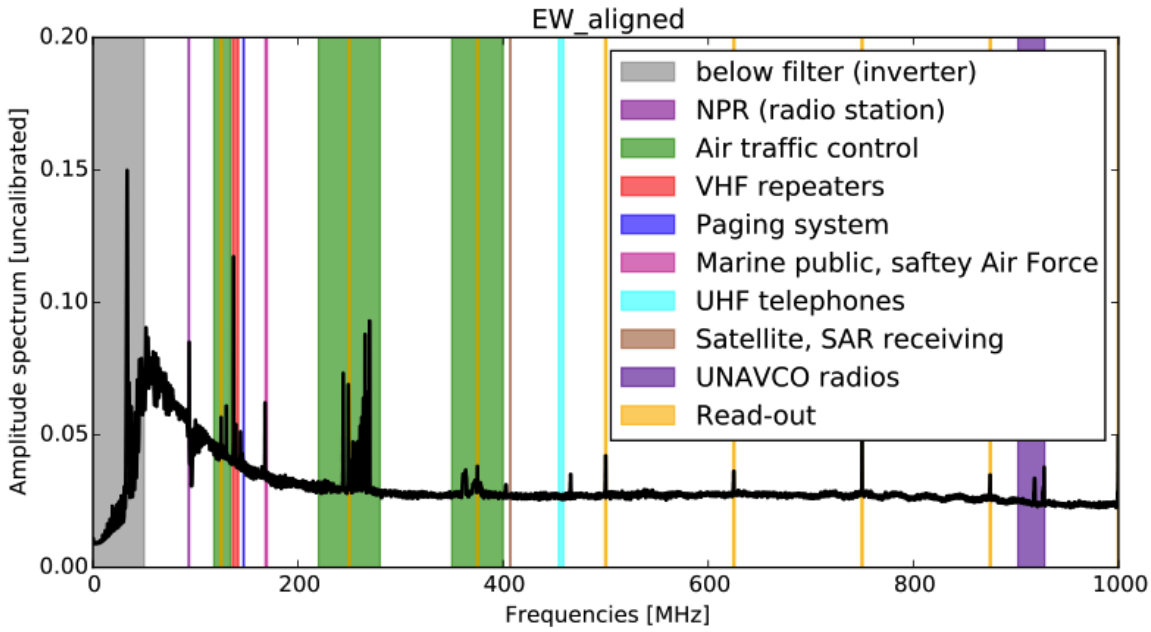

Figure 2.20: Measuremnt of noise environment at Moore's Bay. Data was recorded using a 50 MHz LPDA antenna fed into an oscilloscope. Most high significant noise is narrow band in nature, and can be associated with known anthropogenic sources. For this measurement, the antenna was horizontally polarized, and pointed in the direction of McMurdo station (See Figure 2.15), so it represents a pessimistic background scenario.

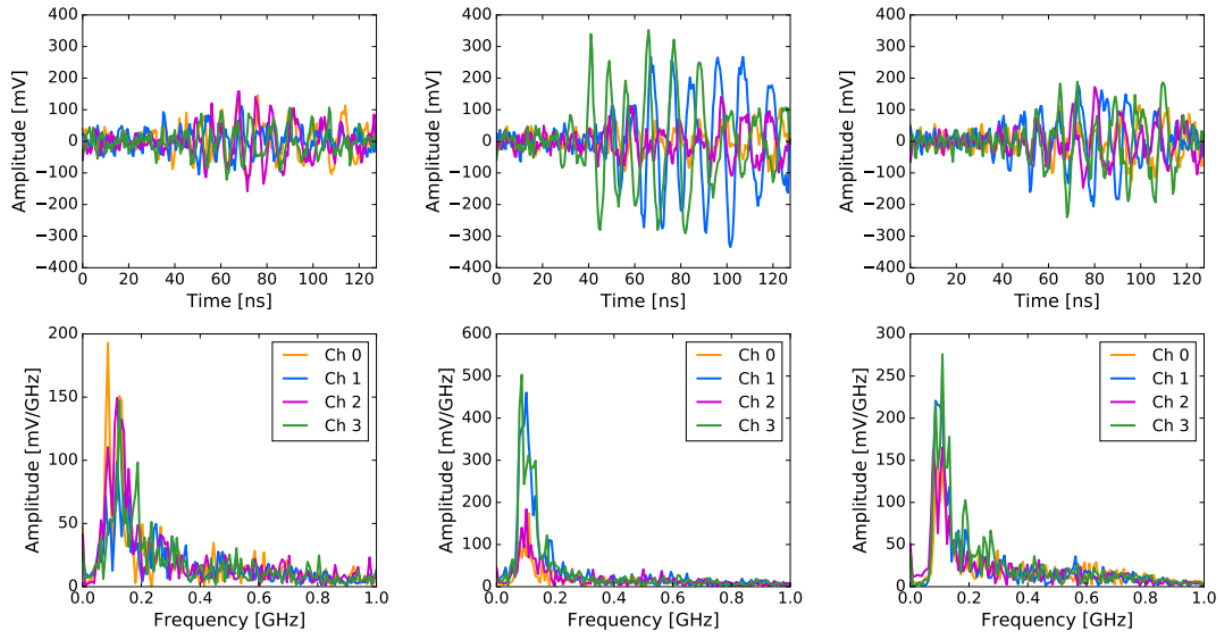

Figure 2.21: Some example cosmic ray signals in HRA stations, identified by coincidence with positively identified cosmic rays from the dedicated cosmic ray station (Section 2.4.3). From [20].

The primary background of concern for ARIANNA comes from atmospheric cosmic ray showers. These showers generate radio pulses in a similar process to those initiated by neutrinos in the ice, and as such, generate similar waveforms in the ARIANNA detector. Future designs for ARIANNA account for this by including upward facing antennas. In this way, upward going signals (neutrinos) can be easily distinguished from downward going signals (cosmic rays) due to the directional gain of the LPDA's. A number of cosmic ray events have been identified at the Moore's Bay site by the cosmic ray prototype station [20] and the updated 8 channel cosmic ray station (Section 2.4.3). These upward facing antennas are not yet incorporated in the HRA stations, however, so cosmic rays remain a significant background. The impact cosmic ray air showers will be discussed in greater detail in (Chapter 5).

2.3.3 Angular Reconstruction

Reconstruction of the signal arrival direction for ARIANNA stations has been demonstrated to the sub 1° level. Measurements using pulses which were bounced off the ice/sea water interface at Moore's Bay are presented in [44] and [47].

Here, we will present a complimentary measurement of the angular reconstruction precision, taken from in situ radio pulses with arrival directions significantly off the boresight of the LPDA's. During the 2017-2018 Antarctic field season tests were performed in which a piezo-electric pulser, designed and constructed at the University of Kansas, was lowered down the already existing South Pole Ice Core (SPICEcore) bore-hole. Pulses were detected by the ARIANNA South Pole Pilot Station (Section 2.4.5), and the time delay between parallel downward facing antennas calculated via the maximum cross-correlation (see Section 5.2.1 for details) was used to reconstruct the signal arrival direction.

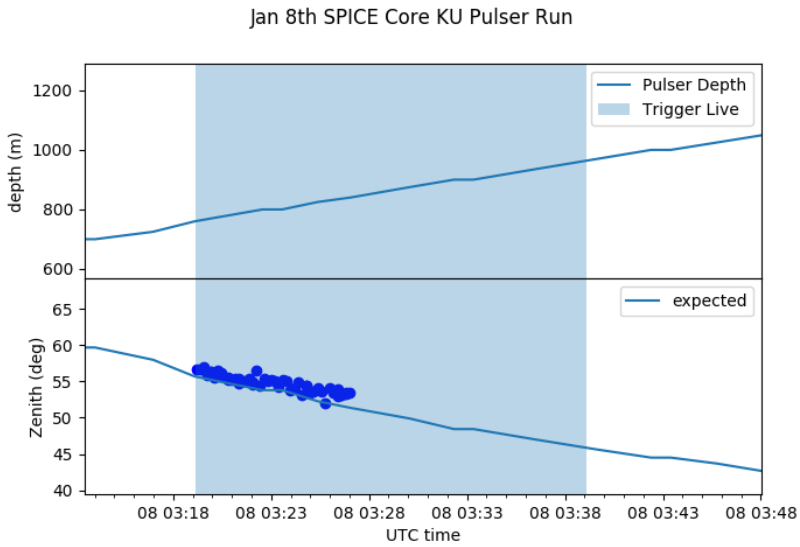

Figure 2.22: KU SPICEcore pulser location vs time, along with expected and reconstructed zenith angle.

Based on the depth vs time logs from the winch operators, geometric ray tracing was used to calculate the zenith angle of the signal of the detector using the best fit to the South Pole ice density profile shown in Figure 3.3. The calculated arrival direction is shown to track the pulser location (Figure 2.22), and while a systematic offset was observed, the precision was shown to be better than 1° (Figure 2.23).

2.3.4 Station Deployment

The design philosophy of independent and autonomously operating stations is incorporated into the deployment procedures for the ARIANNA HRA. Since a full ARIANNA array was intended to include many hundreds of stations, stations were designed in such a way as to be rapidly deployed by small teams. The HRA was deployed in two phases. The first three stations were deployed in the 2012-2013 Antarctic summer season. After a delay due to the US Government Shutdown in 2013, the remaining 4 stations were deployed during in 2014-2015. This was my first deployment with the ARIANNA team, and I directly participated in the construction of these four stations.

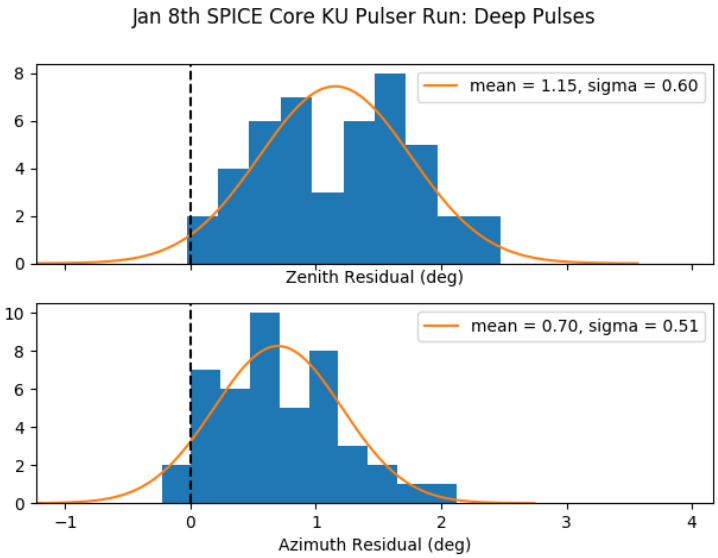

Figure 2.23: Residuals of the zenith reconstruction, showing sub-degree angular reconstruction precision.

Since Moore's Bay is a helicopter supported site, resources and equipment are limited. Equipment was often dragged the 1 km distance between stations on sleds (this trip takes 15-20 minutes, depending on the burden), with a snowmobile used for quicker transport of heavy items[2], such as the solar panel towers.

Pre-assembly of the solar panel towers was done by hand. The assembled tower was stood up by a team of four, and guyed down to wooden dead-men anchors using Phillystran cables. Four people would then use shovels to dig out narrow trenches in which to place the downward facing LPDA antennas. A this point, the majority of the physical work is done. Team members then share the remaining work of measuring antenna positions, and cabling the antennas. Since the LPDA's are deployed at the surface with easy physical access, the final antenna positions can be directly measured by tape measure, and a laser level is used to determine height offsets. The positional accuracy of the antennas is estimated to be ± 3 cm in x/y and ± 1 cm in z, with angles fixed to within 2° of vertical.

[2]The use of the snowmobile was found not to be strictly necessary, and so it was not used for the deployment of other ARIANNA stations in later seasons.

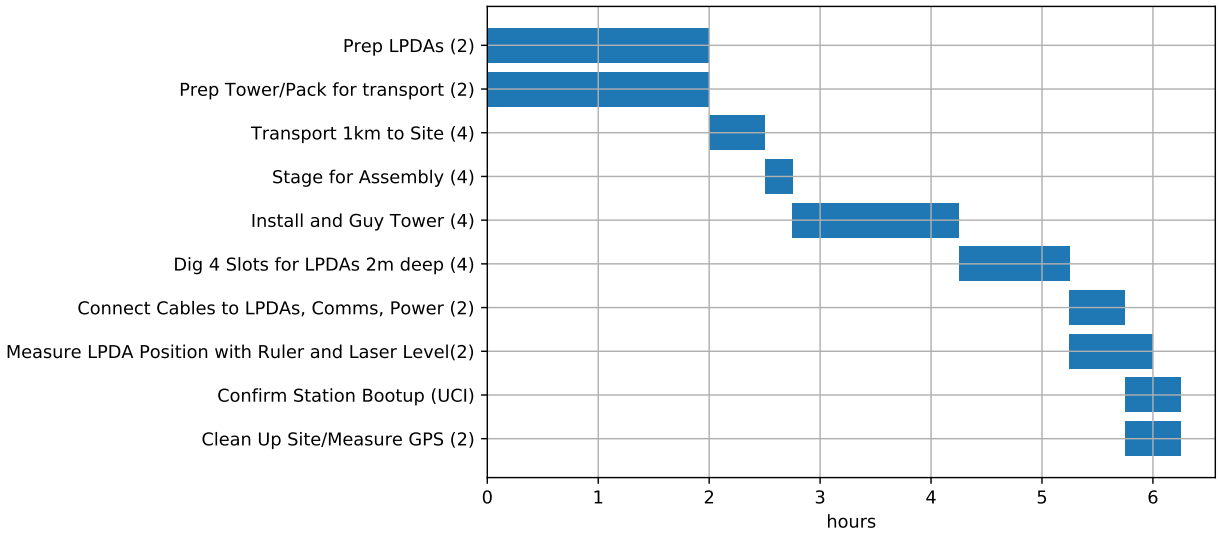

Figure 2.24: Gantt chart showing the deployment time-line for an ARIANNA station. Some tasks require all four team members, while others can be parallelized (the number of people engaged in each step is the number in parenthesis). The preliminary work can be performed in advance by separate personnel, significantly shortening the deployment time.

Once the station is powered on, monitoring is passed off to personnel at UCI, who are in contact with the field team via Iridium satellite phone.

All told, a team of four graduate students (with some help from a PI) can fully deploy an ARIANNA station in approximately 4 hours, plus approximately 2 hours of preparatory time. For a breakdown of the deployment time-table, see Figure 2.24.

What we have shown so far is valid for a surface station. Designs which include antennas at significant depth, such as the "strawman" design presented in Section 1.4, introduce added complexity. As a thought experiment, we will propose a deployment schedule for an ARIANNA like station which includes a set of 4 downward facing LPDA's, 4 upward facing LPDA's, an array of 4 vertically polarized dipole antennas at a depth of 5 m, and a string of dipoles at 10 m, 20 m, and 30 m. This station will be deployed at a site, such as near the South Pole Station, where a power grid has already been constructed, so we will neglect the solar panel tower.

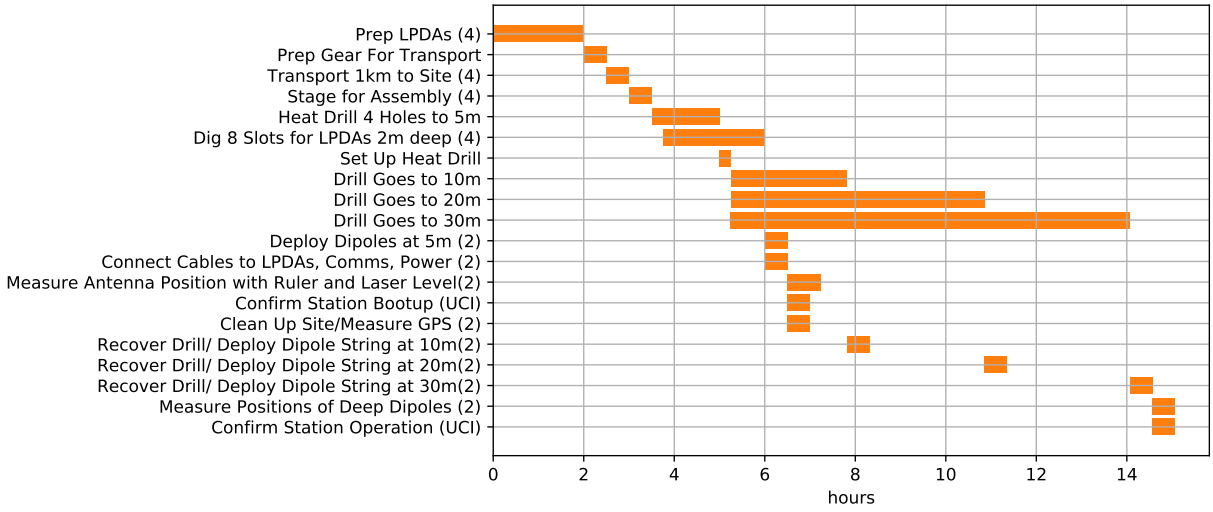

Figure 2.25: Gantt chart showing the deployment time-line for a "strawman" station with dipoles down to 30 m. The number of people engaged in each task is shown as the number in parenthesis. The heat drill takes significant time to reach depth, but this is mostly passive time, which can be used for other tasks.

Holes for the vertical dipoles will be drilled by a set of four heat drills. Such heat drills, developed by Aachen University in Germany, were used by the ARIANA field team in December 2016 and were operated to a depth of 20 m, though they are capable of depth of 50 m or more. The drills were logged at a rate of 4 m/h near the surface, slowing down to about 3 m/h by 20 m. The drilling of the holes takes substantial time, but much of it is inactive, as the heat drills can can operate mostly unsupervised.

A time-line for a "strawman" station deployment is presented in Figure 2.25. The conclusion is that, with appropriate equipment, a station design incorporating vertical bicone antennas down to depths of 30 m can be deployed by a team of four people in a single day. This can be made even more efficient by allocating the preliminary work, such as the assembly of LPDA antennas, to separate personnel.

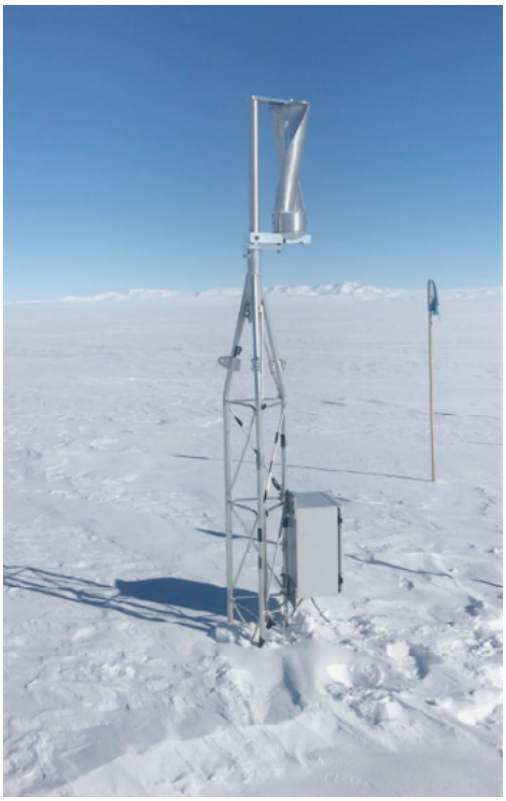

Figure 2.26: Photo of the vertical axis wind turbine, developed at Uppsala University, which was deployed during the Antarctic summer of 2017-2018, and has provided power to ARIANNA site E throughout the winter.

2.4 Ongoing Research and Development

Due to the HRA's nature as a pilot array, there are active areas of development that are underway, but which are not considered as part of the HRA. In this section, we will discuss some of these developments, along with some preliminary results.

2.4.1 Wind Power for Autonomous Stations

It has been a goal of the ARIANNA to develop a system for wind power in order to extend the operation of autonomous stations into the winter months, when the sun does not raise above the horizon. The challenges of engineering such a system, which must survive the extreme

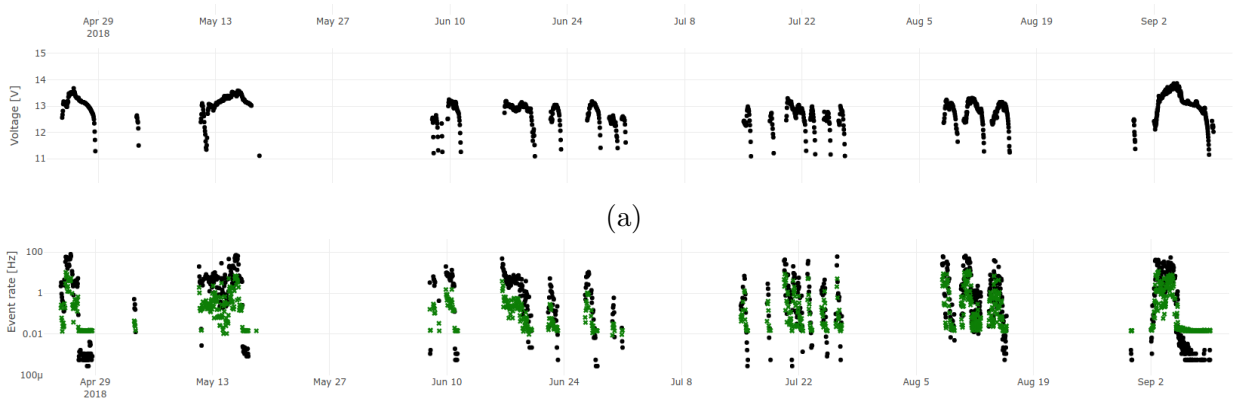

Figure 2.27: (a) Battery voltages reported by the ARIANNA station at site E during the winter months, showing the operation of the newly designed vertical axis wind turbine. (b) Event rates vs time, showing rates before (black dots) and after (green x's) the on-board L1 trigger.

cold of the antarctic winter while also being sufficiently radio quiet not to overwhelm the station, has proven to be great. However, substantial progress has been made with a vertical axis wind powered generator developed in collaboration with Uppsala University.

This newly designed turbine was installed as on the HRA station at site E, and at the time of writing, continues to power the station during the winter (see Figure 2.27) with a livetime fraction of $\approx 23\%$. The operation of this wind-gen also produced significantly elevated trigger rates in the nearby station, so more development is still needed to reduce RF emission. Some simple improvements, such as improving the greases and increasing the blade height should lead to substantially greater uptimes.

2.4.2 The 8 Channel SST Board

The 4 channel design of the HRA stations represents a minimum level of functionality, which is useful for demonstrating hardware reliability, but is not ideal as a fully capable detector. One vital requirement of a complete ARIANNA design is the ability to very reliably tag cosmic ray air showers which, due to their similar emission mechanism, can closely mimic

neutrino induced Askaryan pulses. In principle, a detailed analysis of waveform properties may be capable of distinguishing air showers from neutrinos; however, the most robust and reliable separation can likely be made by breaking the degeneracy between upward going neutrino signal and downward going cosmic ray signals signals. By installing upward facing LPDA antennas, the LPDA's directionality can be leveraged to make this distinction, allowing for a cosmic ray veto based on the power ratio in the upward and downward facing antennas, as was discussed in [24].

In order to manage these additional antennas, a new version of the SST DAq board was developed which has 8 input channels. The design remains essentially the same as the 4 channel board (Section 2.1.2), except that the board contains two copies of the SST chip and supporting circuitry, with each chip handling 4 channels. These new boards were tested/calibrated at UCI over the summer of 2017 and were deployed in three separate prototype stations during the 2017/2018 Antarctic field season, which will be discussed in the following subsections.

2.4.3 Moore's Bay Cosmic Ray Station

In order to expand upon the success of the 4 channel ARIANNA cosmic ray station presented in [20], that station was replaced by a new 8 channel cosmic ray station with the usual 4 downward facing LPDA's, as well as 4 upward facing LPDA's. This station has the same neutrino capabilities as the 4 channel HRA stations, with the added capability for detecting cosmic ray air showers. Since the downward facing antennas are in the same layout as the HRA stations, this cosmic ray station will be an important tool for validating the back-lobe response of the HRA stations to air shower signals.

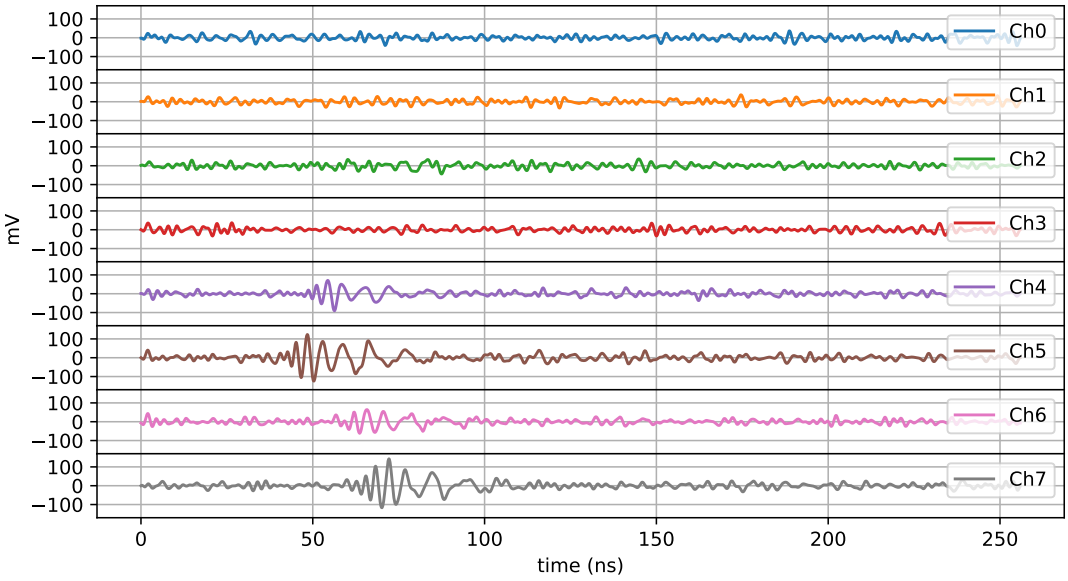

Figure 2.28: Signal from a cosmic ray air shower in the 8 channel ARIANNA cosmic ray station at Moore's Bay. Channels 0-3 are downward facing, while 4-7 are upward facing. Similar signals are seen in pairs of co-polarized channels (4/6 and 5/7), with time offsets consistent with a plane wave. The apparent up/down anisotropy is an important factor in tagging cosmic rays WRT the neutrino search.

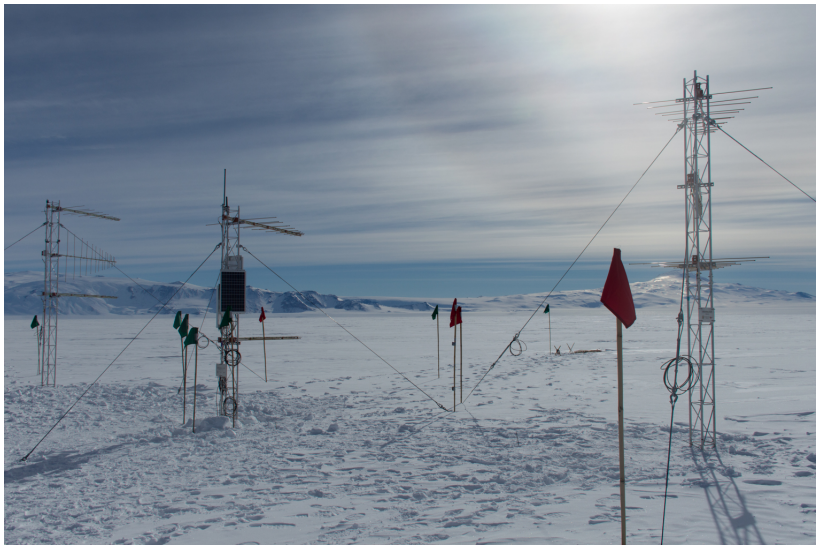

Figure 2.29: A photo of the 8 channel upgraded HRA station deployed at Moore's Bay, showing Mt Discovery in the background.

The cosmic ray search and analysis for the 2017 and 2018 analysis is still ongoing. But a number of cosmic ray candidates have been preliminarily identified using a template matching procedure, as was done in [20]. An example of a cosmic ray candidate is shown in Figure 2.28.

2.4.4 The Horizontal Cosmic Ray Station

The ARIANNA DAq is agnostic towards antenna type and layout, and as such, many detector layouts are possible. In concert with the TAROGE collaboration, a Horizontal Cosmic Ray (HCR) station was developed and deployed at the Moore's Bay site [48]. The detection principle of this device relies on the τ double bang process (discussed in Section 3.6.2), where ν_τ interacting in nearby Mt Discovery produce τ leptons, which in turn produce air showers as they decay en route to the detector.

In the 2017/2018 Antarctic field season, this prototype was upgraded to an 8 channel system, with antennas placed on three separate towers (Figure 2.29). This significantly increased the

Figure 2.30: A photo ARIANNA South Pole pilot station, showing the Amundsen-Scott station in the background. Upward pointing antennas are visible, with three downward facing LPDA's and an ARA bicone antenna below the surface.

azimuthal reconstruction capability, which is essential for vetoing cosmic ray air showers which *do not* originate from the direction of Mt Discovery.

2.4.5 South Pole Pilot Station

Apart from Moore's Bay site, which is the location of the ARIANNA HRA, the East Antarctic Ice Sheet is another viable site for an ARIANNA style array. Results from simulation suggest that the longer attenuation length (which is a function of the colder ice near the surface) can lead to an overall increase in effective volume, even with the loss of the reflected signals present in Moore's Bay (see Section 4.2.3). Deploying such an array in the vicinity of South Pole Station would have the benefit of close logistical support and access to infrastructure, at the cost of a less clean noise environment.

In order to test the feasibility of an ARIANNA array near south pole, an 8 channel station was deployed near the site of ARA's wind turbine 3. This station contains the standard set of downward facing antennas, as well as 3 upward facing LPDA's, and a bicone dipole

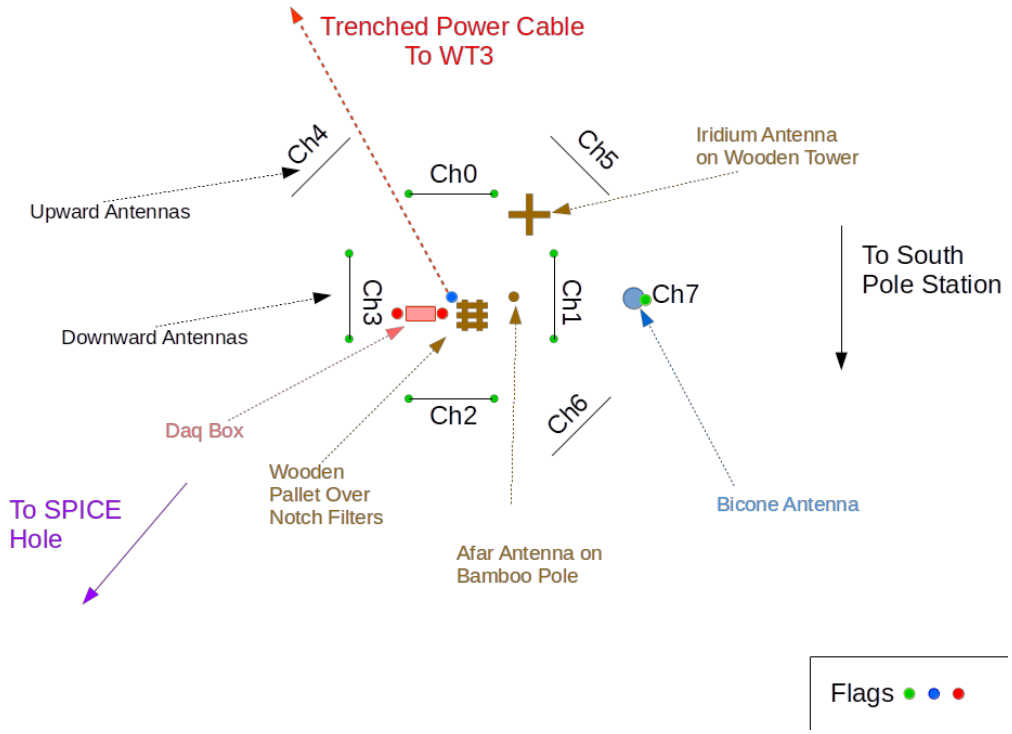

Figure 2.31: Digram of the ARIANNA South Pole pilot station, showing the antenna positions and orientation relative to South Pole landmarks.

antenna which is identical to those which are deployed in the ARA array [22] (Figure 2.31). In lieu of solar power and batteries, this station is powered on 40 V DC which is stepped down off of the 300 V from the South Pole Station's power grid, which allows uninterrupted operation over the winter.

While the noise background is greater near the South Pole than at the Moore's Bay site. To asses this background, a preliminary analysis was carried out, calculating the average correlation coefficient (χ, see Section 5.2.1) of triggered events to a set of neutrino templates, following the process outlined in Chapter 5. A full analysis of this data requires the simulation of a realistic neutrino set, which is still forthcoming. However, the distribution of neutrino events in χ averaged over all templates is not likely to be substantially worse than what is shown in Figure 5.5, since the low χ tail is pulled down by random noise. The result, shown in Figure 2.32 paints an optimistic picture for the prospect of surface based radio detectors near South Pole.

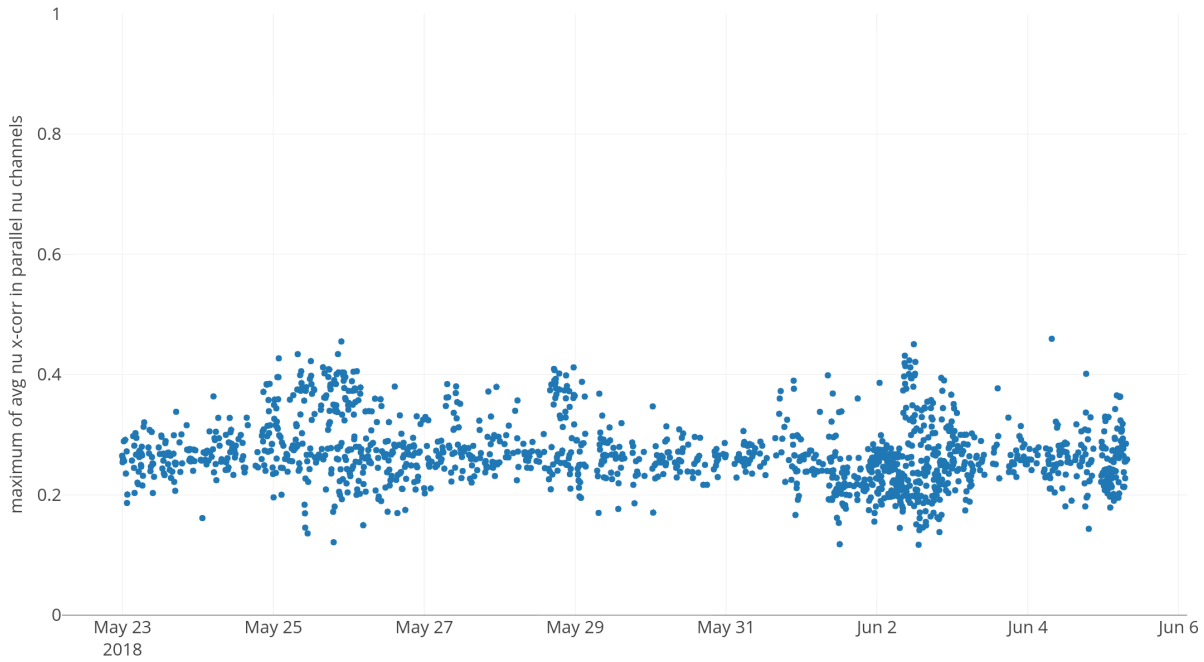

Figure 2.32: Results of a preliminary template matching analysis to a selection triggered events from the ARIANNA South Pole pilot station. The y-axis represents the average cross-correlation of the triggered event to a set of simulated neutrino templates. While different templates were used here, a comparison to the distribution of simulated neutrino signal in χ from the HRA analysis (Figure 5.5) would suggest that the noise background near South Pole station is acceptable WRT background rejection for a neutrino analysis.

Chapter 3

The ShelfMC Monte Carlo

Simulations to determine the sensitivity of the ARIANNA array are primarily performed using the *ShelfMC* Monte Carlo. *Version 0.0* of *ShelfMC* was developed by F. Wu from a fork of the *icemc* code originally developed for the ANITA collaboration at UCLA. *ShelfMC* has progressed through many iterative improvements, being brought to *version 1.0* by K. Dookayka. This version, which is documented in [49], was inherited by the author, and has since evolved to *version 2.0*. This chapter will summarize the overall framework of the *ShelfMC* Monte Carlo, and highlight the improvements in *version 2.0*.

The casino-like aspect of the Monte Carlo procedure comes in the random event generation. In the context of in-ice neutrino detection, a fiducial volume is chosen which completely surrounds the detector and contains all of the interaction medium in which an event can trigger the detector. In the case of an ARIANNA detector, the neutrino interaction length L_{int} (Table 3.1) is much longer than the size of this volume, so we can assume a uniform distribution of neutrino vertices within the volume. *ShelfMC* also chooses uniformly random arrival directions for the simulated neutrinos, and applies a geometrical weight factor to account for absorption of upward traveling neutrinos by the Earth (See Section 3.3).

$E\ (eV)$	$L_{int}\ (km)$
10^{15}	6517.85
10^{16}	2672.72
10^{17}	1200.14
10^{18}	567.57
10^{19}	291.90
10^{20}	154.12
10^{21}	84.24

Table 3.1: Water equivalent neutrino interaction length, based on all nucleon cross section in [25].

Mediator	Flavor	f_{had}	f_{em}	Notes
CC	ν_e	y	$1-y$	LPM effect on EM shower
	ν_μ	y	-	
	ν_τ	y	-	τ induced shower with $E_\tau = (1-y)E_\nu$
NC	all	y	-	

Table 3.2: Energy fractions in hadronic and electromagnetic showers (f_{had} and f_{em}) for all neutrino flavors.

The relevant shower parameter for determining the strength of the Askaryan effect in ice is the energy of the neutrino induced particle shower. The energy fraction of the primary neutrino which contributes to the shower is determined by its flavor, the mediator (CC vs NC), as well as the inelasticity y, which is defined as the fraction of energy that goes into the hadronic shower component. For ν_e CC interactions, the secondary electron induces an EM shower which is lengthened through the LPM effect [50]. For ν_μ, the muon loses energy through bremsstrahlung and does not contribute to the radio emission. For ν_τ the τ can decay, producing a hadronic shower with $E_\tau = (1-y)E_\nu$. For a summary, see Table 3.2.

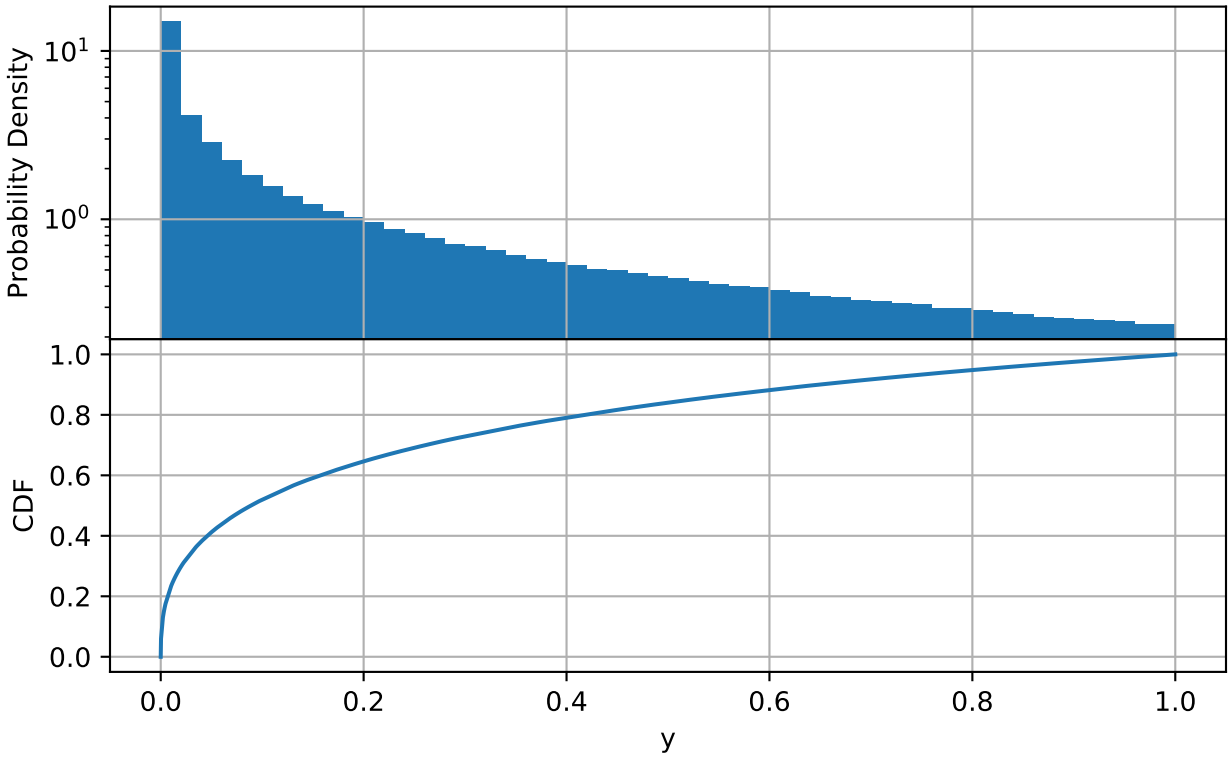

Figure 3.1: Probability distribution (top) and cumulative distribution function (bottom) for the inelasticity (y). Half of neutrino induced showers will have $Esh = yE_\nu < 0.1E_\nu$ in the hadronic shower.

Once a neutrino interaction vertex is generated, the signal path to the detector is calculated. The signal amplitude at the each antenna of the detector is calculated based on propagation losses, the emission angle with respect to the Cherenkov cone, and the antenna response. If the signal strength exceeds a pre-set threshold in enough antennas to satisfy the majority logic condition, then the event is saved as a trigger, with the appropriate weight factor to account for neutrino absorption before reaching the detector.

3.1 Improvements in ShelfMC Version 2.0

Here the various expansions and improvements which took place between *version 1.0* and *version 2.0* of *ShelfMC* are listed.

- Re-worked setup file handling to allow for easier addition of simulation parameters.
- Flexibility to allow multiple antenna types, and station configurations with arbitrary number, placement, and orientation of antennas.
- Added event list feature, allowing for cross-validation across different Monte Carlo packages.
- Allow for configurable index of refraction profiles with arbitrary scale factor. (Section 3.2.1)
- Calculate "shadow zone" upon initialization, based on index of refraction profile. (Section 3.2.3)
- Incorporated more accurate antenna modeling based on $\vec{\ell}_{eff}$ from WIPL-D simulations. (Section 3.5.1)
- Improved handling of τ double bangs. (Section 3.6.2)

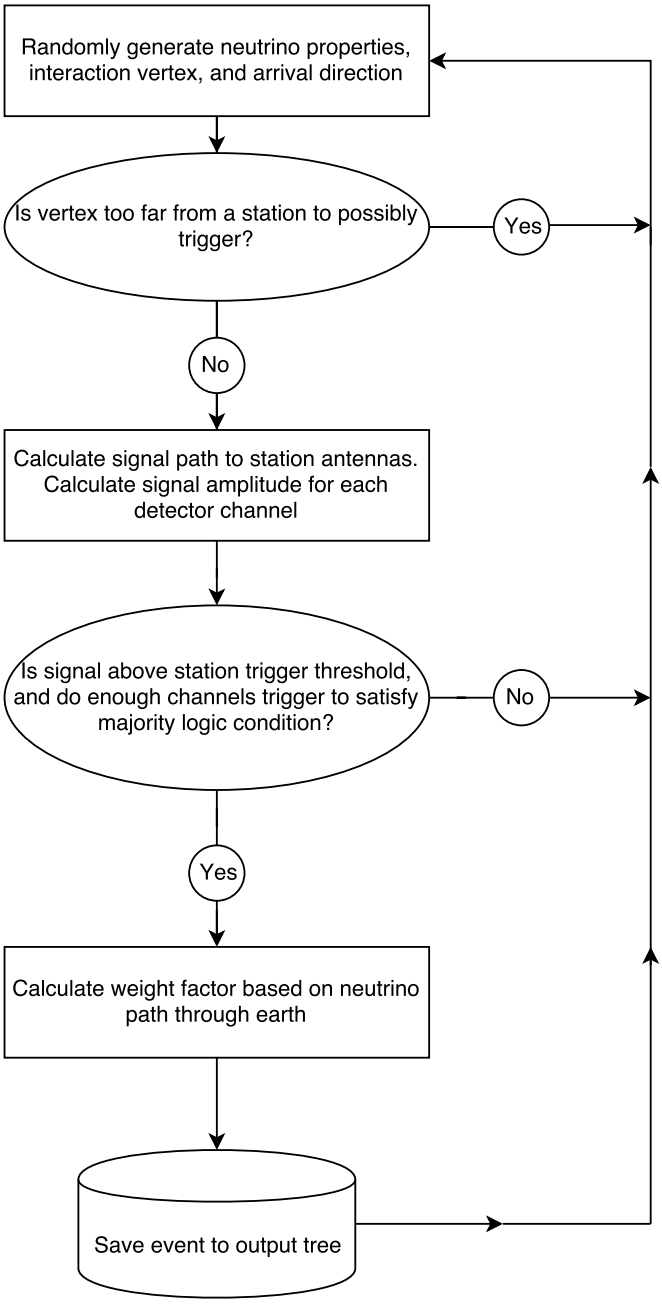

Figure 3.2: Basic Outline of ShelfMC procedure

- Addition of "horizontal propagation" mode, to allow for investigation of non-standard ray propagation that violates the shadow zone restriction. (Section 3.2.5)
- Numerous quality of life improvements, including helper scripts for easier calculation of effective volumes and plotting, as well as improved automation of parallel computing, and increased modularization for easier development.

3.2 Signal Propagation

3.2.1 Index of refraction profile

The changing density of the firn as a function of depth generates a continuously varying index of refraction (n), which will cause a bending of light as it passes through the firn. The density profile of the firn can be reasonably modeled by the equation:

$$\rho(d) = \rho_{ice} + (\rho_0 - \rho_{ice})e^{-d/C} \quad \text{where} \quad d > 0 \tag{3.1}$$

Where d is the depth below the surface, $\rho_{ice} = 0.9167 g/cm^3$ is the density of solid ice, ρ_f is the density of snow at the surface, and C is a characteristic length scale which depends on the details of the glacial deposition, and varies based on location. The index of refraction is extracted from the density using the empirical relation

$$n = 1 + 0.78\frac{\rho}{\rho_{ice}} \tag{3.2}$$

And therefore

$$n(d) = n_{ice} + (n_0 - n_{ice})e^{-d/C} \quad \text{where} \quad d > 0 \tag{3.3}$$

Where $n_{ice} = 1.78$ for solid ice, and n_0 is the index of refraction at the surface. Since density reduction in the firn is due to trapped air bubbles which are much smaller than the wavelengths of interest, the index of refraction is essentially frequency independent in our regime of interest [51].

For the Moore's Bay site the index of refraction profile is based off of measurements taken by the ARIANNA field team in 2016, converted to an index of refraction using Eqn. 3.2, see Figure 3.3. For the South Pole, we use firn density measurements reported by the SPICE collaboration.

3.2.2 Signal Path to Detector

In principle, it is possible to model the bending path of a light ray as it propagates through the firn. However, this is a relatively computationally expensive process in the context of ShelfMC, so we make an approximation.

For the purposes of calculating the propagation path from interaction vertex to the detector, the ice shelf is modeled as two slabs of uniform index of refraction. From the surface to the bottom of the firn, whose depth ($FIRNDEPTH$) is taken as $2C$, where C is defined in Equation 3.3 and taken to be $34.48m$ for Moore's Bay, the index of refraction is set to $NFIRN = 1.30$ to match the index at the surface. Below this depth, the index is set to $NICE = 1.78$ to match the index of the bulk ice. The signal path undergoes Snell's

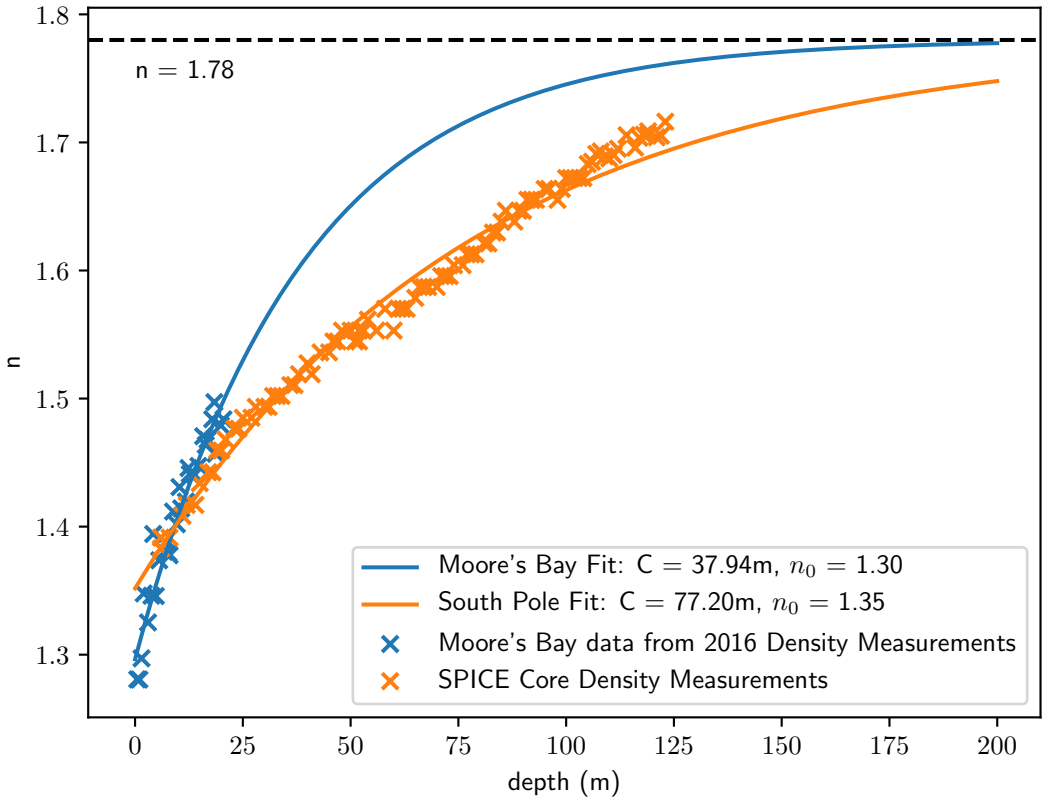

Figure 3.3: Best fit to Eqn. 3.3 for index of refraction profiles. Based on firn density measurements taken by the ARIANNA field team in Moore's Bay, and the SPICE collaboration at the South Pole.

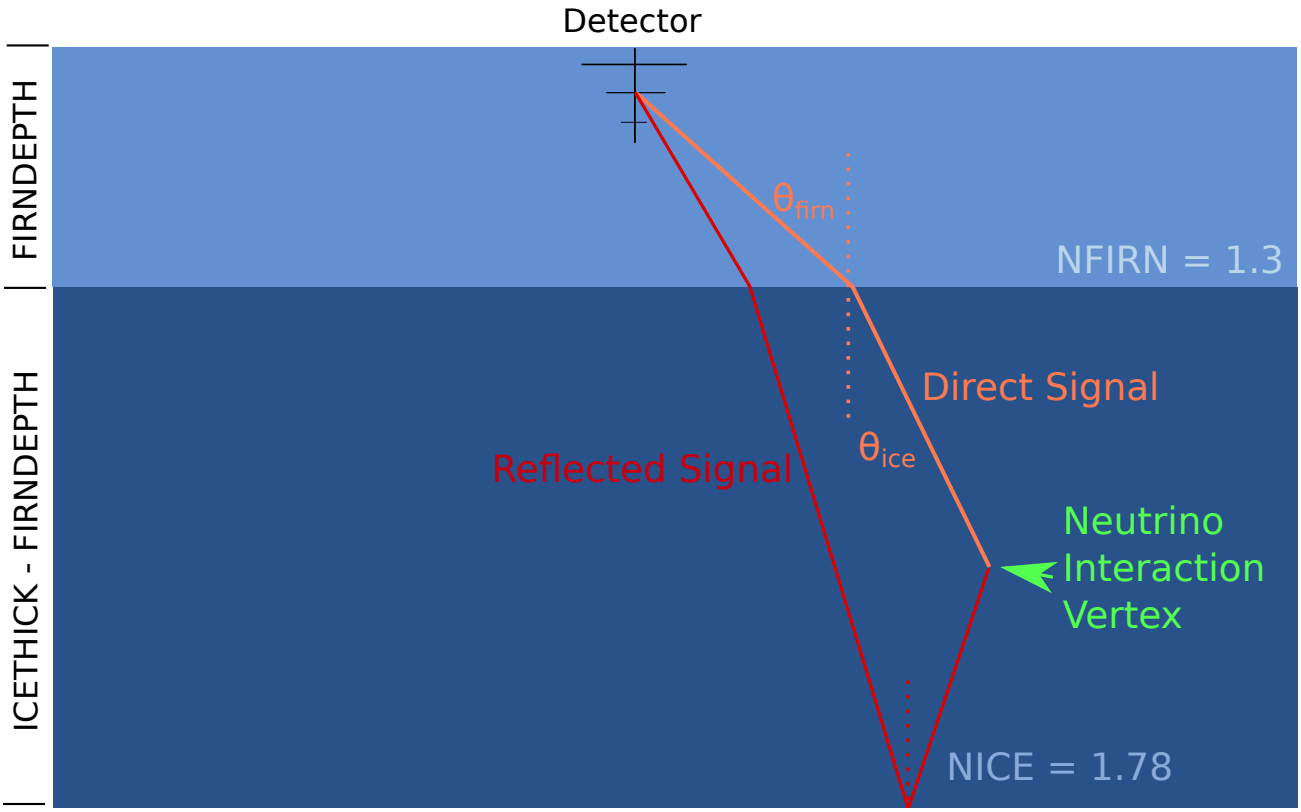

Figure 3.4: Diagram of *ShelfMC* ray tracing procedure. Rays are bent as if undergoing Snell refraction at a discrete boundary.

Law refraction at this boundary, such that $NFIRN \sin(\theta_{FIRN}) = NICE \sin(\theta_{ICE})$, see Figure 3.4. For vertices within the firn, the signal undergoes straight line propagation to the detector.

3.2.3 Ray Shadowing

As the rays which represent the propagation of radio waves through the ice experience a continually changing index of refraction, their direction of propagation changes according to Snell's Law. The relationship between the ray propagation zenith angles θ at two different depths in a continuous medium is precisely what one would expect from the discrete Snell's

Law equation:

$$n(z_0)\sin\theta_0 = n(z_f)\sin\theta_f \tag{3.4}$$

A consequence of this is that a ray originating at depth z_0 with propagation zenith θ_0 will be unable to propagate to depth z_f if $\theta_0 > \theta_{crit}$, where:

$$\sin\theta_{crit} = n(z_f)/n(z_o) \tag{3.5}$$

We can use Snell's Law to calculate the horizontal distance x traveled by a ray as it bends up through the firn from depth z_0 to z_f for a particular launch angle θ_0:

$$x(z_0, z_f, \theta_0) = \left|\int_{z_0}^{z_f} \frac{dx}{dz} dz\right| = \left|\int_{z_0}^{z_f} \tan\theta(z) dz\right| = \left|\sin\theta_0 \int_{z_0}^{z_f} \left[\frac{n^2(z)}{n_0^2} - \sin^2\theta_0\right]^{1/2} dz\right| \quad \text{where} \quad \theta_0 \leq \theta_{crit} \tag{3.6}$$

For a detector located at the surface, we are interested in the furthest horizontal distance for a given depth d where a an Askaryan pulse can reach the detector. This quantity will define a region, outside of which any neutrino interactions will not be able to trigger the station.

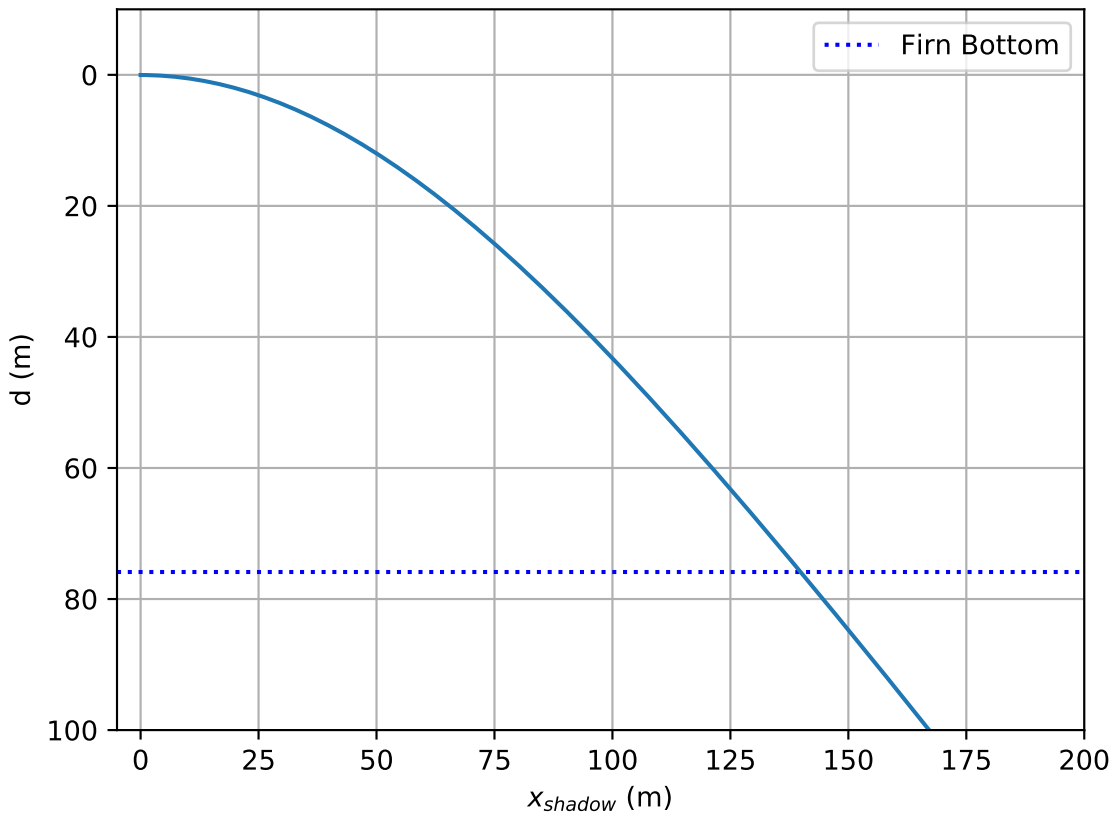

Figure 3.5: Shadow range x_{shadow} defined by Equation 3.7, using the best fit $n(d)$ for Moore's bay (See Figure 3.3). At depths below the firn, where $n(d) \approx n_{ice}$, the shadow zone boundary asymptotes to a constant slope defined by zenith angle θ_{crit} (Equation 3.5).

Setting $\theta_0 = \theta_{crit}$, we can use Equation 3.6 to define the shadow range x_{shadow}:

$$x_{shadow}(d) = \left| \frac{n(0)}{n(d)} \int_d^0 \left[\frac{n^2(z)}{n(d)^2} - \frac{n^2(0)}{n^2(d)} \right]^{1/2} dz \right| \tag{3.7}$$

This equation is numerically integrated upon initialization of the *ShelfMC* Monte Carlo to define a shadow zone boundary, beyond which neutrino events are vetoed (see Figure 3.5).

For a detector where the LPDA's are buried at some depth d_{ant} below the snow surface, the

ray path can be extended by grazing the surface before dipping down to the antennas. So, we make the correction for direct signals:

$$x_{max}^{direct}(d) = x_{shadow}(d) + x_{shadow}(d_{ant}) \tag{3.8}$$

For reflected signals, the ray path will first bend downward, reflect off the ice/sea water interface at a depth $d = d_{max}$, and then traverse the entire thickness of the ice shelf to reach the detector. All together, this gives us the following expression for the reflected signal:

$$x_{max}^{reflected}(d) = (x_{shadow}(d_{max}) - x_shadow(d)) + (x_{shadow}(d_{max}) + x_shadow(d_{ant})) \tag{3.9}$$

See 4.2 to see the effect of Equations 3.8 and 3.9 on the triggered neutrino vertex locations at the Moore's Bay site.

3.2.4 Propagation Losses

In addition to the geometrical $1/R$ factor, the E-field from Askaryan pulses on route to the detector also undergoes attenuation according to:

$$\varepsilon(r) = \frac{\varepsilon_{1m}}{r/\mathrm{m}} e^{-\frac{r}{\ell}} \tag{3.10}$$

Where ℓ is the field attenuation of ice, and ε_{1m} is the measured (or calculated) electric field

amplitude at $r = 1\,\mathrm{m}$.

This picture is complicated somewhat by the fact that ℓ is both a function of temperature and frequency. It is, however, possible to separate the temperature and frequency components as $\ell(T, f) = \ell_T(T)\ell_f(f)$. The frequency dependence has been measured at the Moore's Bay site to be linear, with a slope $\frac{\partial \ell}{\partial f} = -180 \pm 40\,\mathrm{m/GHz}$ [52]. However, these results have not yet been incorporated in to *shelfMC*, so we will take the simplifying approximation $\ell_f = 1$.

Once the temperature of the ice is known as a function of depth, an expression for $\ell(z)$ can be derived. *ShelfMC* uses the following ice shelf parametrization for $\ell(z)$, adapted from [53]:

$$\frac{\ell(z)}{\mathrm{m}} = 1250 \cdot 0.08886 \cdot \frac{\bar{\ell}}{262\,\mathrm{m}} \exp\Big[-0.048827\big(225.6746 - 86.517596 \log_{10}(848.870 - \frac{420z}{z_{max}})\big)\Big] \tag{3.11}$$

where $\bar{\ell}$ is the depth-averaged attenuation length, $z > 0$ is the depth below the surface, and z_{max} is the depth of the ice shelf.

For a neutrino signal originating at interaction depth z_{int}, we are interested in the average attenuation length over the depths that the neutrino signal must travel to reach the detector. For a direct signal, $\bar{\ell}_{up}$ will be the average attenuation length from the z_{int} to the surface.

$$\bar{\ell}_{up} = \frac{1}{z_{int}} \int_0^{z_{int}} \ell(z) dz \tag{3.12}$$

For a bounced signal, $\bar{\ell}_{down}$ will be the average through the full ice depth, plus the distance

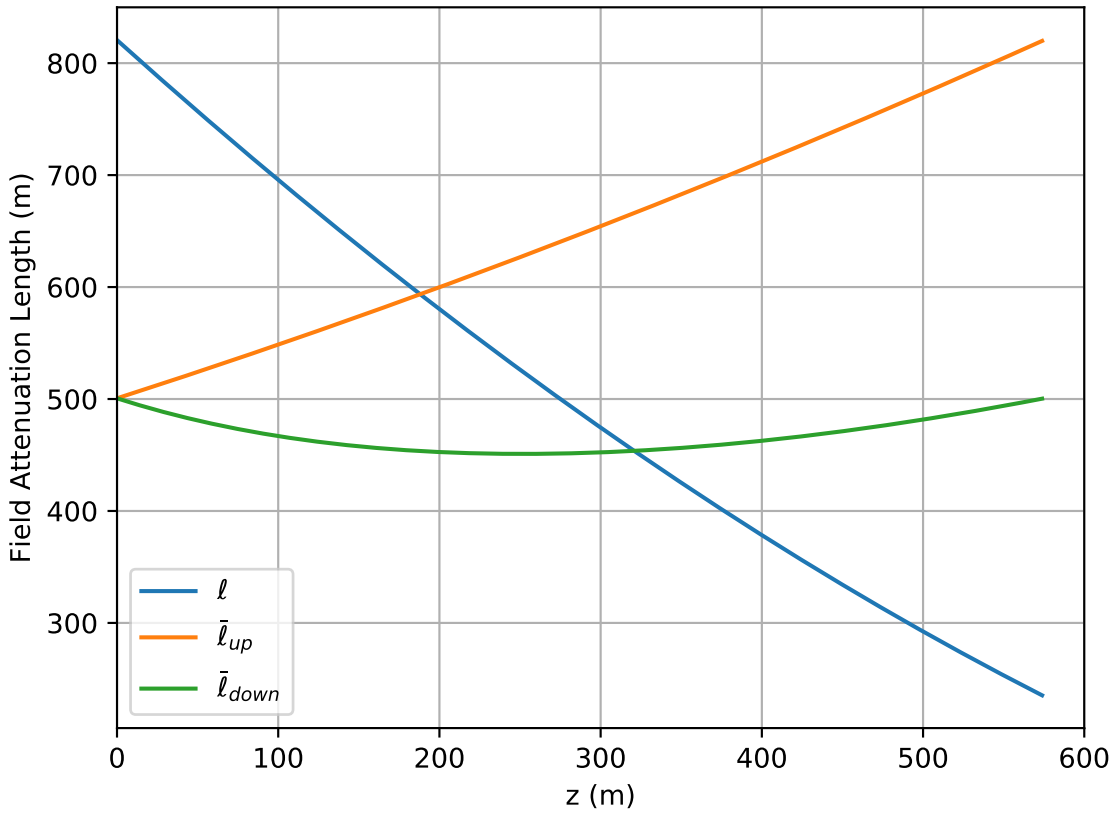

Figure 3.6: Attenuation length (ℓ), average attenuation length for direct signals ($\bar{\ell}_{up}$), and average attenuation length for reflected signals ($\bar{\ell}_{down}$), with z measured down from the surface. Here we have taken $\bar{\ell} = 500\,\text{m}$, which represents a weighted average over frequency according to the gain of the LPDA, and $z_{max} = 575\,\text{m}$. See Equations 3.11, 3.12, and 3.13.

from z_int to the bottom.

$$\bar{\ell}_{down} = \frac{1}{z_{max} + (z_{max} - z_{int})} \left[\int_0^{z_{max}} \ell(z) dz + \int_{z_{int}}^{z_{max}} \ell(z) dz \right] \tag{3.13}$$

The bounced signal also experiences a reflection loss at the ice/sea water boundary according to the reflection coefficient R. All together, the total propagation losses are for direct and

reflected signals are modeled as:

$$\varepsilon_{direct} = \frac{\varepsilon_{1m}}{r_{direct}/\mathrm{m}} e^{-\frac{r_{direct}}{\ell_{up}}} \tag{3.14}$$

$$\varepsilon_{reflected} = \sqrt{R}\frac{\varepsilon_{1m}}{r_{reflected}/\mathrm{m}} e^{-\frac{r_{reflected}}{\ell_{up}}} \tag{3.15}$$

where r_{direct} and $r_{reflected}$ are the total path lengths for the direct and reflected rays (see Figure 3.4).

3.2.5 Horizontal Propagation Model

Spurred on by preliminary results that would eventually lead to the publication of [54], a model was developed for radio classically forbidden signal which travels horizontally past the "shadow zone"[1]. In this model, a ray propagating from point $p_0 = (x_0, y_0, z_0)$ to $p_f = (x_f, y_f, f, z_f)$, where p_f is outside the shadow zone for p_0. will first travel under standard ray tracing along a path that will cause it to arrive at he depth d_f while traveling horizontally at point $p_1 = (x_1, y_1, z_1)$ (see Figure 3.7). The ray then propagates some horizontal distance x_h to the detector with some effective attenuation length ℓ_h. So, the modified calculation of the electric field amplitude $\varepsilon_{shadow}(f)$ is

$$\varepsilon_{shadow} = \frac{\varepsilon_{1m}}{r_{total}/m} \exp\left[-\left(\frac{r^{(p_0 \to p_1)}}{\bar{\ell}} + \frac{x_h}{\ell_h}\right)\right] \tag{3.16}$$

[1]The shadow zone is discussed in more detail in Section 3.2.3

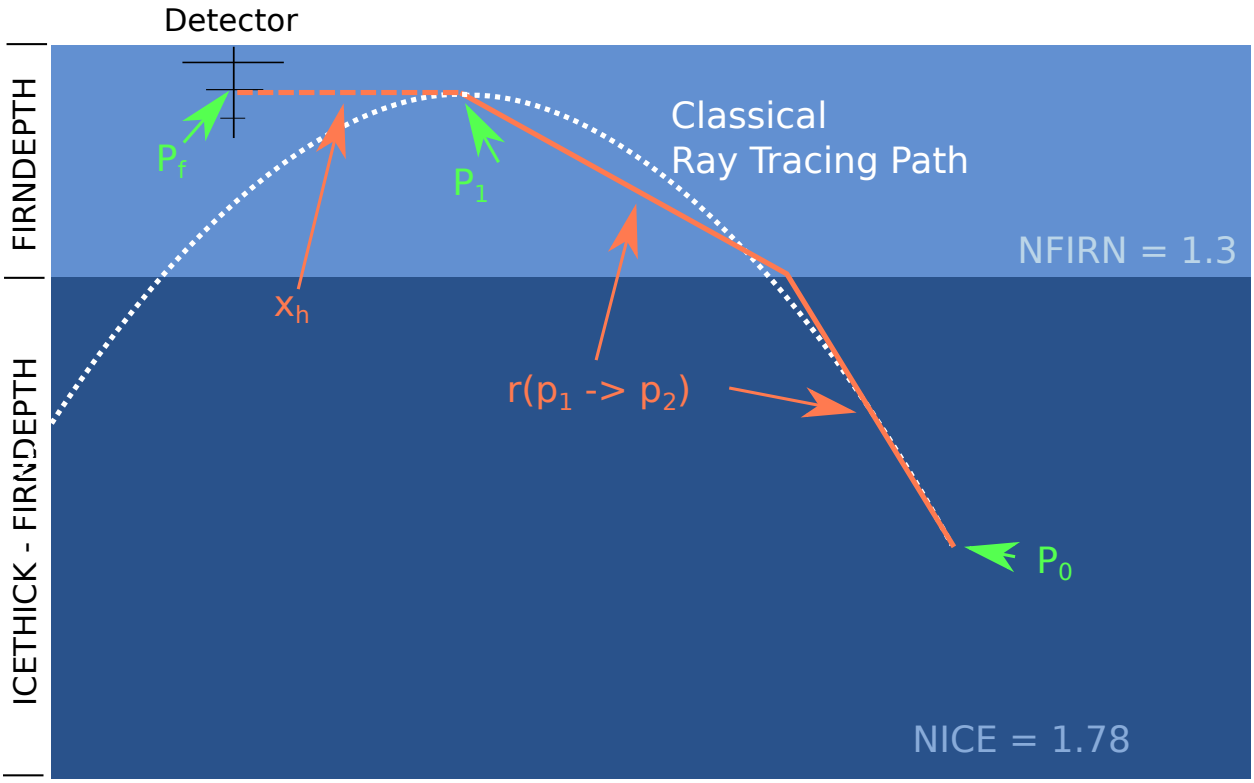

Figure 3.7: Illustration of the horizontal propagation model in *ShelfMC*. A ray propagates normally to the point where it would reach the depth of the detector with classical ray tracing, and then propagates horizontally. Also see Section 3.2.2 for details on *ShelfMC*'s ray tracing approximation.

where ε_{1m} is the electric field amplitude calculated at 1 m (see Equation 3.10), $\bar{\ell}$ is the depth averaged attenuation length, $r^{(p_0 \rightarrow p_1)}$ is the path length of the ray from p_0 to p_1, and r_{tot} is the total path length of the ray, including the horizontal portion.

3.3 Statistical Weight of Neutrino Events

The uniformly distributed arrival directions generated for interaction vertices in the fiducial volume of *ShelfMC* must be corrected by a weight factor w_i in order to account for the

absorption of neutrinos by the Earth. This absorption is approximated as:

$$w_i = \frac{\rho(z)}{\rho_{ice}} \exp\left[-\left(\frac{r_{ice}}{L_{ice}} + \frac{r_{crust}}{L_c rust}\right)\right] \tag{3.17}$$

where r_{ice} and r_{crust} are the path length of the neutrino through ice and crust on route to the detector, and L_{ice} and L_{crust} are the interaction length of the neutrino in ice and crust respectively. The factor of $\rho(z)/\rho_{ice}$ accounts for the local density of the ice. Further details of the calculation can be found in [49].

3.4 Signal Generation

ShelfMC uses a parametrization of the neutrino induced Askaryan pulse developed in [55], and validated against results from the ZHS Monte Carlo [56]. Generalizing to account for the local index of refraction at he event vertex, we have the expression for the on-cone electric field amplitude for $\theta_v = \theta_c$:

$$\frac{\varepsilon_c^{1m}}{\mathrm{V/m/MHz}}(E_{sh}, f) = 2.53 \times 10^{-7} \cdot \frac{E_{sh}}{\mathrm{TeV}} \cdot \frac{f}{f_0} \cdot \frac{1}{1 + (\frac{f}{f_n})^{1.44}} \tag{3.18}$$

$$f_n = f_0 \frac{\sqrt{n_{ice}^2 - 1}}{\sqrt{n(z)^2 - 1}} \tag{3.19}$$

where ε_c^{1m} is scaled to 1 m from the interaction vertex, E_{sh} is the shower energy, $n_{ice} = 1.78$

and $n(z)$ are the index of refraction of bulk ice and at the vertex depth respectively, and the constant $f_0 = 1.15\,\mathrm{GHz}$. From Equation 3.18, we can see that the ε_c^{1m} scales linearly with E_{sh}.

As the viewing angle θ_v (measured WRT the neutrino propagation direction) deviates from the cone angle θ_c, the amplitude falls off as a Gaussian, with a frequency dependent cone width σ_θ, according to:

$$\varepsilon^{1m}(E_{sh}, f, \theta_v) = \varepsilon_c^{1m}(E_{sh}, f) \cdot \frac{\sin\theta_v}{\sin\theta_c} \cdot \exp\left[-\ln 2 \cdot \left(\frac{\theta_v - \theta_c}{\sigma_\theta}\right)^2 \right] \tag{3.20}$$

σ_θ decreases with increasing frequency, such that signals measured off-cone contain significantly less high-frequency content. The cone-width also differs between hadronic and electromagnetic showers [50], with σ_θ for electromagnetic showers being reduced from shower elongation due to the Landau Pomeranchuck Migdal (LPM) effect [57]. See Figure 3.8.

For hadronic showers, the cone width σ_θ^{had} is calculated using the parametrization in [57]:

$$\frac{\sigma_\theta^{had}}{1^\circ} = \begin{cases} \frac{f_n}{f} \cdot (2.07 - 0.33\epsilon + 7.5 \times 10^{-2}\epsilon^2) & \text{for } 0 < \epsilon < 2 \\ \frac{f_n}{f} \cdot (1.744 - 1.21 \times 10^{-2}\epsilon) & \text{for } 2 \leq \epsilon < 5 \\ \frac{f_n}{f} \cdot (4.23 - 0.785\epsilon + 5.5 \times 10^{-2}\epsilon^2) & \text{for } 5 \leq \epsilon < 7 \\ \frac{f_n}{f} \cdot (0.67925 + 0.10725\epsilon) & \text{for } \epsilon \geq 7 \end{cases} \tag{3.21}$$

where we have defined $\epsilon = \log_{10} \frac{E_{sh}}{\mathrm{TeV}}$, and f_n is given by Equation 3.19, with $f_0 = 500\,\mathrm{MHz}$.

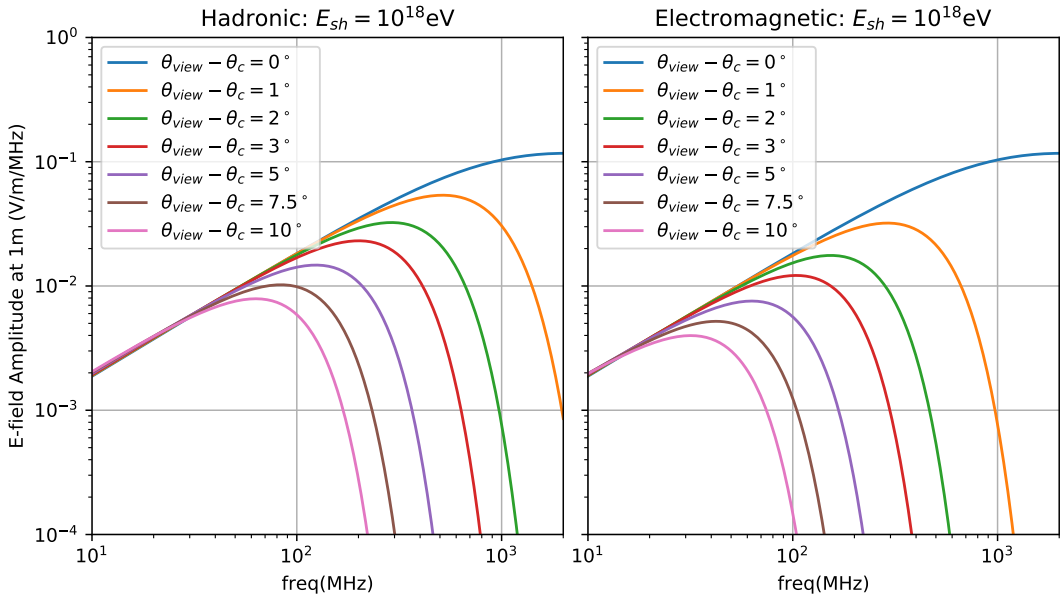

Figure 3.8: Electric field amplitude ε^{1m}, 1 m from the neutrino interaction vertex (Equation 3.20) for hadronic (left) and electromagnetic (right) showers with $E_{sh} = 10^{18}$ eV. Note that as the viewing angle shifts away from the Cherenkov cone angle, high frequency components fall off. For the EM showers, the cone width σ_θ is reduced due to the LPM effect.

For the electromagnetic shower cone width σ_θ^{em}, from [57] we have:

$$\sigma_\theta^{em} = 2.7^\circ \cdot \frac{f_n}{f} \cdot \left(\frac{E_{LPM}}{0.14 E_{sh} + E_{LPM}} \right)^{0.3} \tag{3.22}$$

Where $E_{LPM} = 2\,\text{PeV}$ is the characteristic energy at which the LPM effect becomes important, and f_n is given by Equation 3.19 with $f_0 = 500\,\text{MHz}$.

See A.1 for a Python function that performs the complete Askaryan emission calculation from *ShelfMC*

3.5 Hardware Response

3.5.1 Antenna Response

ShelfMC has the flexibility to incorporate a variety of antenna models through a flexible framework developed by Anna Nelles. For the LPDA response, this framework takes output from the WIPL-D antenna simulation software, extracting the complex current $\vec{I}(f,\phi,\theta) = (I_\phi\hat{\phi} + I_\theta\hat{\theta})$ and the complex impedance $Z(f,\phi,\theta)$, where f is the frequency and ϕ and θ represent the azimuth and zenith angles, respectively. The antenna is oriented such that the boresight lies along the $\theta = 0$ direction, and the tines along $\phi = 0$, e.g. the antenna lies in the x/z plane.

For the *ShelfMC* calculation, phases are neglected, and an effective length $\vec{\ell}$ is calculated according to

$$\vec{\ell}(f,\phi,\theta) = 2\lambda\frac{|Z|}{Z_0}\left(|I_\phi|\hat{\phi} + |I_\theta|\hat{\theta}\right) \tag{3.23}$$

where $\lambda = nf/c$ in the medium, and $Z_0 = 119.9169\pi\,\Omega$ is the impedance of free space.

For an incident electric field $\vec{\varepsilon}(f) = \varepsilon(f)\hat{n}_{pol}$, where $\hat{n}_{pol}$ is the E-field polarization normal vector, the induced voltage amplitude in the frequency domain $v(f)$ (which has units $[volts]/[frequency]$) and the effective length are related through the expression

$$v(f) = \frac{1}{2}\varepsilon\hat{n}_{pol}\cdot\vec{\ell} \tag{3.24}$$

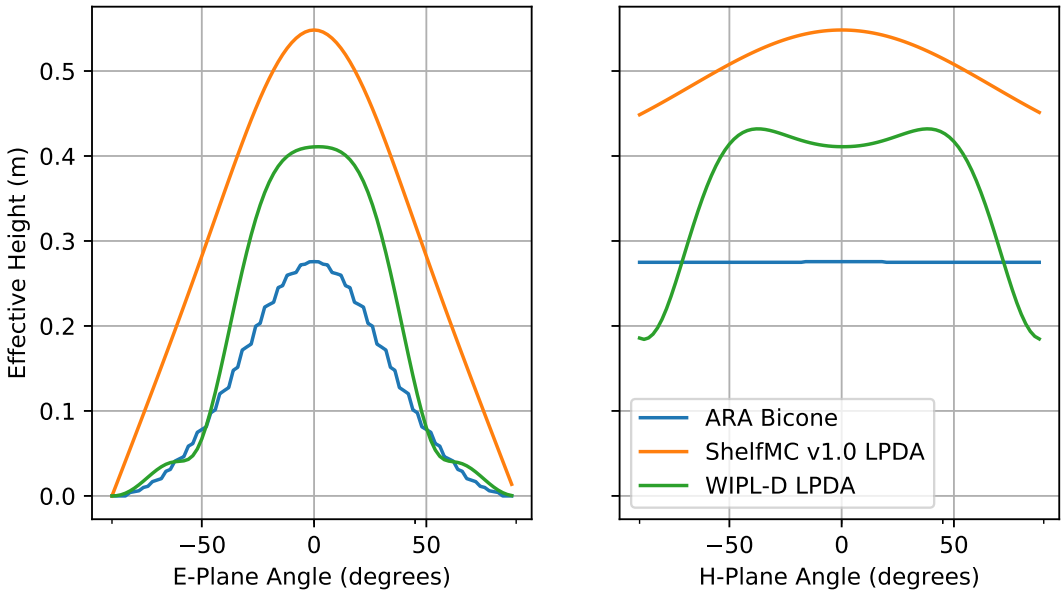

Figure 3.9: Effective height vs arrival angle for various antenna models, as calculated by *ShelfMC* at $f = 300\,\text{mHz}$

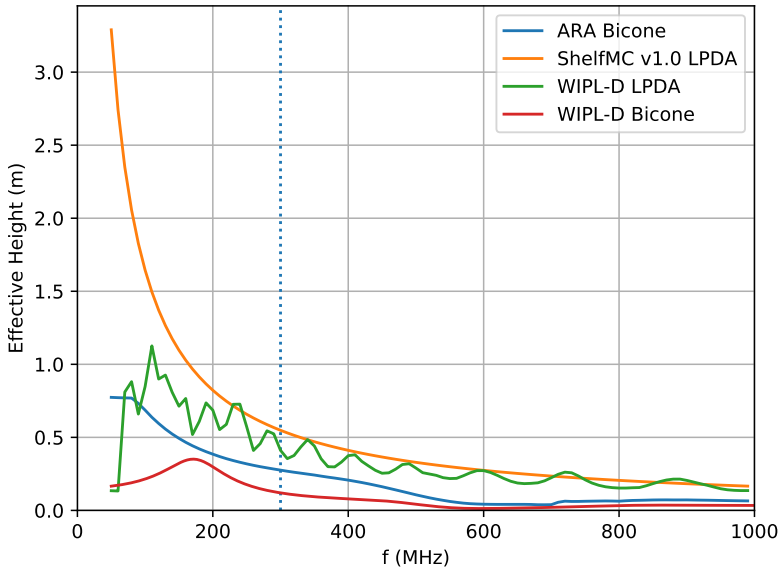

Figure 3.10: Effective height vs frequency for various antenna models, as calculated by *ShelfMC*. The vertical line marks 300 MHz which was chosen for the angular dependence shown in Figure 3.9. Note, there is disagreement between the WILP-D model of the ARA bicone antenna (red line) and the model which is currently implemented in ShelfMC (blue line). This likely introduces significant systematic uncertainty in V_{eff} for stations which employ bicones.

Figure 3.11: Photo of the ARA bicone antenna which is modeled in *ShelfMC*. Photo from [22].

where the 1/2 factor is due to the matched impedance of the DAq.

In *ShelfMC*, $\varepsilon(f)$ and $Heff(f) = \hat{n}_{pol} \cdot \vec{\ell}$ are calculated as arrays $Heff_i$ and ε_i at discrete frequencies over the bandwidth, such that the final signal amplitude at the detector V_{tot} is calculated according to:

$$V_{tot} = \frac{1}{2} \sum_{i=1}^{n} [Heff_i \varepsilon_i] \times \delta f \tag{3.25}$$

where δf is the frequency bin width.

This more nuanced approach can be compared to the LPDA parametrization which was used in *ShelfMC* v1.0 [49], which modeled the effective height as a Gaussian profile centered on the boresight (see Figure 3.9).

This work uses a model of the wire-frame bicone antenna which was borrowed from the ARA collaboration [22]. A detailed simulation of this antenna model was carried out in WIPL-D, but is not yet incorporated into ShelfMC. This result shows disagreement among the models, particularly at low frequencies (see Figure 3.10). This issue will be resolved in upcoming revisions of ShelfMC, but for now it represents a significant systematic uncertainty, likely overestimating the sensitivity of the dipole antennas.

3.5.2 Thermal Noise and Triggering

The trigger threshold in *ShelfMC* is set relative to the thermal noise V_{RMS} calculated according to

$$V_{RMS}^{noise} = \sqrt{PR} = \sqrt{k_B B T_{eff} R} \tag{3.26}$$

taking the bandwidth $B = 1000 - 50\,\mathrm{MHz} = 950\,\mathrm{MHz}$, $R = 50\,\Omega$, and $T_{eff} = 350\,\mathrm{k}$, which yields $\sigma = V_{RMS}^{noise} = 15.15\,\mu\mathrm{V}$.

The trigger condition for a single channel is that the voltage V_{tot} calculated in Equation 3.25 satisfy $V_{tot} \geq N_{thresh} \times \sigma$, where N_{thresh} is the programmed threshold value. Additionally, an n-fold majority logic can be imposed requiring that a fixed number of antennas or greater are triggered in order to save the triggered event.

3.6 Flavor Effects

3.6.1 LPM Effect on ν_e Induced Showers

As discussed in Section 3.4, the elongation of electromagnetic showers leads to a reduced cone width σ_θ at high energies. This is not a major factor for ν_τ and ν_μ induced showers, since the energy in the secondary lepton does not induce an EM shower near the interaction vertex. However, for charged current ν_e interactions, the electron produces an EM shower which co-develops alongside the hadronic shower.

In *ShelfMC*, the electromagnetic shower will have energy $E_{sh}^{em} = (1-y)E_\nu$, while the hadronic

shower will have $E_{sh}^{had} = yE_\nu$ (See Table 3.2 and Figure 3.1). These two showers are treated independently, and their signals are added according to Equation 3.20:

$$\begin{aligned}\varepsilon_{total}^{1m}(E_{sh}^{had}, E_{sh}^{em}, f, \theta_v) = \varepsilon_c^{1m}(E_{sh}^{had}, f) \cdot \frac{\sin\theta_v}{\sin\theta_c} \cdot \exp\left[-\ln 2 \cdot \left(\frac{\theta_v - \theta_c}{\sigma_\theta^{had}}\right)^2 \right] \\ + \varepsilon_c^{1m}(E_{sh}^{em}, f) \cdot \frac{\sin\theta_v}{\sin\theta_c} \cdot \exp\left[-\ln 2 \cdot \left(\frac{\theta_v - \theta_c}{\sigma_\theta^{em}}\right)^2 \right]\end{aligned} \tag{3.27}$$

where σ_θ^{had} and σ_θ^{em} are given in Equations 3.21 and 3.22.

Since E_{sh}^{had} does not depend on flavor for any given neutrino interaction with inelasticity y, the addition of the EM shower from the CC ν_e can only increase the electric field amplitude. This has the effect of increasing the effective volume of the detector for ν_e. However, the reduction in σ_θ^{em} for increased energies restricts viewing angles for which an Askaryan pulse will trigger a detector. Therefore, the ν_e advantage is greatest at low energies (See Figure 3.12).

For energies where σ_θ^{had} and σ_θ^{had} differ significantly, it may be possible to distinguish ν_e showers through frequency spectrum measurements at various viewing angles.

3.6.2 Tau Double-bang

ν_τ which undergo CC interactions in the ice produce a secondary τ lepton which will decay with a characteristic decay length given by

$$\lambda_\tau(E_\tau) = \begin{cases} 50\,\mathrm{m} \times \frac{E_\tau}{\mathrm{PeV}} & for \quad E_\tau < 10^{18}\,\mathrm{eV} \\ 50\,\mathrm{m} \times 10^3 & for \quad E_\tau \geq 10^{18}\,\mathrm{eV} \end{cases} \tag{3.28}$$

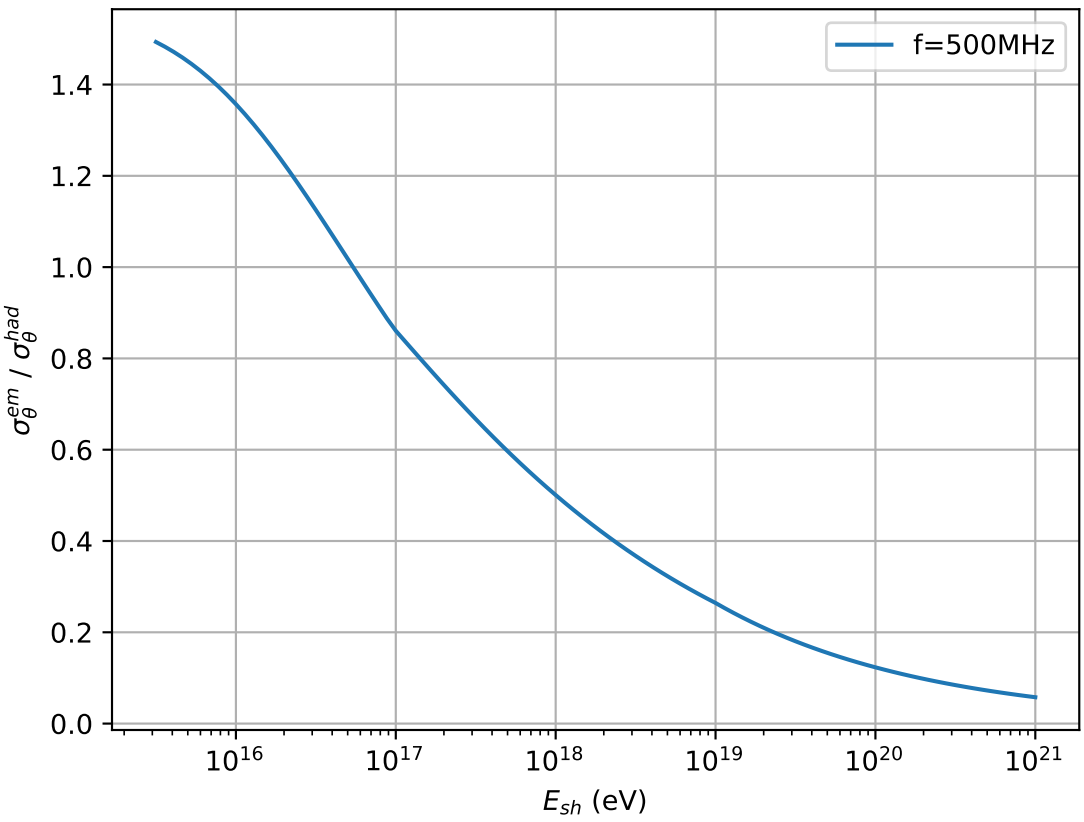

Figure 3.12: Ratio of $\sigma_\theta^{had}/\sigma_\theta^{em}$ vs E_{sh} (Equations 3.21 and 3.22). For $E_{sh} > 10^{18}\,\text{eV}$, cone width for electromagnetic showers is reduced by over a factor of 2. Note: while this calculation was done at $f = 500\,\text{MHz}$, these ratios hold regardless of frequency.

Condition		E_{sh}	Interpretation
$\theta_\nu \geq \pi/2$	$\lambda_\tau < L_{ice}$	$\max(y,(y-1))E_\nu$	Downward going, τ double-bang in ice
	$\lambda_\tau \geq L_{ice}$	yE_ν	Downward going, τ double-bang below ice
$\theta_\nu < \pi/2$		$\max(y,(y-1))E_\nu$	Upward going, τ double-bang in ice

Table 3.3: Shower energy algorithm for CC ν_τ interactions. θ_ν is the arrival zenith for the neutrino, and fixfixfix$L_{ice} = z/\cos(\theta_\nu)$ is the path-length in ice where the τ can decay where z is measured up from the ice/sea water interface. λ_τ is calculated according to Equation 3.28.

Note that for τ lepton in the EHE regime, decay losses are dominated by photonuclear effects, which are not well constrained [58]. Therefore, we cap λ_τ at $E_\tau = 10^{18}\,\text{eV}$ in *ShelfMC* as a conservative approximation.

ShelfMC does not currently track separate ν_τ and τ vertices for each event. Instead we consider the possibility that a particular shower could *either* be from the primary ν_τ interaction with $E_{sh} = yE_\nu$ or the subsequent decay of the resulting τ lepton with $E_{sh} = (1-y)E_\nu$, according to Table 3.2. If the τ decay happens in the ice then the larger of the two showers will be considered; otherwise the τ shower will be ignored. This is summarized in Table 3.3.

For an upward going τ lepton decaying in the ice, there is a possibility that the primary ν_τ interaction would have taken place outside the fiducial volume. In essence, the fiducial volume for these events is essentially greater with respect to the calculation of the effective volume (see Equation 3.30). We account for this by scaling the weight factor w of upward going CC ν_τ events according to:

$$w_{adjusted} = w \times (\lambda_\tau \cos(\theta\nu) + d)/ICETHICK \quad \text{if} \quad \lambda_\tau \cos(\theta\nu) + d) > ICETHICK \quad (3.29)$$

where d is the depth of the τ decay vertex, and $ICETHICK$ is the total depth of the ice shelf. For a visualization of Equation 3.29 see Figure 3.13.

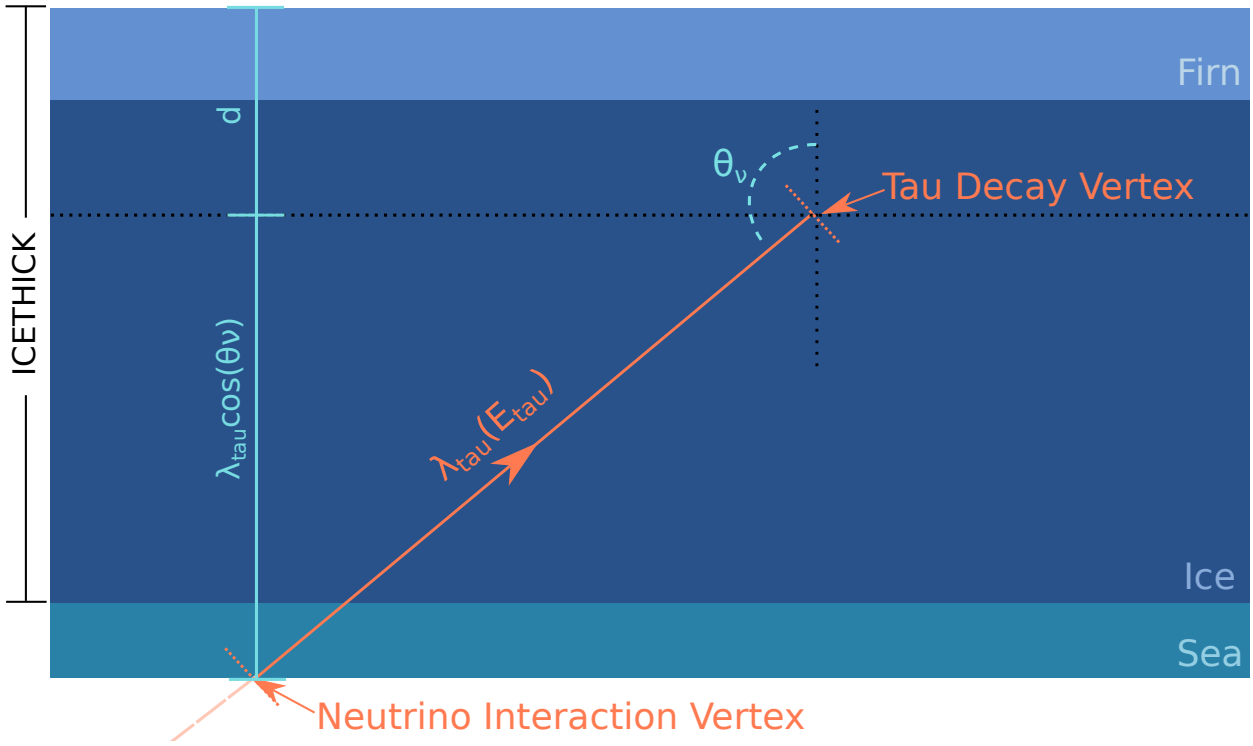

Figure 3.13: Graphical representation of the weight adjustment in Equation 3.29. Scaling the weight effectively increases the fiducial volume to include the sea between the primary neutrino interaction vertex and the bottom of the ice shelf.

3.6.3 Tau Regeneration

Uniquely, ν_τ can undergo a process by which they may pass through the Earth's crust at energies at which the Earth is no longer transparent to the other flavors [59]. In this mechanism, τ leptons produced in the initial ν_τ induced shower quickly decay before loosing significant energy, producing a ν_τ with reduced energy in the process. The net result is an increased appearance of upward going ν_τ with $E'_\nu < E_\nu$. Neutrinos within ARIANNA's detectable energy range are still above the threshold where τ regeneration renders the Earth transparent, so this effect is most prominent for lower energy neutrinos with arrival zeniths near the horizon.

Since the energy of the neutrino that interacts near the detector (E'_ν) is reduced from the energy of the original neutrino incident on the Earth (E_ν), the proportional increase in the abundance of neutrinos at the detector with energy E'_ν depends on the relative isotropic fluxes $\Phi(E_\nu)/\Phi(E'_\nu)$ for all $E_\nu > E'_\nu$. Thus, the increase in the calculated effective volume at E'_ν is model dependent on the UHE neutrino flux.

ShelfMC accounts for the τ regeneration effect by multiplying the neutrinos statistical weight by a proportionality factor which is a function of detected neutrino energy and arrival zenith, using the dedicated simulation in [59]. The results of this calculation are tabulated and presented in [49].

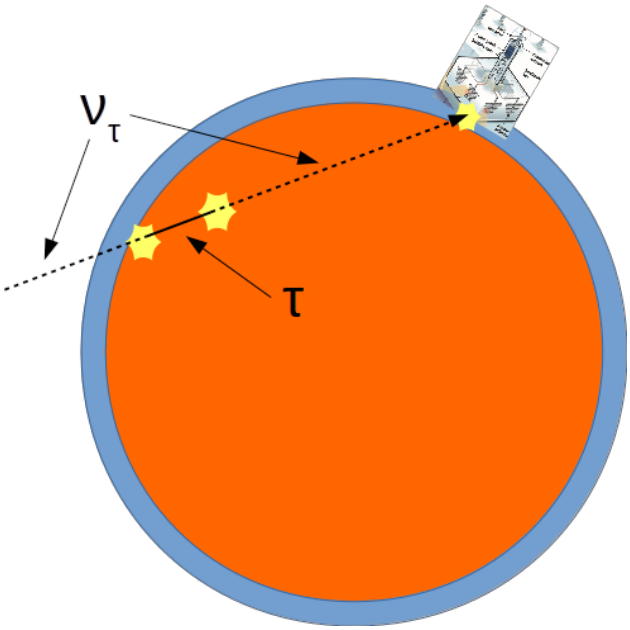

Figure 3.14: Graphical representation of the τ regeneration effect. The τ lepton produced in the initial CC neutrino interaction decays before loosing significant energy, producing a ν_τ at reduced energy, and hence, longer interaction length.

3.7 Effective Volume Calculation

The total effective volume integrated over sold angle, $V_{eff}\Omega$, is a standard measure of the overall aperture of a neutrino detector, and is defined in Eqation 3.30.

$$V_{eff}\Omega = V_{fid} \cdot \frac{\rho_{ice}}{\rho_{water}} \cdot 4\pi \cdot \frac{1}{n} \cdot \sum_{i=1}^{n_{trig}} w_i \tag{3.30}$$

Where V_{fid} is the fiducial volume in which neutrino vertices are generated, n is the total number of simulated neutrinos, n_{trig} is the number of successful triggers, and w_i is the statistical weight factor for each triggered event.

A directionally resolved effective volume $V_{eff}(\phi, \theta)$ can also be defined with the normalization

condition:

$$\oiint V_{eff}(\phi,\theta)d\Omega = \int_0^{2\pi}\int_{-1}^{1} V_{eff}(\phi,\theta)d\cos\theta d\phi = V_{eff}\Omega \tag{3.31}$$

To extract this quantity from the results of a Monte Carlo, neutrino arrival directions should be histogrammed into equal area bins in ϕ and $\cos\theta$ with bin widths $\Delta\cos\theta$ and $\Delta\phi$. Let w_{jk} be the weighted number of triggered events in the bin centered at θ and ϕ, and w_{tot} be the total weighted number of triggered events, such that:

$$V_{eff}(\phi,\theta) = \frac{w_{jk}}{w_{tot}}\frac{V_{eff}\Omega}{\Delta\cos\theta\Delta\phi} \tag{3.32}$$

Chapter 4

Results from Monte Carlo

4.1 Simulation of Current ARIANNA Stations

4.1.1 Effective Volume for HRA Stations

The calculation of the total effective volume (Equation 3.30) for a single HRA station was performed by running many instances of *ShelfMC* in parallel. Each instance generates a pre-determined number of neutrino vertices at pre-defined energies. Here we have chosen to calculate V_{eff} at half decade intervals from $10^{15.5} - 10^{21}$ eV. The number of events generated at each particular energy is chosen such that the expected number of triggered events at each energy is 3000. As we will see, the effective volume decreases rapidly at low energies, so computing time is dominated by the low energy calculation. The number of simulated events n required to yield n_{trig} triggered events at energy E is parametrized as:

$$n = n_{trig} \times 10^{x} \quad with \quad x = 1.2 + 22637.8178 \times 10^{-0.2438544 \log_{10} E} \tag{4.1}$$

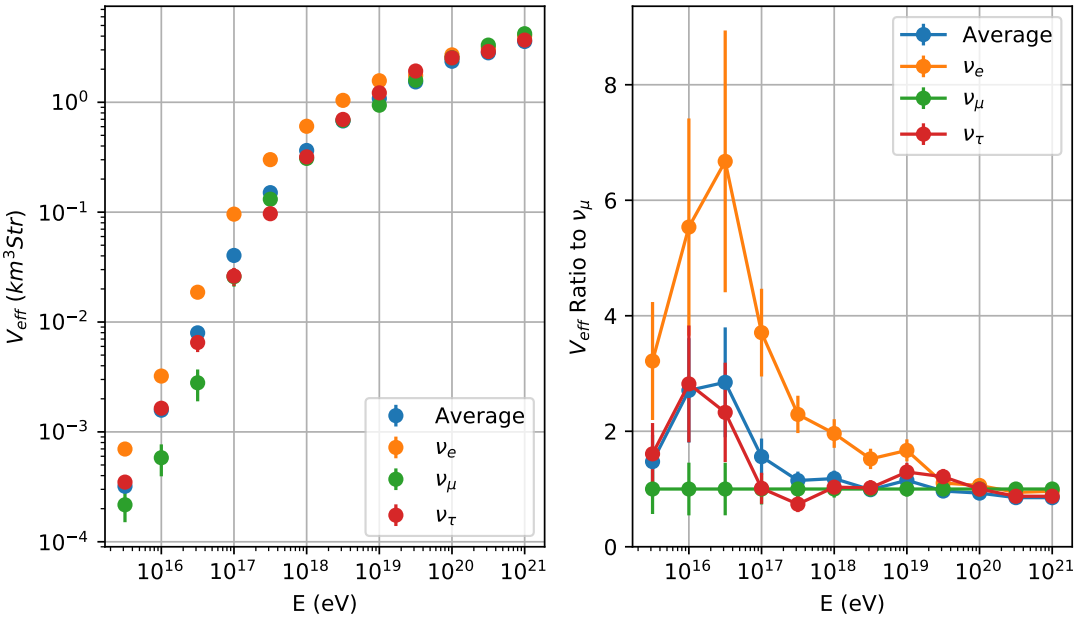

Figure 4.1: (left) Effective Volume for a single HRA station, simulated according to the simulation parameters in 4.1. (right) Ratio of single-flavor V_{eff} to the ν_μ effective volume. Flavor effects which enhance the ν_e and ν_τ effective volumes are discussed in detail in the text of Section 4.1.1. Possible explanations for the relatively weak enhancements of these flavor effects below $10^{16.5}$ eV are discussed in the text.

Individual flavor, as well as the flavor averaged effective volume are shown in Figure 4.1. We see the impact of the flavor effects discussed in Section 3.6 at play in the ν_e and nu_τ effective volumes.

ν_e dominates at low energy since the prompt EM shower produced by the secondary electron in the CC interaction increase the median shower energy by a factor of 10. However, elongation of the EM shower at higher energies due to the LPM effect restricts the geometries where the EM shower can trigger a station, so the benefit is negligible above $E \approx 10^{18}$ eV (Section 3.6.1).

ν_τ also sees an enhancement at lower energies due to the tau regeneration and double bang effects (Sections 3.6.3 and 3.6.2). In particular, the enhancement from tau regeneration for a GZK flux is significant below 10^{17} eV (see Figure 4.7).

Parameter	Setting
Spectrum	GZK
Energy Range	$10^{15.5} - 10^{21.5} eV$
Ice Thickness	$575m$
C (see Eqn. 3.3)	$34.48m$
Firn Depth	$68.96m$
Depth Averaged Attenuation Length	$500m$
Noise Temperature	$350°C$
Bandwidth	$50 - 1000MHz$
Noise Before Trigger	Disabled
Reflection Coefficient	0.9
Trigger Threshold	4σ
Majority Logic	2 of 4
Tau Regeneration	Enabled
Shadowing	Enabled

Table 4.1: *ShelfMC* simulation parameters for the currently deployed ARIANNA stations. The effective noise temperature is based on the amplifier measurements presented in Table 2.2.

Results in Figure 4.1 seem to indicate that the enhancement from these effects peaks near $10^{16.5}$ eV, but the naive expectation would be that the relative effect should continue to increase at lower energies. This is not yet well understood, and merits further study. Possible explanations include the widening of the EM cone width at low energies (Figure 3.12). It is also possible that for the lowest energies, significant numbers of events are within a radius where the separation of the antennas becomes important, and the Askaryan signal should no longer be modeled as a plane wave.

4.1.2 Details of the Simulated Neutrino Signal

From the position of the neutrino vertices (Fig. 4.2), the effect of shadowing can be seen as a hard boundary. Notice, that for direct events, a majority of triggered event vertices lie near the shadow boundary. Since the Chenrenkov angle for ice $\theta_c \approx 56°$ is slightly greater than the critical angle associated with the shadow zone $\theta_{crit} = arcsin(N_{firn}/N_{ice}) \approx 47°$, the on-cone emission for horizontally propagating neutrinos will be directed towards the station

Neutrino Energy (eV)	Effective Volume ($km^3 Str$)
$10^{15.5}$	7.252×10^{-4}
10^{16}	4.180×10^{-3}
$10^{16.5}$	1.680×10^{-2}
10^{17}	4.918×10^{-2}
$10^{17.5}$	1.597×10^{-1}
10^{18}	3.981×10^{-1}
$10^{18.5}$	6.929×10^{-1}
10^{19}	1.104
$10^{19.5}$	1.625
10^{20}	2.166
$10^{20.5}$	2.783
10^{21}	3.329

Table 4.2: All flavor effective volume for a single ARIANNA HRA station, using the simulation parameters in Table 4.1.

when the interaction vertex is inside the shadow zone.

Besides ray optics, the main physics consideration which constrains the relatively narrow cone width, σ_θ, about the Cherenkov cone angle (see Section 3.4). The viewing angle must fall within a narrow range in order for a sufficiently strong signal to be incident on the detector, imposing a particular geometrical alignment to trigger the station. The distribution of viewing angles for triggered events is shown in Figure 4.3.

Since the ice/seawater interface at Moore's Bay acts as a reflector for radio waves, the ARIANNA stations at Moore's Bay are sensitive to (initially) downward propagating radio signals from downward going neutrinos. This effectively spreads the detector's aperture across the whole upward sky. Signals which reach the detector without reflecting , however, restrict neutrino arrival directions to zenith angles near the horizon (Fig. 4.4).

For the reflected events, the signal arrival directions at the detector has mode near 45° below the horizon. However, for direct events, the signal arrival direction is concentrated closer towards the horizontal (Fig. 4.5).

The distribution of signal polarization also varies depending on whether the signal is direct

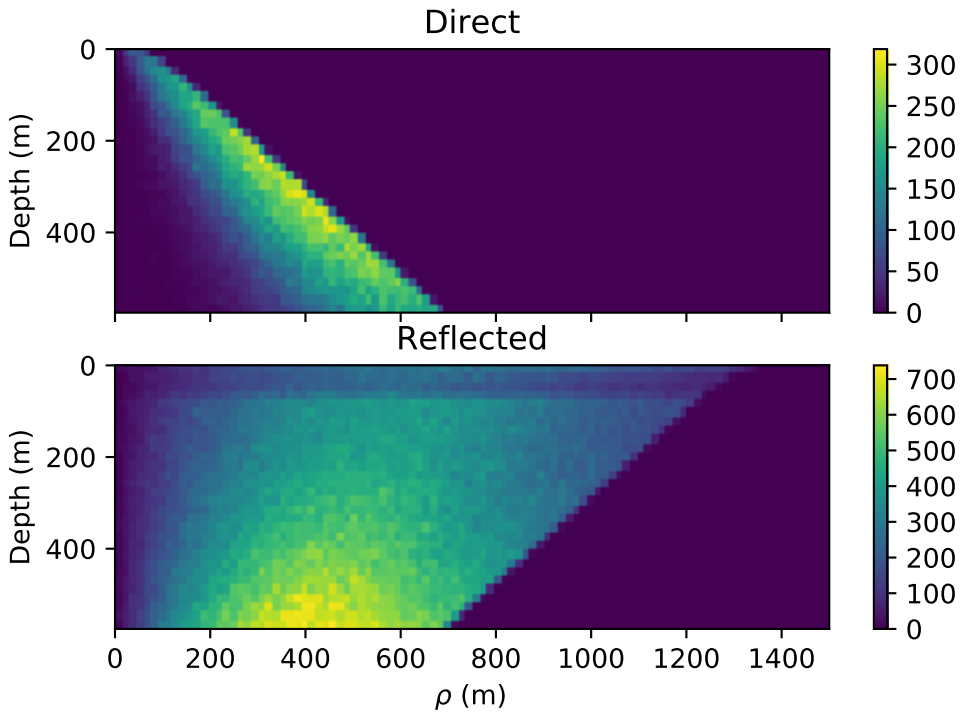

Figure 4.2: Neutrino vertex location for simulated neutrino events. Standard ARIANNA station located at the origin. See Table 4.1 for simulation parameters. Note that color scales vary between the direct and reflected events plots.

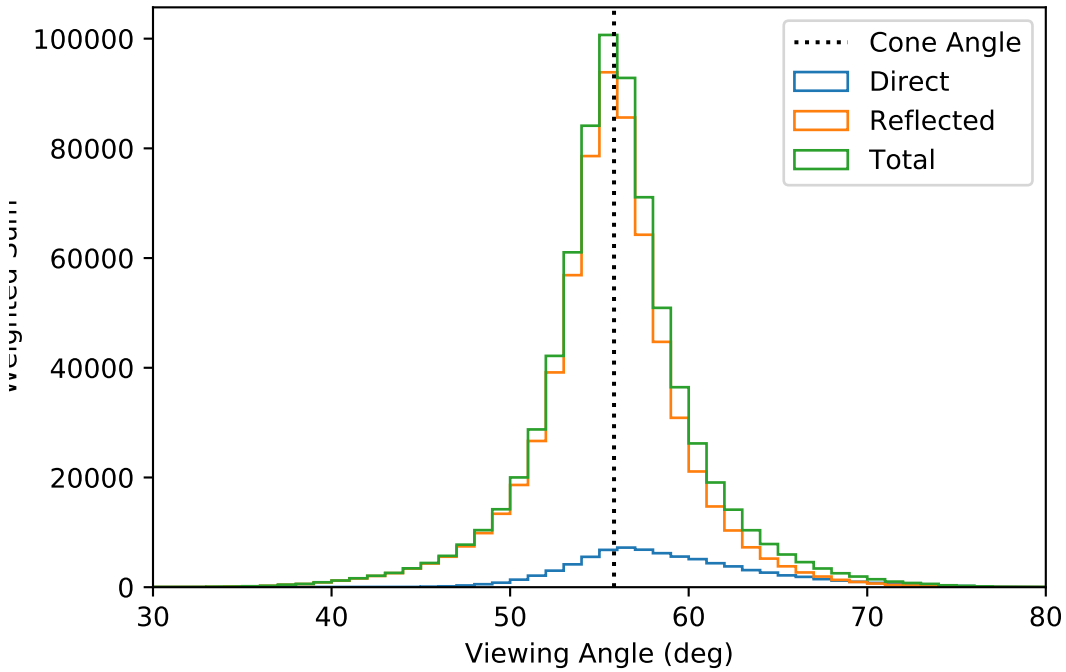

Figure 4.3: Viewing angle of the neutrino signal, measured with respect to the neutrino propagation direction. See Table 4.1 for simulation parameters.

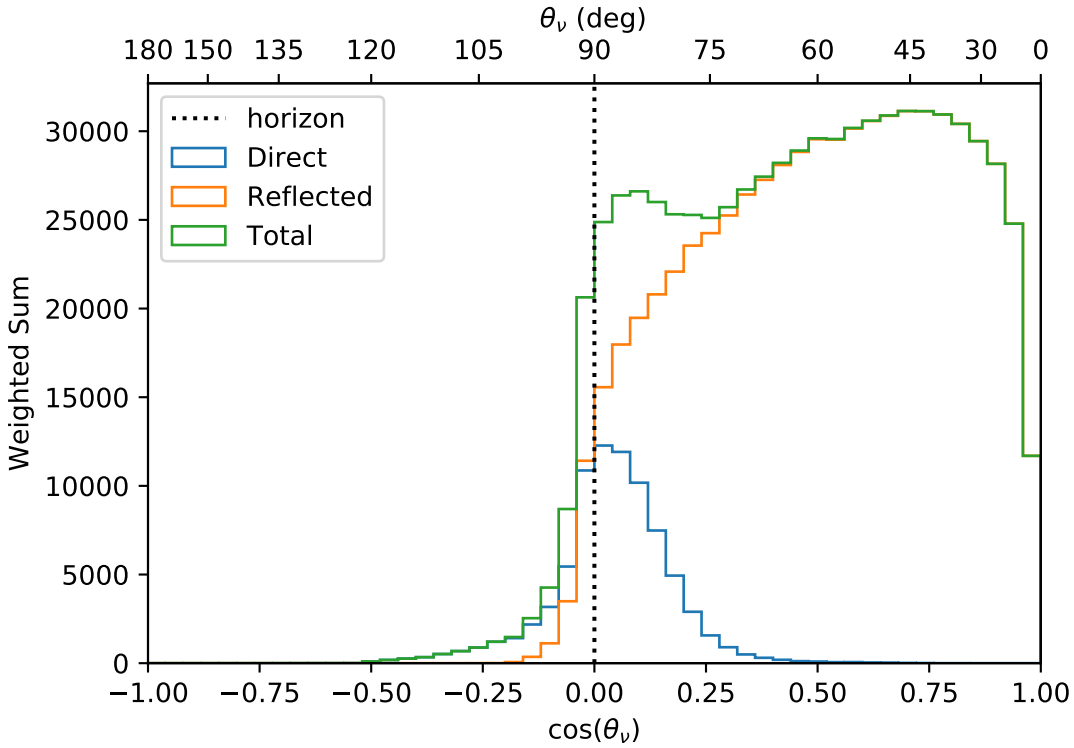

Figure 4.4: Neutrino arrival zenith, with with 0° representing a downward going neutrino. See Table 4.1 for simulation parameters.

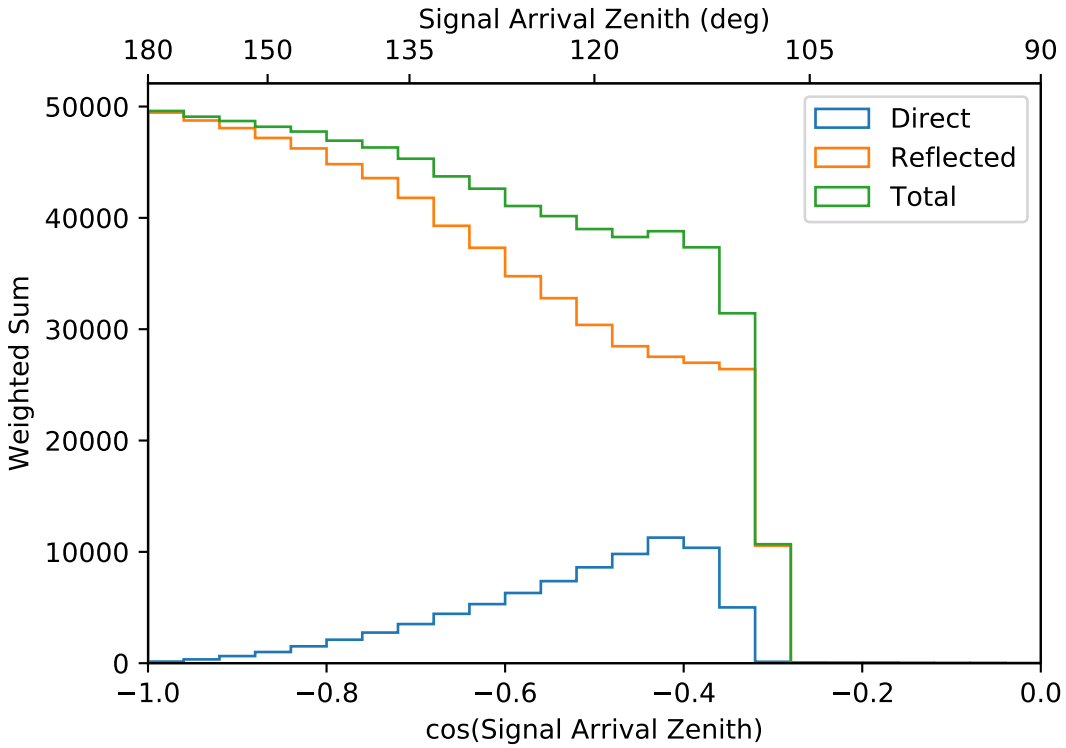

Figure 4.5: Arrival zenith of neutrino signal at the station, with 180° representing an upward going signal. See Table 4.1 for simulation parameters.

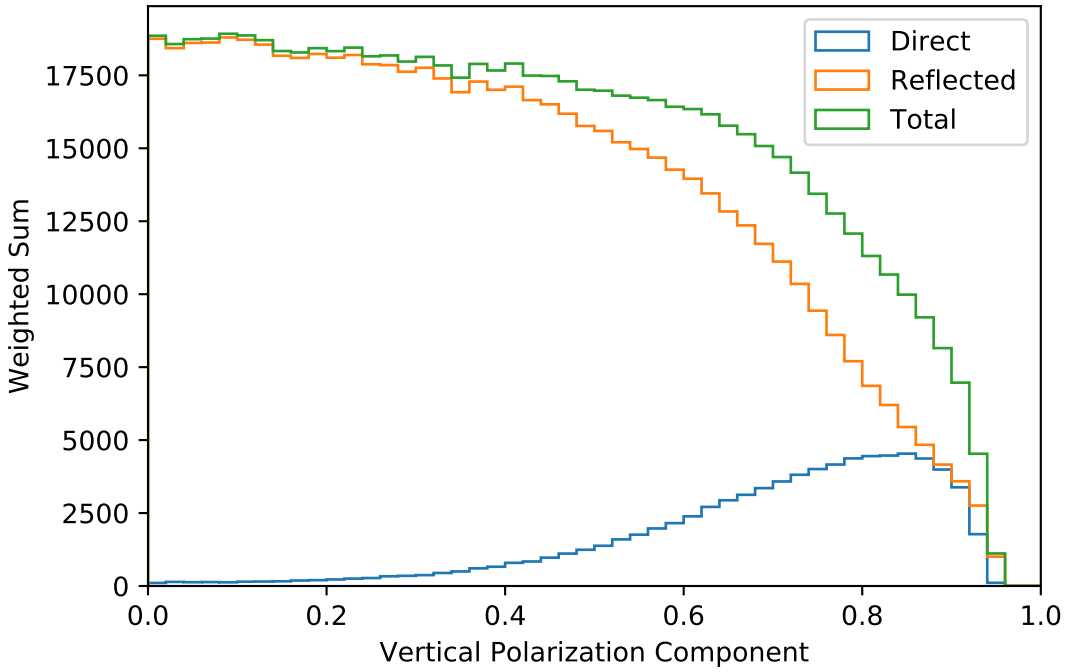

Figure 4.6: Vertical component of the neutrino signal polarization ($|cos\theta_{pol}|$). See Table 4.1 for simulation parameters.

or reflected (Fig. 4.6). Reflected signals are have a larger horizontal polarization component, which is suitable for the downward facing LPDA antennas of the HCR stations.

These qualitative differences between the direct and reflected signals are an important consideration for a potential ARIANNA station at South Pole (Sections 4.2.3 and 4.2.4), since a detector with exclusively downward facing LPDA's is not optimized for the direct signal.

4.2 Systematic effects on Effective Volume

4.2.1 Tau Regeneration

The Tau regeneration effect (Section 3.6.3) effectively boosts the ν_τ effective volume close to the horizon. Since the scale of this effect is model dependent on the UHE neutrino flux, we have simulated the Tau regeneration effect for both ESS GZK, as well as an E^{-2} spectra. See Figure 4.7.

4.2.2 Horizontal Propagation Model

As discussed in Section 3.2.5, a model was incorporated into *ShelfMC* to estimate the effect of radio signal which may propagate to the detector from classically forbidden regions. The impact of this effect is shown in Figure 4.8. Such horizontal propagation has been observed [54], but the impact on neutrino signal is not yet well understood, and there will likely be difficulty in reconstructing such events. However, these simulation results motivate additional study, since the potential impact on effective volume is large, particularly at the South Pole, where much of the signal arrives at angles close to the horizon.

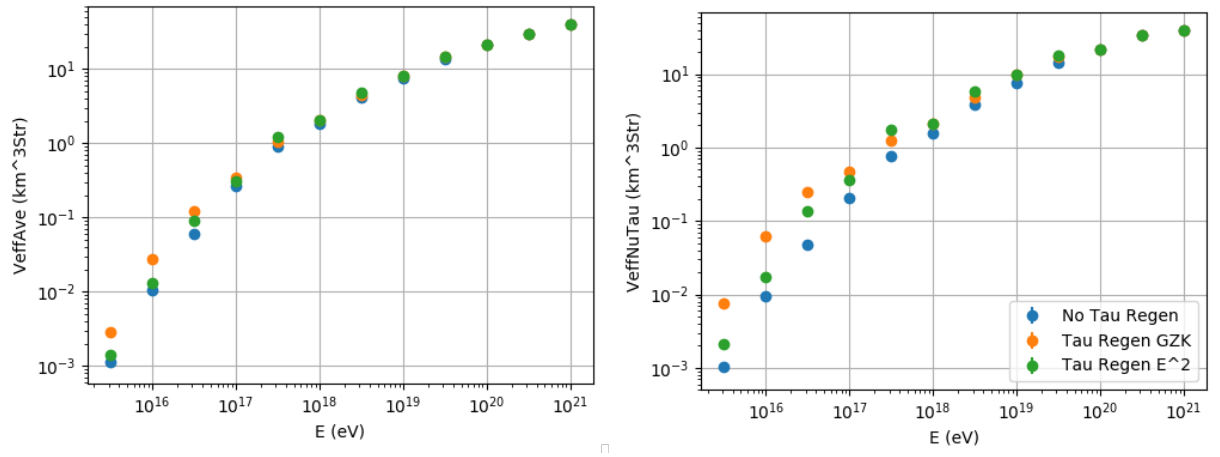

(a)

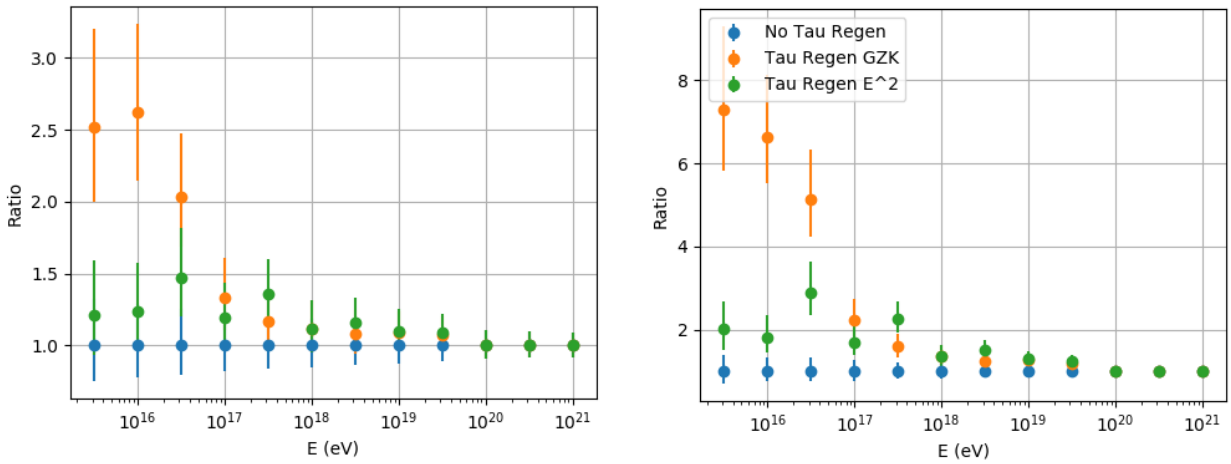

(b)

Figure 4.7: Impact of Tau Regeneration effect on flavor averaged (left), and τ only effective volume for a HRA single station. The strong enhancement below 10^{17} eV for the GZK flux is due to the abundant flux at 10^{18} eV (see Figure 1.7) cascading to lower energies. The enhancement for an E^{-2} spectrum is comparatively much weaker, such that for the even softer spectra measured by IceCube [14, 15] the effect should be negligible.

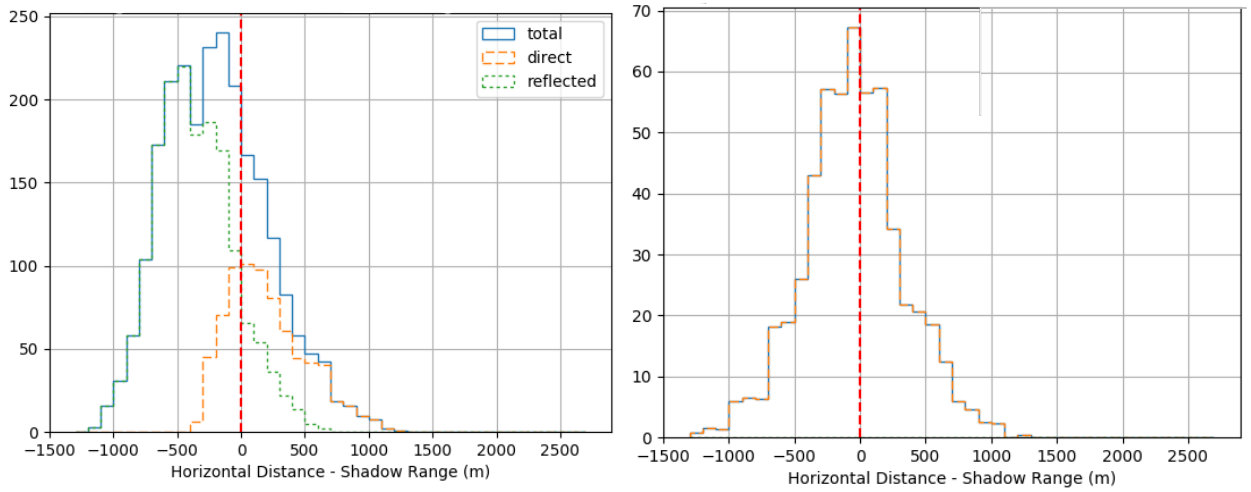

(a) (b)

Figure 4.8: Distance distribution for simulated neutrino events for Moore's Bay (a), and South Pole (b) ice for an effective horizontal attenuation length $\lambda_h = 400\,\text{m}$. Positive values represent events which originate in the "shadow zone" (see Section 3.2.5). The additional area under the curve to the right of the vertical red line represents the effective volume gained by these classically forbidden triggers.

4.2.3 Assessment of Moore's Bay Vs South Pole Ice

Since the area surrounding South Pole Station is being investigated as an alternative site for an ARIANNA style array[1], a trade analysis of the two sites is required.

The principle advantage of the South Pole ice (by virtue of the colder surface temperatures) is the longer attenuation length. The functional dependence of temperature vs depth on the East Antarctic Ice Sheet differs somewhat from the ice shelf parametrization (Equation 3.11), but to first order, we can approximate the South Pole ice by using Equation 3.11 with the modified parameters $\bar{\ell} = 1400\,\text{m}$ and $z_{max} = 2700\,\text{m}$.

Additionally, the depth of the firn at the South Pole is significantly deeper then Moore's Bay site (See Figure 3.3). The lower gradient of the index of refraction ($\partial n/\partial z$) near the surface

[1]I suppose the acronym would have to change from Ross Ice shelf ANtenna Neutrino Array if such an array was deployed on the East Antarctic Ice Sheet. Surely another suitable female name beginning in A can be found. Or, perhaps, it's time for something new.

Parameter	Setting
Spectrum	GZK
Energy Range	$10^{15.5} - 10^{21.5} eV$
Ice Thickness	$2700m$
C (see Eqn. 3.3)	$71.43m$
Firn Depth	$142.86m$
Depth Averaged Attenuation Length	$1400m$
Noise Temperature	$350°C$
Bandwidth	$50 - 1000 MHz$
Noise Before Trigger	Disabled
Reflection Coefficient	0
Trigger Threshold	4σ
Majority Logic	2 of 4
Tau Regeneration	Enabled
Shadowing	Enabled

Table 4.3: *ShelfMC* simulation parameters for the HRA station at South Pole.

leads to a wider shadow zone, opening more volume for interaction vertices to trigger the detector.

The main drawback of the South Pole ice is that, unlike for an ice shelf, there is no reflective boundary beneath the ice. The lack of these reflected events, which make up $\approx 90\%$ of the signal at Moore's Bay, restricts the triggering neutrino arrival direction to zenith angles close to the horizon. This reduces sky coverage, as well as restricting the signal arrival direction at the detector. This necessitates a re-optimization of the standard ARIANNA layout, to take best advantage of the South Pole ice properties, which will be discussed in Section 4.2.4.

4.2.4 Detector Optimization

Due to the HRA's nature as a pilot array, who's primary goal was the demonstration of the feasibility of the ARIANNA concept, there is significant space for optimization in the final detector design. *ShefMC* results show a significant fraction of signal arrival directions close to the horizon as well as vertically polarized signals, neither of which is optimal for

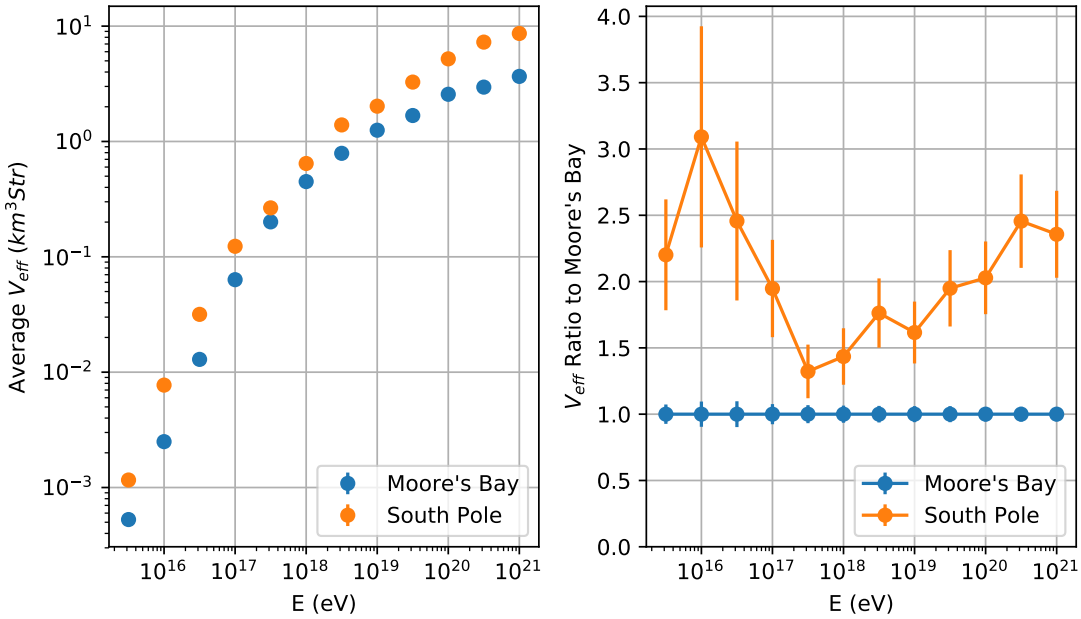

Figure 4.9: Single station V_{eff} at South Pole and Moore's Bay sites with standard ARIANNA HRA layout. Note: See Section 4.2.4 for discussion and results for alternative station layouts.

downward pointed LPDA's (see Section 4.1.2). This is even more significant at the South Pole, where the lack of reflected events concentrates the signal near the horizon. The addition of vertically oriented dipole antennas adds sensitivity to horizontally propagating, vertically polarized signals, reducing the trigger bias of the ARIANNA HRA layout. This also creates a design with can measure polarization in all three orthogonal directions, aiding in polarization reconstruction and, in turn, the directional reconstruction of the primary neutrino.

Also, buy leveraging the majority logic, thermal trigger rates can be significantly reduced by increasing the number of antennas which must trigger in coincidence. A proposed layout with 8 downward LPDA's, and 4 vertically oriented dipoles would allow for a 4 of 12 majority logic condition, allowing for a threshold reduction to $\approx 3\sigma$ while maintaining trigger rates of $< 10^{-2}$ Hz.

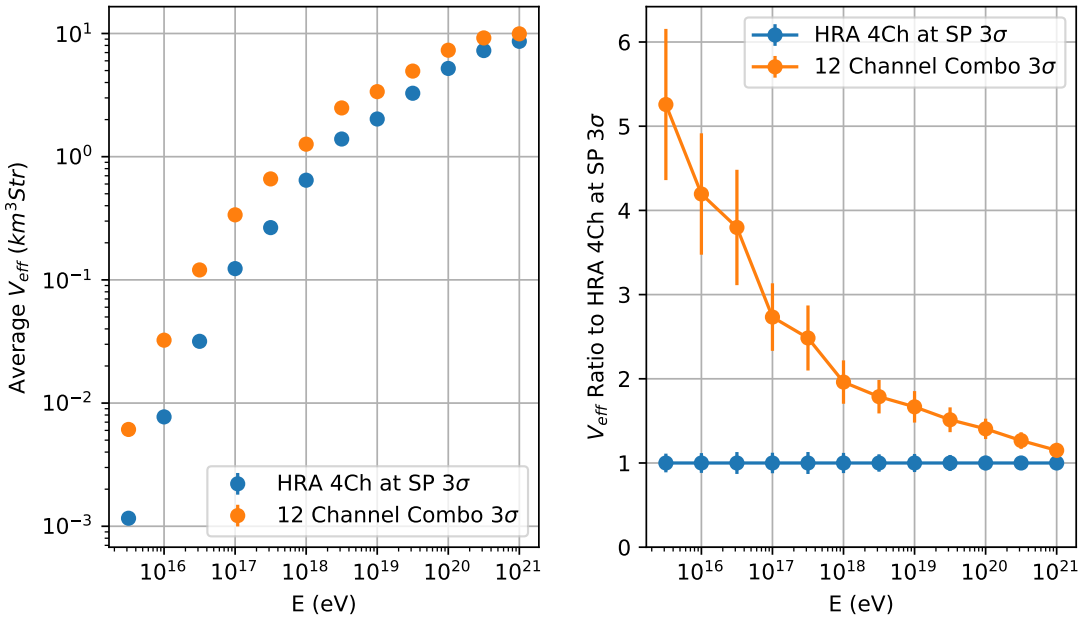

Figure 4.10: Comparison of flavor averaged V_{veff} for the standard HRA and proposed 12 channel combo station. Here, both stations are modeled with 3σ thresholds, to highlight the impact of the added antennas. Note: As mentioned in Section 3.5.1, the implementation of the bicone dipole antenna is likely optimistic at low frequencies (Figure 3.10), and may exaggerate the increase in effective volume at low energies.

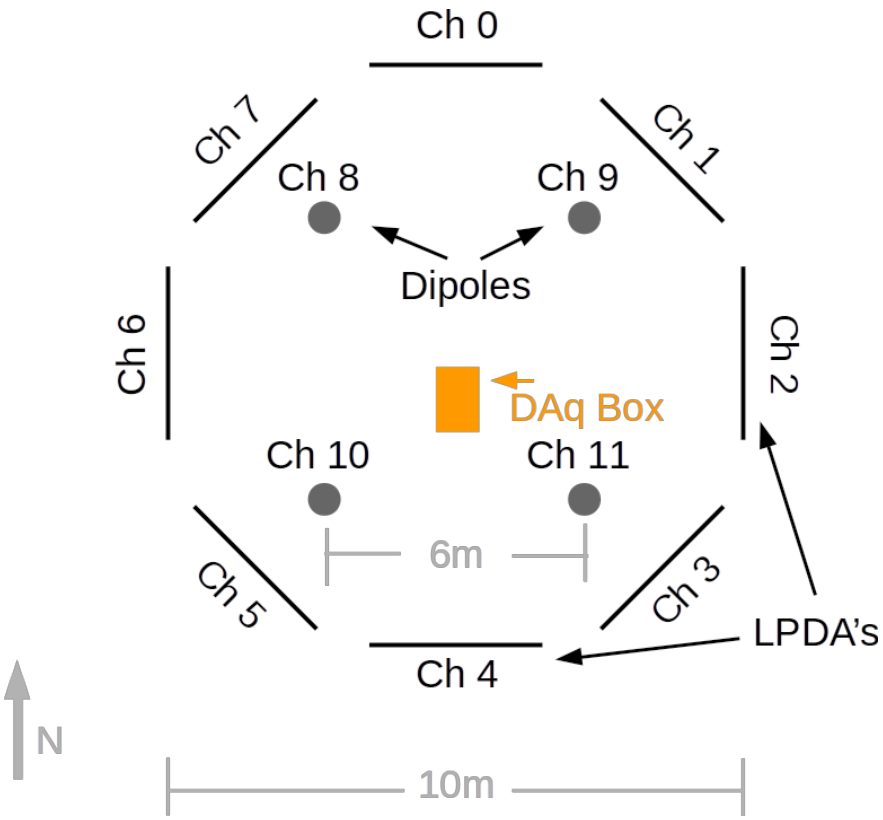

Figure 4.11: Top-down diagram of the proposed 12 channel ARIANNA combo station. Final design would also include a set of upward facing LPDA's for cosmic ray tagging, but those are not considered for the V_{eff} calculations.

Chapter 5

Analysis

5.1 Generating The Neutrino Signal Space

Simulated neutrino events are produced using a multi-step process. First, a library of 1265 neutrino templates is created by convolving Askaryan pulses parametrized from ZHS Monte Carlo [60] (Figure 5.1) through the measured antenna and amplifier response, according to the procedure outlined in [23].

Secondly, neutrino triggers are generated in *ShelfMC*, which contain the amplitude, signal arrival direction and polarization, and viewing angle. This information is used to generate simulated events using the pre-calculated neutrino templates.

The simulated neutrino signals which pass the 4σ threshold over thermal noise (the effective threshold of HRA stations during normal operation) are included in the simulated signal space. The analysis will be performed in the 2D parameter space defined by the maximum correlation of the data channels against a reference template (χ, Section 5.2.1) and the minimum channel amplitude ($MinLogP2P$, Section 5.2.3), which provides an intuitive method

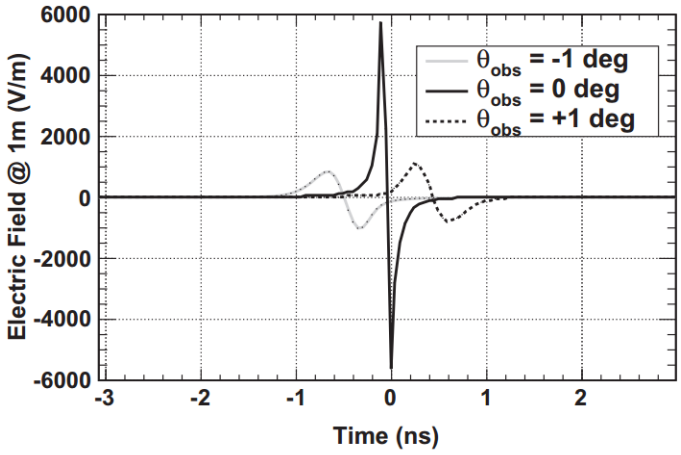

Figure 5.1: Simulated raw E-field due to a neutrino induced particle shower in ice, from [23].

for separating signal and background.

5.1.1 The Neutrino Templates

Since the HRA employs two separate amplifiers with differing responses (see Section 2.1.4), two distinct sets of templates must be generated for the neutrino signal. For this analysis, the correlation parameter χ (Section 5.2.1) is taken as the maximum cross-correlation between the waveform under test and a single reference template. Here we have chosen the template corresponding to E and H-plane angles[1] of 30° and a cone angle of 0° (viewing angle is on the Cherenkov cone).

Selecting a single template avoids the complication of dependence on directional reconstruction, while still providing a strong discriminator against background. This particular template was chosen since 30° from vertical is a region of relative abundance for the triggered signal arrival direction (see Figure 4.5). This template also correlates well with the full set of other neutrino templates (Figure 5.3), such that neutrino signals from various arrival directions should correlate well to the reference template.

[1]The E-plane angle is a rotation in the plane of the LPDA tines, while the H-plane angle is a rotation about the axis of the tines. $E = H = 0$ corresponds to the boresight.

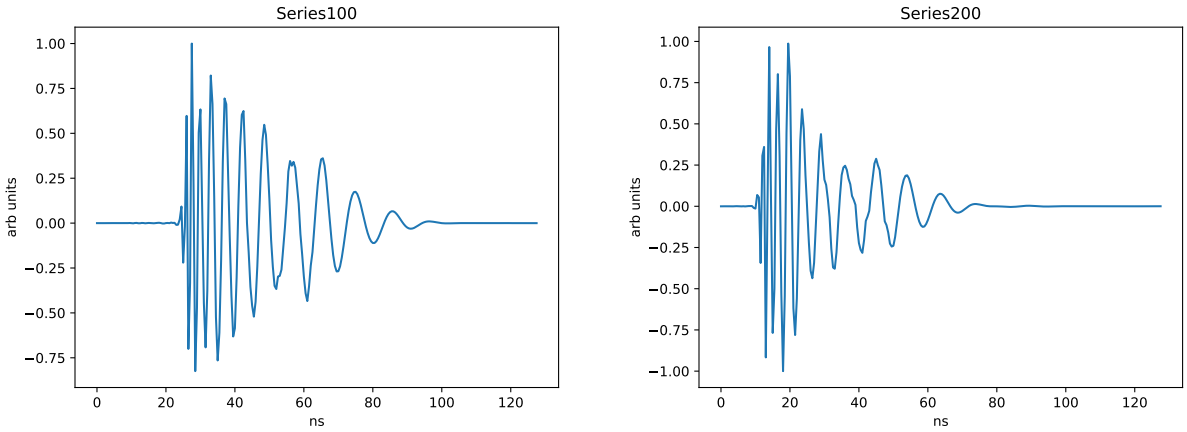

(a) (b)

Figure 5.2: Reference neutrino templates for 100 series (left) and 200 series (right) amps. Both templates correspond to on-cone neutrino signals with E-plane and H-plane angles of 30° for the LPDA response. The chirped response, with the higher frequency components arriving earlier in the pulse, is an outcome of both the antenna dispersion and amplifier group delay, and is characteristic of the system response to an impulse.

Since the cone width decreases with increasing frequency, neutrino signals measured off cone have reduced high frequency content (Figure 5.4). The nature of the Pearson Correlation Coefficient (Section 5.1) dictates that the low frequency oscillations will be the dominant contributor to the cross-correlation.

A similar template matching procedure has also been validated by successfully identifying cosmic rays in the upward facing antennas of ARIANNA's cosmic ray stations [20, 61].

5.1.2 The Neutrino Signal Space

In order to model the sensitivity of the ARIANNA detector, it is first necessary to generate a population of simulated neutrino signals in Monte Carlo. For this purpose, one billion neutrino interactions were simulated in *ShelfMC* with a ESS GZK energy spectrum [62], using a detector configuration matching the currently deployed ARIANNA HRA stations in Moore's Bay, see Table 4.1 for details. This produced a sample of approximately 1.3 million

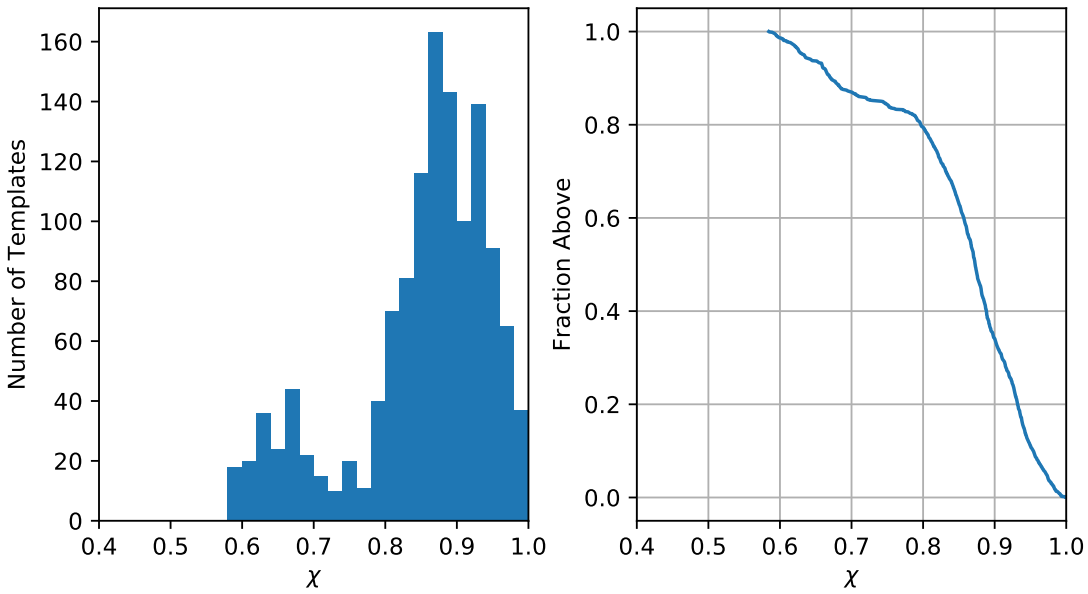

(a)

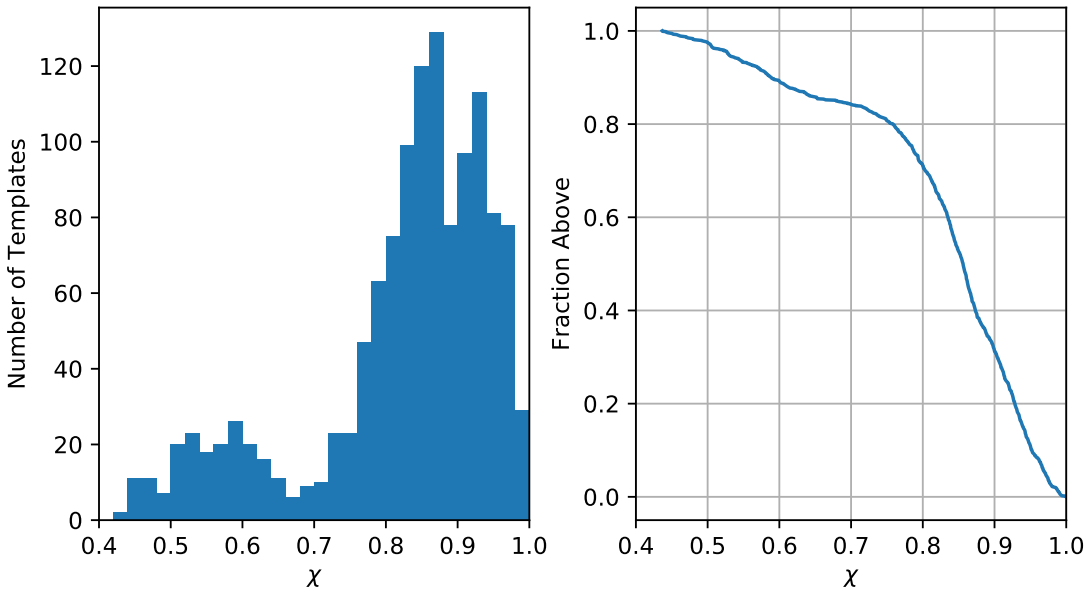

(b)

Figure 5.3: Distribution of cross correlation values between the 100 series (top) and 200 series (bottom) reference templates. The secondary mode at lower χ corresponds to templates with E-plane angle greater than 55°, where the antenna response appears to change rapidly. This is likely due to a node in the LPDA response for high frequencies near an E-plane angle of 55°, apparent in the measurements in [23].

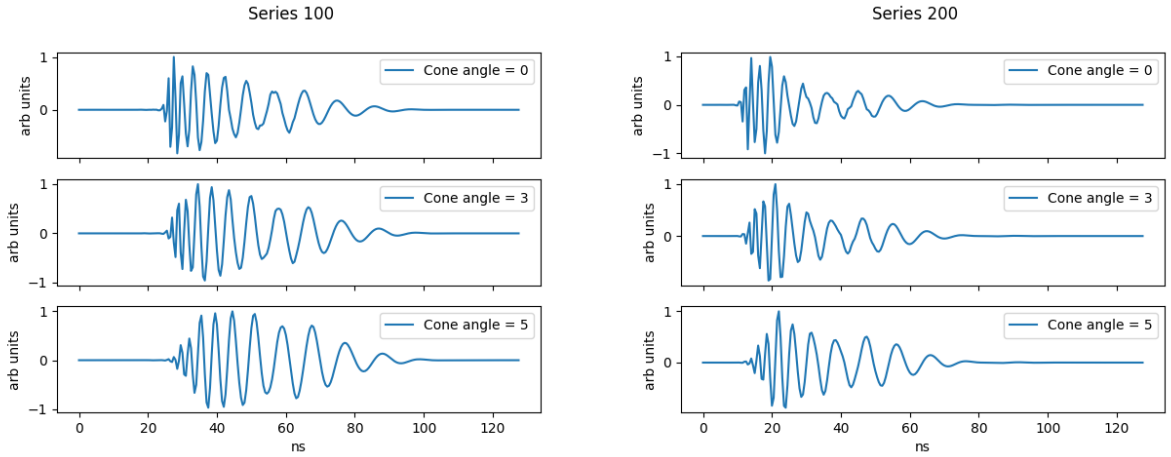

(a) (b)

Figure 5.4: Systematic effect of viewing angle on neutrino templates for 100 series (left) and 200 series (right) amplifiers. The viewing angle relative to the Cherenkov cone is varied, while the E-plane and H-plane angles remain 30°.

events which triggered the simulated station at a 4σ level above the thermal noise V_{rms}.

For each triggered *ShelfMC* event, the arrival direction and polarization relative to the antenna orientation, and the viewing angle relative to the Cherenkov cone are used to choose the most appropriate template. The template is then scaled according to the appropriate amplitude, and finite bandwidth random noise is added. This data is converted to the same format as typical ARIANNA data, and ran through exactly the same algorithms as the triggered events.

5.2 Variables for Analysis

This section will define quantities used to classify events in this analysis. The distributions are presented for the simulated neutrino signal as described in 5.1.2, and for all data from of 1.5 years ARIANNA HRA operation, as shown in taken from December 2015 through April 2017, except for a period from November 9th through December 10th, 2016 when the deployment team was in the field. Data which was taken during periods where the station

communication peripherals were powered on, or while the station was transmitting heartbeat pulses are also omitted from this analysis.

5.2.1 χ Correlation Coefficient

The essential tool in separating potential neutrino signal from background in this analysis is a template matching procedure, so a quantitative measurement of the similarity between two waveforms is required. We will make use of the Pearson Correlation Coefficient [63, 64] (PCC), typically referred to as r.

$$r = \frac{\sum_{i=1}^{n}(x_i - \bar{x})\sum_{i=1}^{n}(y_i - \bar{y})}{\sqrt{\sum_{i=1}^{n}(x_i - \bar{x})^2}\sqrt{\sum_{i=1}^{n}(y_i - \bar{y})^2}} \tag{5.1}$$

Where, in this context, x and y represent two waveforms under comparison, n is the number of samples in the waveforms, and $\bar{x}$ and $\bar{y}$ are the mean values of x and y respectively. The PCC can take values from -1 to 1, where 1 represents perfect positive correlation and -1 represents perfect negative correlation. Values close to 0 represent totally un-correlated waveforms. Since, depending on the arrival direction of the signal relative to the antenna orientation, the measured signal may have reversed polarization relative to the neutrino template, we will only consider the absolute value of r.

Since the PCC is dependent on the alignment of the two waveforms under test, measured waveforms must be shifted relative to each other in time to find the offset which produces the maximum correlation value. To do this, we must zero-pad y such that $y_i = 0$ for

$-n+1 \leq i \leq 0$ and $n+1 \leq i \leq 2n$ so we can define the cross-correlation matrix r_k where:

$$r_k = \frac{\sum_{i=1}^{n}(x_i - \bar{x})\sum_{i=1}^{n}(y_{i-k} - \bar{y})}{\sqrt{\sum_{i=1}^{n}(x_i - \bar{x})^2}\sqrt{\sum_{i=1}^{n}(y_i - \bar{y})^2}} \qquad for \quad -n \leq k \leq n \tag{5.2}$$

A Python function for calculating this matrix can be found in Appendix A.2.

Finally, we can define the quantity $\chi = max(|r_k|)$ to be the maximum Pearson cross-correlation value which we will use for quantifying the similarity of waveforms x_i and y_i. The offset k_{max} which produces the maximum correlation can be used to calculate the most likely time offset Δt_{x-y} between two waveforms through the relation

$$\Delta t_{x-y} = k\delta t \tag{5.3}$$

where δt is the sampling period of the waveforms. This technique is used to calculate the time offsets used in the reconstruction of the signal propagation direction.

For this analysis, χ will refer to the maximum cross-correlation of all input channels against a fixed reference template, as described in Section 5.1.1. The distribution of triggered events in χ (Figure 5.5) shows a significant non-thermal contribution, as compared to min-bias events. The distribution for the neutrino signal is significantly higher than most thermal noise, with it's shape being dictated by the cross-correlation between the reference template and the various templates used to construct the simulated events.

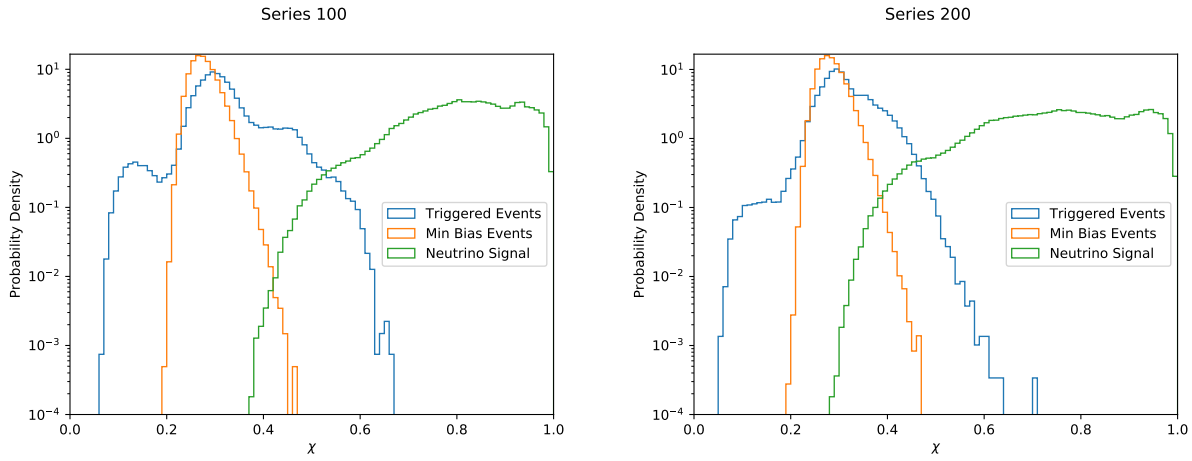

(a) (b)

Figure 5.5: Probability distributions of the max correlation coefficient the reference template (χ) for triggered event, min bias events, and simulated neutrino signal for 100 series and 200 series amps.

5.2.2 L1 Single Frequency Suppression

A significant portion of non-thermal triggers are generated by narrow-band anthropogenic noise. While such background is easily distinguished from broadband neutrino signals in analysis, the amplitudes of these constant wavelength (CW) events are sufficiently high as to induce very high trigger rates in the ARIANNA stations, leading to loss of effective livetime. Therefore, an on-board level 1 trigger was developed to target CW events, which runs on the MBED between event readout and storage.

Since the Moore's Bay site experiences noise from several man-made sources at various frequencies, a single digital notch filter is not sufficient. Therefore, the Level 1 Single Frequency Suppression ratio ($L1$) was developed as a general quantitative filter for CW noise. To calculate $L1$ an FFT is taken of the waveform, generating the Fourier Transform F_i, where the DC bin (F_0) is ignored. $L1$ is then defined as the power in the maximum power FFT bin

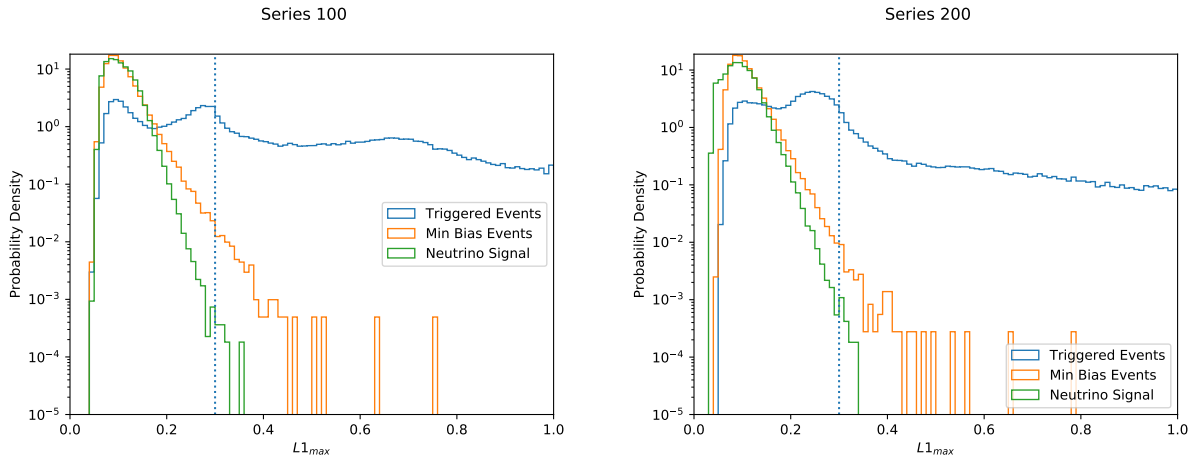

(a) (b)

Figure 5.6: Distributions of simulated neutrino events, as well as HRA data in the $L1$ variable (Eqn. 5.4). The on-board veto of $L1 > 0.3$ is efficient at vetoing narrow band transmitters, while only rejecting 1.8 in 10^5 simulated neutrino signals. Note, since some detector runs do not have the L1 trigger enabled, and some L1 vetoed events are saved for monitoring (scaledown of 50), there are triggered events above the $L1 > 0.3$ threshold.

divided in the total power in all other bins, or

$$L1 = \frac{Power\ in\ Max\ FFT\ Bin}{Total\ Remaining\ Power} = \frac{F_{max}^2}{\sum_{i=1}^{n}[F_i^2]\ -\ F_{max}^2} \tag{5.4}$$

Since the length of the data waveform is known, the FFT can be very quickly calculated using look-up tables, so the calculation of $L1$ can be performed with minimal increases to detector deadtime.

In normal operation, events in which $L1 > 0.3$ for any channel are vetoed before storage. This value was chosen to be highly efficient with regards to the neutrino signal, with only 1.8 in 10^5 simulated neutrino events being rejected, while also being very efficient at rejecting CW noise. Stations are also configured with a scaledown factor of 50, such that 1 out of 50 events vetoed by the $L1$ cut will be sampled in order to monitor the background noise environment.

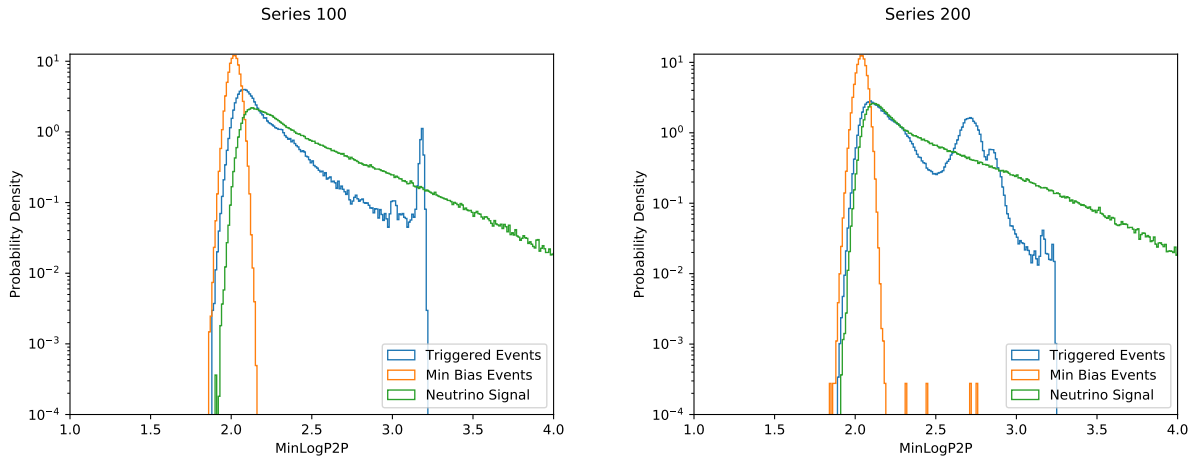

(a) (b)

Figure 5.7: Distributions of amplitudes, measured as $MinLogP2P$, for station data and simulated neutrino signal. The pileup at $MinLogP2P \approx 3.2$, and lack of triggered events with $MinLogP2P > 3.2$ is due to clipping of the amplifiers. Neutrino signal extends well beyond this point because amp model assumes a linear amplitude response. The implications of this will be discusses in Section 5.3.

5.2.3 MinLogP2P Waveform Amplitude

There are several ways to quantify the signal strength of a recorded waveform, and one must be chosen. Here we use the peak-to-peak voltage (V_{P2P}), since this takes into account the unknown polarization of the signal, the fact that the neutrino signal is bi-polar by nature, as well as potential DC offsets. Since each event has a separate V_{P2P} for each channel, there are various ways to combine the measured V_{P2P}'s into a scalar quantity. It was found that the log of the minimum V_{P2P} provided good signal/background separation in the following analysis, so we define

$$MinLogP2P = \min\left(\log_{10}(\frac{V_{P2P}}{\text{mV}})\right) \tag{5.5}$$

5.3 Analysis of Triggered Events

In this section a straw-analysis will be presented, with the goal of estimating the achievable analysis efficiency of a full scale ARIANNA style array. This exercise will develop the tools and methods which will be employed in the forthcoming final analysis of the full > 3 years of operation for the HRA. Surely, more efficient methods of background rejection can and will be developed, so this should be viewed as a conservative evaluation.

The data considered in this analysis consists of ARIANNA HRA taken from December 2015 through April 2017, except for a period from November 9th through December 10th, 2016 when the deployment team was in the field (see Figure 2.19).

5.3.1 Defining the Signal Region

Looking at the distribution of the neutrino signal in χ vs amplitude (figure 5.8), there is a clear trend towards higher χ values with increasing amplitude due to the improved signal-to-noise ratio. For some bin centered on $MinLogP2P_i$ we can find a value of χ_i such that a desired fraction of neutrinos (ϵ_i) will have $\chi > \chi_i$. This is implemented by calculating χ_i on a sliding 0.1 decade bin, creating a smooth contour which represents a preliminary lower bound with a neutrino signal efficiency of $\approx \epsilon_i$. Note that the total signal efficiency ϵ from this method will vary slightly from ϵ_i due to binning effects.

A critical look at the constant efficiency bound in Figure 5.8 shows two main points of improvement. Firstly, since the station's amplifiers clip at ≈ 800 mV, there is a hard cutoff in $MinLogP2P$, as shown in Figure 5.7. In light of this, it is unlikely that neutrino signal with greater amplitudes than this cutoff would reconstruct well to the reference template, and may be very hard to analyze. To account for this, we write off all neutrino signal with $MinLogP2P > 3.2$ which incurs an $\approx 10\%$ penalty on analysis efficiency (see Figure 5.9).

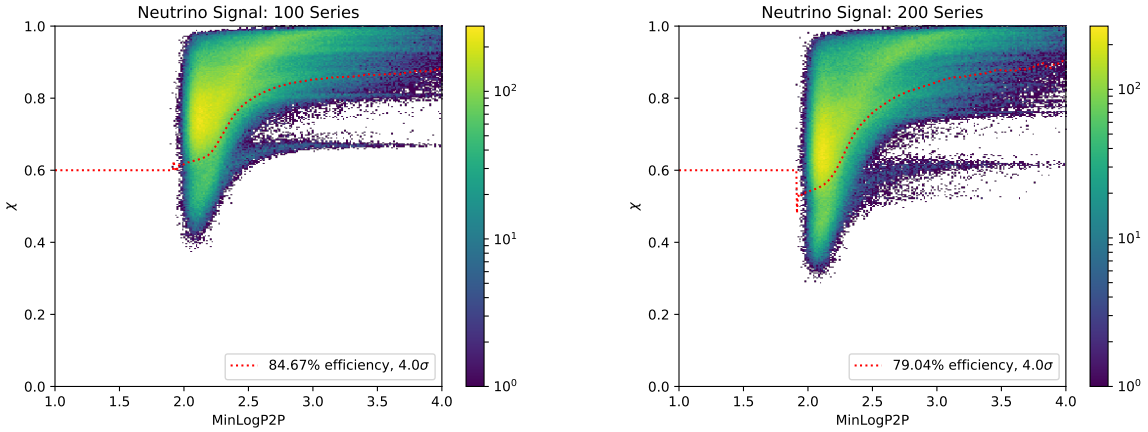

(a) (b)

Figure 5.8: Distribution of simulated neutrino signal in χ vs $MinLogP2P$. Notice that larger values of $MinLogP2P$ correspond to larger values in χ, since lower SNR leads to worse cross-correlation to the reference template. Here, the dashed red line represents a curve of constant analysis efficiency, as discussed in the Section 5.3. This is the starting point, but not the final lower bound used for the analysis, which is shown in 5.11

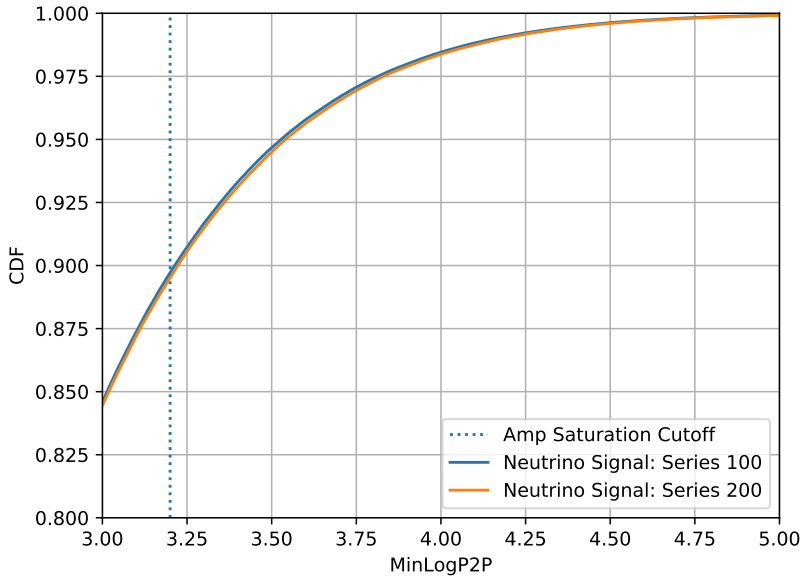

Figure 5.9: Cumulative distribution of the signal amplitude of simulated neutrino events. The maximum cutoff imposed by the saturation of the amps at $\approx 800\,\mathrm{mV}$ corresponds to a 10% loss in signal efficiency. Reducing the loss to 1% would be equivalent to a gain reduction of $\approx 15\,\mathrm{dB}$ and correspond to a thermal noise V_{RMS} of $\approx 3\,\mathrm{mV}$, which would be unacceptably close to the SST system noise.

Secondly, for large amplitude events, the value of χ on the constant efficiency cut is overly conservative. This can be optimized by considering the distribution of triggered events in χ. Looking at the tails of the cumulative sums for the triggered events it is possible to extrapolate a lower bound in χ corresponding to the acceptable number of background events which exceed the cut value (Figure 5.10). Here we have chosen a value of 0.1 events over the time-frame of this analysis for each amplifier type. This process does implicitly assume that there are no as-of-yet undetected sources of rare noise which would modify the shape of the tail.

It is also worth recognizing that these distributions, in addition to the various nuisance backgrounds like narrow-band transmitters and wind-correlated events, also contain cosmic ray air shower events in the LPDA back lobe. These events likely contribute to the shape of the high χ tail (as in the knee in the series 100 amp distribution in Figure 5.10). The addition of upward facing antennas is expected to provide a reliable tag for such events so, in that sense, these bounds are conservative.

With these two refinements, we can set the final signal region lower bound for this analysis (Figure 5.11).

5.3.2 Results

Of all triggered events in this time period, exactly one event remains in the signal region (see Figure 5.12). This event was not associated with a cluster of high-rate wind related events, nor were there any coincident events in any upward-facing antennas of the cosmic ray stations. This lack of a coincidence is not unexpected however, due to the asynchronous nature of the stations, and the fact that only certain cosmic ray footprints have the possibility of triggering multiple stations. Unfortunately, this leaves us unable to verify whether this event was, in fact, due to a cosmic ray (as opposed to an exceedingly (un)lucky neutrino

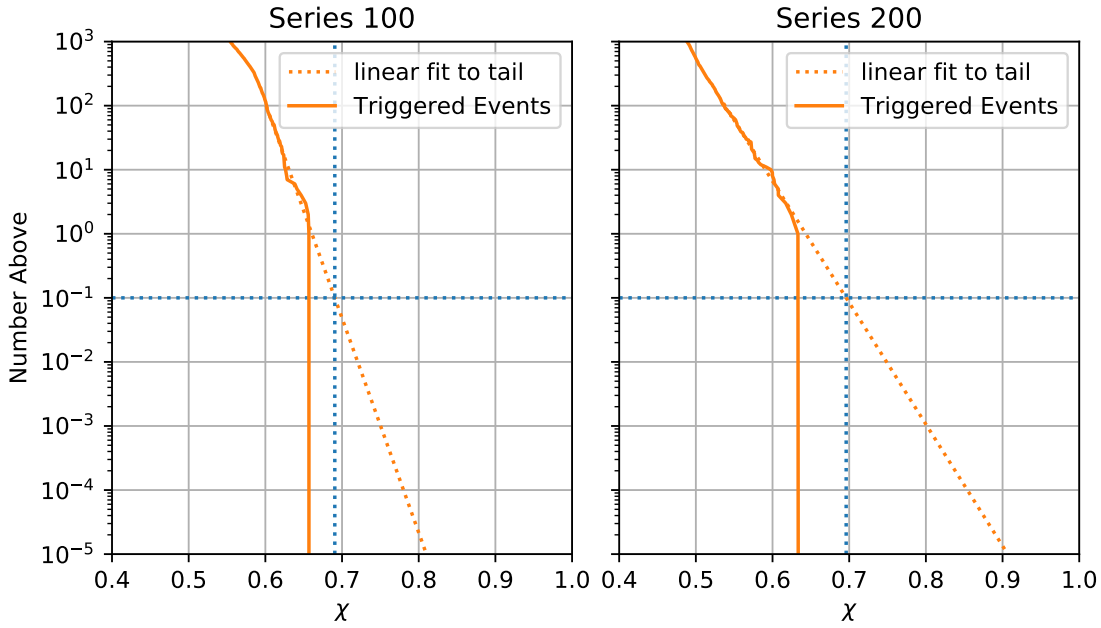

Figure 5.10: The extreme tails of the χ distribution for triggered events, shown as a cumulative sum. The tail is extrapolated by fitting an exponential to the 100 highest χ events, excluding the single highest χ out-lier. χ values of 0.6906 and 0.6960 for 100 series and 200 series amps, respectively, coincide to an expected background of 0.1 event over the time-frame of this analysis.

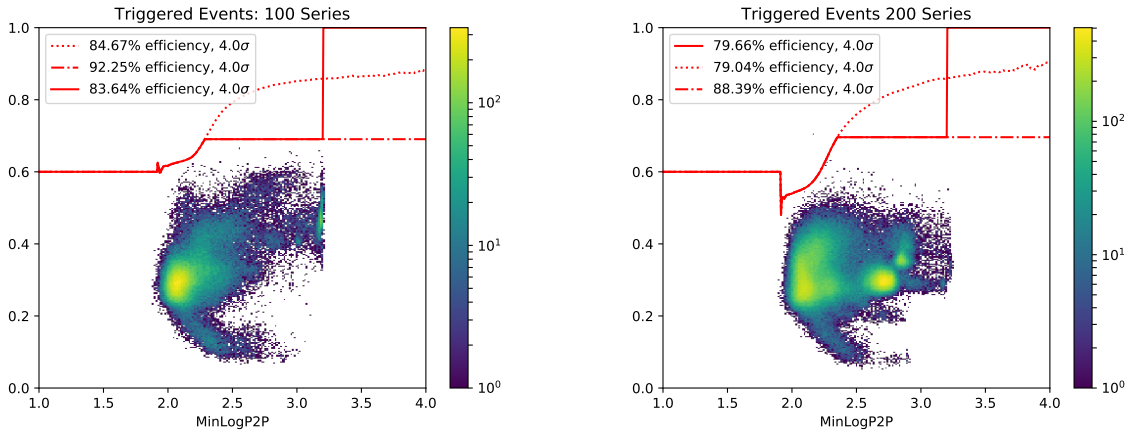

(a) (b)

Figure 5.11: Distribution of all triggered events in ARIANNA HRA stations during the time period of this analysis. The solid red line represents the final signal region lower bound for this analysis, whose derivation is described in the text. The percentages shown in the legend represent the fraction of the simulated neutrino signal which lies in the signal region. There is one thermal trigger event which passes the final cut (black circle), the significance of which will be discussed in the text, and in Figure 5.12.

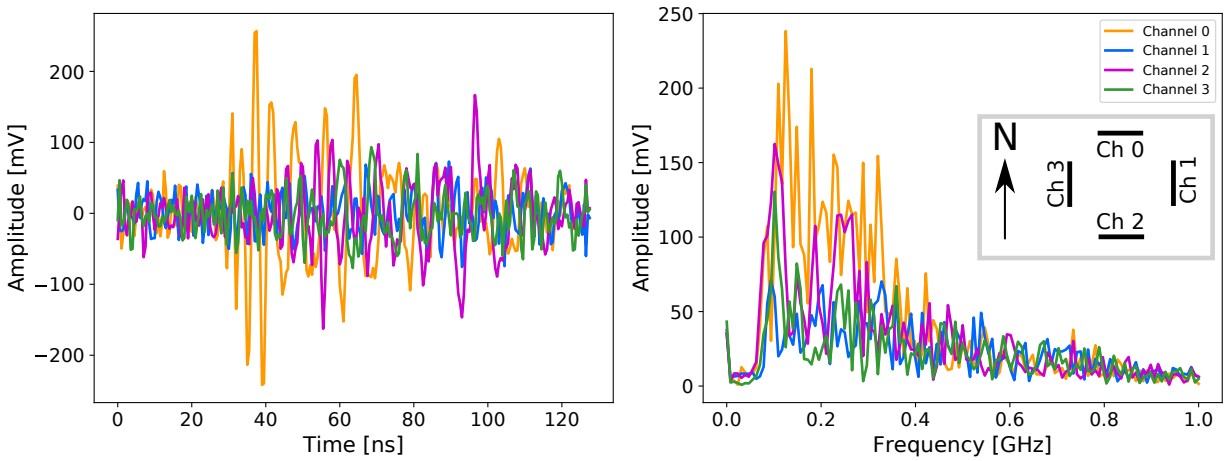

Figure 5.12: Waveform and FFT of the outlying event in Figure **??**. This event has a correlation value of $\chi = 0.71$, and was recorded at ARIANNA Site A at 10:25:03 UTC on March 27$^{\text{th}}$, 2017. The inset shows the positions and polarizations of the LPDA's for each DAq channel.

observation). Of course, this is a problem that was anticipated, and is the justification for the inclusion of upward facing LPDA's.

This outlying event can be compared to some identified comic rays from the HRA, shown in Figure 2.21. The outlying event in Figure 5.12 appears to contain greater high-frequency content compared to the back-lobe cosmic ray waveforms, which likely contributes to its higher value of χ. A careful study of this waveform, combined with a directional reconstruction and deconvolution through the LPDA response may help determine its likely origin, but this analysis is still forthcoming. For now, this highlights the importance of the upward facing channels in a final detector design, which are expected to effectively tag cosmic rays while maintaining greater than 90% efficiency WRT the neutrino signal (see Figure 5.13). While the cosmic ray analysis from the ARIANNA 8 channel cosmic ray station is still ongoing, initial results support this up/down asymmetry in the preliminary cosmic ray sample. A typical cosmic ray event, with $\langle U \rangle - \langle D \rangle = 5.52\sigma$ is shown in Figure 2.28.

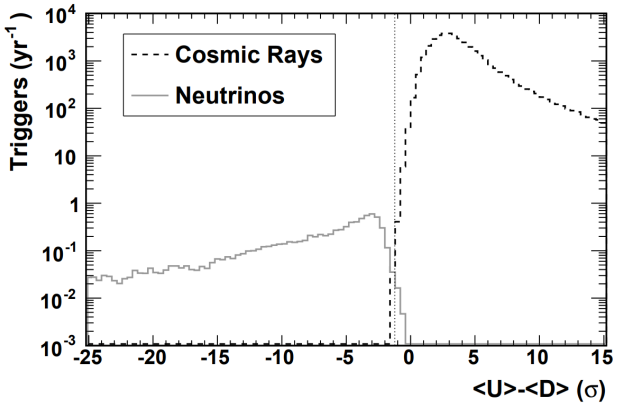

Figure 5.13: Difference in average signal amplitude in upward and downward facing antennas for neutrinos and cosmic rays, from [24]. A cut of $< -1.2\sigma$ maintains 99.7% of the neutrino signal, while reducing the cosmic ray background rate to 0.1 events over a three year run of 1296 ARIANNA stations.

5.4 Flux Limits

Based on the results from 1.5 years of triggered HRA data, and with the justified assumption that cosmic rays will be efficiently tagged by the addition of upward facing LPDA's, we can conclude that an analysis efficiency of 83.64% (based on results from the series 100 amps) is achievable at a 4σ threshold. Inevitably, more efficient analysis techniques will be developed, but we will use this as a conservative starting point to project the sensitivity of a full scale ARIANNA deployment.

5.4.1 Model Independent Flux Limit

Calculation

For some isotropic flux $\Phi(E)$, we can calculate the expected number of events per in an energy bin of a detector as

$$n_i = \Phi(E_i) \cdot Veff\Omega(E_i) \cdot \epsilon t_{live} \cdot dE \ / \ L(E_i) \tag{5.6}$$

where E_i is the energy of the bin, dE is the bin width, $V_{eff}\Omega$ is the effective volume averaged over all flavors, L is the water equivalent interaction length calculated using the cross section in [25], ϵ is the analysis efficiency of the neutrino signal, t_{live} is the total livetime of the detector.

Since the energies of interest span over many orders of magnitude, energy bins are typically in the log scale. Using $dE = \ln 10 \cdot E \cdot d\log_{10} E$ and rearranging, we can derive the following expression for the flux as a function of the measured number of neutrinos.

$$E^2\Phi(E_i) = \frac{n_i}{d\log_{10} E} \frac{E_i L(E_i)}{\ln 10 \ V_{eff}\Omega(E_i) \ \epsilon t_{live}} \tag{5.7}$$

In the absence of observed events and with zero expected background events, we can set a 90% confidence upper limit of 2.44 events in a given energy bin using the Feldman/Cousins approach [65].

$$E^2\Phi(E) \leq \frac{2.44E\ L(E)}{\ln 10\ d\log E\ \epsilon\ V_{eff}\Omega\ t_{live}} \tag{5.8}$$

Performance Projection

We can use the performance of the HRA to inform the key parameters which are required to project a flux limit for a full scale deployment of an ARIANNA style array. The effective volume per station is set by Monte Carlo simulation, but factors such as number of stations and years of deployment are not decided by physics, but by logistics and cost concerns. Other factors, such as the useful station livetime and the analysis efficiency can be conservatively estimated by current results, but are nearly certain to improve in the future.

There is an essentially limitless matrix of possible combinations of station number, trigger thresholds, detector layouts, array locations, etc. For the sake of brevity, we will explore a few illustrative examples. As a starting point, we will assume a 300 station array over a 5 year run. Analysis efficiency will be taken as the demonstrated efficiency of 83.64% for the stations with series 100 amplifiers. A few values for livetime per year will be explored. A summary of the various parameters used for projections are shown in Table 5.1.

Most conservatively, the "As Built" estimate will simply take the demonstrated average livetime of the HRA over 1.5 years of operation.

The "Optimal Solar" estimate will assume a 90% operational efficiency during every day that the sun raises more than 5° above the horizon at Moore's Bay (0.58 of a year). This

Scenario	N Stns.	Years	Type	Thresh.	Loc.	Livetime/Year	ϵ
HRA 3 Year	7	3	HRA 4 Ch	4σ	MB	145 days	81.81%
As Built	300	5	HRA 4 Ch	4σ	MB	145 days	83.64%
Optimal Solar	300	5	HRA 4 Ch	4σ	MB	191 days	83.64%
Optimal Wind	300	5	HRA 4 Ch	4σ	MB	329 days	83.64%
Moore's Bay Combo Solar	300	5	12 Ch Combo	3σ	MB	191 days	83.64%
Moore's Bay Combo Wind	300	5	12 Ch Combo	3σ	MB	329 days	83.64%
South Pole Solar	300	5	12 Ch Combo	3σ	SP	164 days	83.64%
South Pole Grid	300	5	12 Ch Combo	3σ	SP	329 days	83.64%

Table 5.1: Parameters for ARIANNA flux limit projections in Figures 5.14 and 5.15. Justifications for the various livetime estimates are outlined in the text. Abbreviations: MB = Moore's Bay, SP = South Pole.

estimate is justified by the $> 90\%$ livetime efficiency observed during stable opperation of the HRA (Figure 2.19).

The "Optimal Wind" projection assumes the development of a satisfactory wind power system which could allow year-round operation. The stochastic nature of wind patterns makes this a somewhat optimistic projection, but if can serve as a reasonable upper bound for the livetime of an autonomous detector.

Lastly, for comparison, we will construct an "HRA 3 Year" projection based on the demonstrated livetime and efficiency of the 7 stations of the HRA. This will serve as an estimate of a limit which will be calculated from the forthcoming analysis of the full HRA data set.

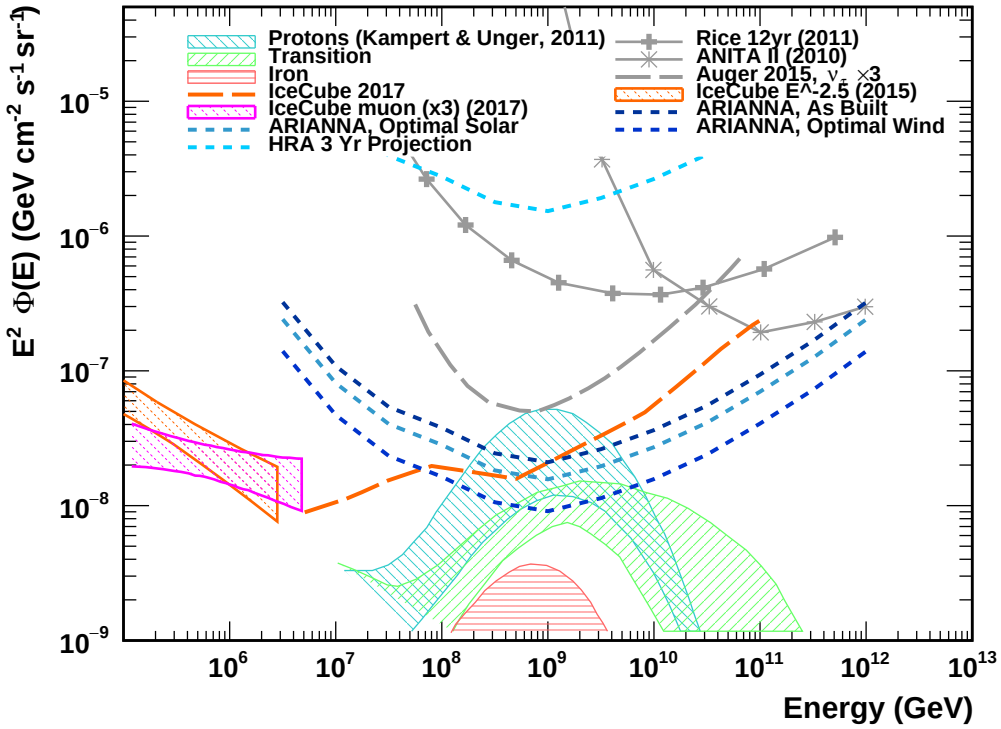

Figure 5.14: Projected flux limits for 5 years of operation of a 300 station ARIANNA array at the Moore's Bay site, as well as a 3 year projection for the HRA pilot array. Input parameters are shown in Table 5.1, with additional details in the text. IceCube spectra from [14, 15]. Icecube limit from [16]. RICE, Auger, and ANITA limits from [17, 18, 19]. Flux models from [12]. For details of the calculation see section 5.4.1.

As discussed in Section 4.2.4, there is potential for an ARIANNA style array located near the South Pole to leverage the ice properties for significantly larger effective volume per station. The 12 channel combo station (Figure 4.11), running at a reduced trigger threshold of 3σ has substantially greater capability compared to the standard HRA station at Moore's Bay, particularly at low energies (Figure 4.10).

One could imagine deploying an array of such stations near the South Pole in two fashions. Such an array could be designed to be autonomous and self powered, similarly to the Moore's Bay design. Solar power would provide reliable power for 50% of the year[2]. In principle this could be extended by employing wind power, but the colder temperatures, calmer winds, and lower atmospheric density at the South Pole conspire to make this a significant challenge relative to Moore's Bay.

A possible extension of livetime for a station near the South Pole could be achieved by cabling into the station's power grid. This would enable reliable year-round operation, essentially doubling the sensitivity of the array. This is illustrated in Figure 5.15.

5.4.2 Model Dependent Normalization and Expected Events

Given some model for the UHE neutrino flux, the expected number of measured events is given by

$$N = \ln 10 \; \epsilon t_{live} \int_{E_{min}}^{E^{max}} \frac{\Phi(E)}{E} \frac{Veff\Omega(E)}{L(E)} \; d\log_{10} E \tag{5.9}$$

[2]At South Pole there is only one sunset per year, so batteries provide negligible additional livetime during the transition from summer to winter.

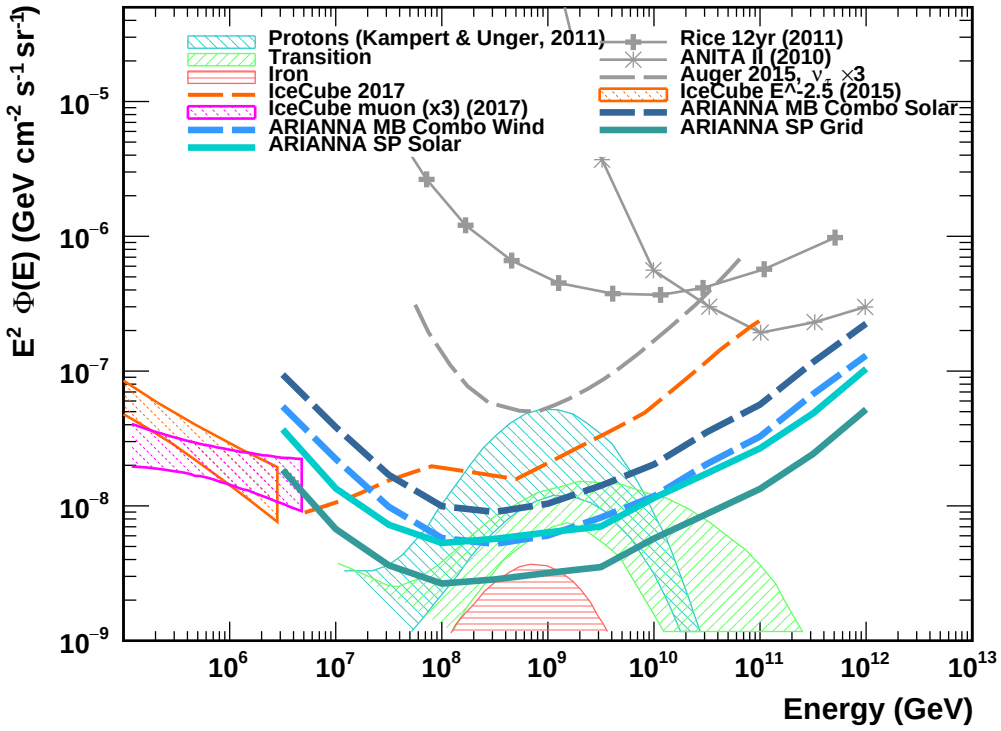

Figure 5.15: Projected flux limits for 5 years of operation of a 300 station ARIANNA arrays. Here we use the effective volume calculated for the optimized 12 channel combo station, with a 3σ trigger threshold. Input parameters are shown in Table 5.1, with additional details in the text.

So for any given flux model, knowing the effective volume, it is possible to project an expected number of events per station per year. Results for a few flux models are shown in Table 5.2. For the GZK flu models, high and low estimates were calculated using the bounds shown in Figures 5.14 and 5.15. For the IceCube power law fluxes, the slope and intercept were randomly varied according to the published uncertainties from [14] and [15] through 10000 iterations, and the high and low estimates for n_ν are taken to be the 1σ inclusive bounds centered at the median value of n_ν.

The IceCube fluxes are reported as

$$\Phi_\nu = \phi \times \left(\frac{E_\nu}{10^5 \,\mathrm{GeV}} \right)^{-\gamma} \tag{5.10}$$

With the $\phi = (2.06^{+0.4}_{-0.3}) \times 10^{-18}\,\mathrm{GeV}^{-1}\mathrm{cm}^{-2}\mathrm{s}^{-1}\mathrm{sr}^{-1}$ and $\gamma = 2.46 \pm 0.12$ for the all flavor flux, and $\phi = (3.03^{+0.78}_{-0.69}) \times 10^{-18}\,\mathrm{GeV}^{-1}\mathrm{cm}^{-2}\mathrm{s}^{-1}\mathrm{sr}^{-1}$ and $\gamma = 2.19 \pm 0.10$ for the ν_μ only flux (multiplied by 3 for comparison to the all flavor models).

The extension of these fluxes to $E = 10^{20.5}\,\mathrm{eV}$ represents a very optimistic picture for the expected number of neutrino detections for an ARIANNA like detector. As time goes on, it may be that an extrapolation of the hard $\nu_\mu \times 3$ flux may be constrained by the UHE all flavor limit from IceCube (see Figure 5.15).

Model	Station	n_ν (low)	n_ν (high)
IceCube all flavor extended [14]	HRA Standard	8.59×10^{-4}	5.29×10^{-3}
	12 Channel Combo	5.09×10^{-3}	2.56×10^{-2}
IceCube $\nu_\mu \times 3$ extended [15]	HRA Standard	3.17×10^{-3}	1.94×10^{-2}
	12 Channel Combo	1.50×10^{-2}	8.04×10^{-2}
Kampert and Unger Proton [12]	HRA Standard	2.55×10^{-3}	1.08×10^{-2}
	12 Channel Combo	9.25×10^{-3}	3.96×10^{-2}
Kampert and Unger Transition [12]	HRA Standard	1.22×10^{-3}	3.41×10^{-3}
	12 Channel Combo	4.24×10^{-3}	1.24×10^{-2}
Kampert and Unger Iron [12]	HRA Standard	6.40×10^{-4}	-
	12 Channel Combo	2.28×10^{-3}	-

Table 5.2: Expected number of neutrinos per station per year (n_ν) for selected isotropic flux models. The HRA Standard station is in Moore's Bay ice with a threshold of 4σ, while the 12 Channel Combo is in South Pole ice with a threshold of 3σ. The GZK fluxes from Kampert and Unger (shown in Figure 5.14) represent a wide range of models for composition, source evolution, etc. No attempt was made to calculate the lower bound for the iron only flux prediction. The estimated number of triggers from the measured IceCube fluxes were taken by extrapolating out to $10^{20.5}$ eV.

5.5 Relating Analysis Efficiency to Signal to Noise Ratio

In the previous sections, it was demonstrated that a simple analysis can reject thermal noise, as well as other backgrounds present as the Moore's Bay site, while maintaining a neutrino signal efficiency of greater than $\approx 85\%$. This is, in part, possible because the operating trigger threshold of 4σ above the thermal noise V_{RMS} ensures that triggered events are maintained above a certain signal to noise ratio (SNR). For template matching techniques, a higher SNR allows for a greater discrimination between the desired signal and background ,and as such, leads to higher analysis efficiency. Conversely, a lower detector threshold increases the number of potential signal events, but these events will have a lower SNR, and diminished analysis efficiency.

This effect is an important counterweight to the increase in effective volume that comes with lower thresholds. There comes a point of diminishing returns, beyond which the real costs

of increased trigger rates, hardware complexity, and data volume out-pace the increase in neutrino events which can reliably be extracted from the background. For an ARIANNA style array which consists of autonomous and independent detectors, the effective volume scales linearly with the number of stations, i.e. cost. Therefore, the increase in effective volume *after* adjusting for analysis efficiency gained by lowering the triggering threshold must increase *greater than* linearly with increased cost in order for the exercise to be justified.

In order to quantify the analysis efficiency as a function of SNR, a set of simulated neutrino events were produced in *ShelfMC*, in much the same way as in Section 5.1.2, except with the trigger threshold reduced to 1.5σ above the thermal noise V_{RMS} (See Table 5.3 for simulation parameters). The arrival direction and signal amplitude calculated in ShelfMC is used in combination with pre-calculated neutrino signal templates and finite-bandwidth random noise in order to create simulated trigger events for analysis.

For this study, we adopt the definition $SNR = |V|_{max}/V_{RMS}$ where $|V|_{max}$ is the maximum absolute amplitude of the signal before noise, taken from Monte Carlo, and V_{RMS} is the thermal noise root-mean-square voltage. Since this definition of SNR matches the trigger in *ShelfMC*, different thresholds values (N_σ) can be considered by simply requiring that $SNR > N_\sigma$.

The resulting simulated neutrino events can be analyzed with the same procedure as the collected data from the ARIANNA HRA, and can be plotted on the $2D$ parameter space generated by χ and $MinLogP2P$, as was done in Section 5.3. As a reminder, χ represents the maximum correlation of any signal channel to a reference neutrino template, which is taken to be at E and H angles of 30° and on the Cherenkov cone, and $MinLogP2P$ is the minimum of $log_{10}(V_{P2P}/mV)$ across all channels. As the threshold is lowered, the low-χ low-$MinLogP2P$ tail extends downward, towards the region which contains thermal noise (Figure 5.16).

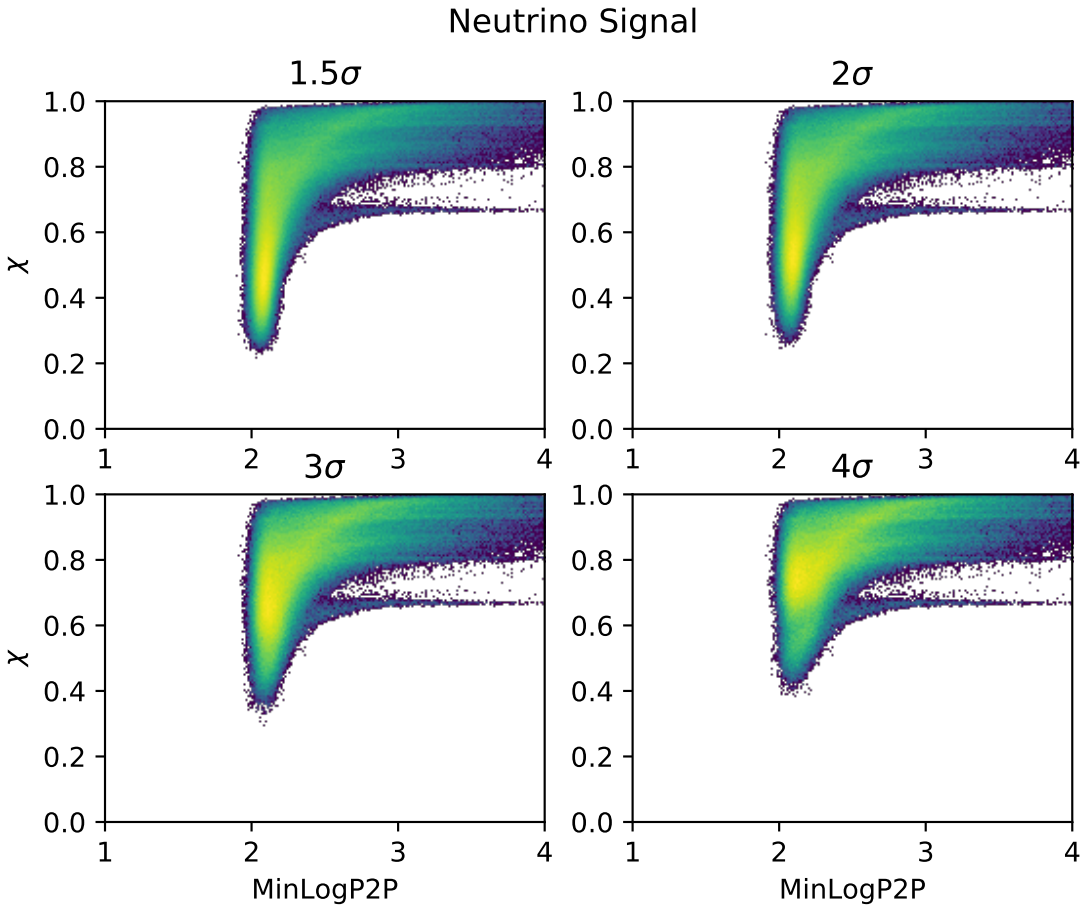

Figure 5.16: The neutrino signal space for various trigger thresholds. The lower SNR events which are accepted by lower trigger thresholds shift the overall distribution to lower χ, reducing the effectiveness of the template matching procedure.

Parameter	Setting
Spectrum	GZK
Energy Range	$10^{16} - 10^{21.5} eV$
Ice Thickness	$575m$
C (see Eqn. 3.3)	$34.48m$
Firn Depth	$68.96m$
Average Attenuation Length	$500m$
Noise Temperature	$350°C$
Bandwidth	$50 - 1000 MHz$
Noise Before Trigger	Disabled
Reflection Coefficient	0.9
Trigger Threshold	1.5σ
Majority Logic	2 of 4
Tau Regeneration	Enabled
Shadowing	Enabled

Table 5.3: *ShelfMC* simulation parameters for the study of analysis efficiency for low SNR events.

We can draw the constant efficiency curves for each trigger threshold with $\epsilon_i = 85\%$ as was done in Section 5.3.1 in order to establish a lower bound for the neutrino signal which can be compared with the distribution of triggered background events. For a 2σ trigger threshold, the $\epsilon_i = 85\%$ inclusive cut is not sufficient to reject the triggered background or min-bias events, so a more restrictive bound must be adopted in order to ensure a pure neutrino signal population (Figures 5.17 and 5.18).

The determination where to set the cutoff boundary for a 2σ trigger threshold is not trivial, since the collected sample of background events is biased by the 4σ threshold used in the operation of the HRA. In principle, there may be unaccounted for sources of noise which lie below the trigger threshold; however, since the SNR of this potential background will be lower than the collected data, it is unlikely that it will have a higher value in χ. Therefore, it is reasonable to extend the low amplitude distribution by chooseing a minimum value for χ which excludes all triggered events at 4σ thresholds, and assume this new *safe* cut will hold for lower thresholds. This will be the cut, shown as the solid red curve in Figures 5.17 and 5.18, used for the calculation of analysis efficiency in this section.

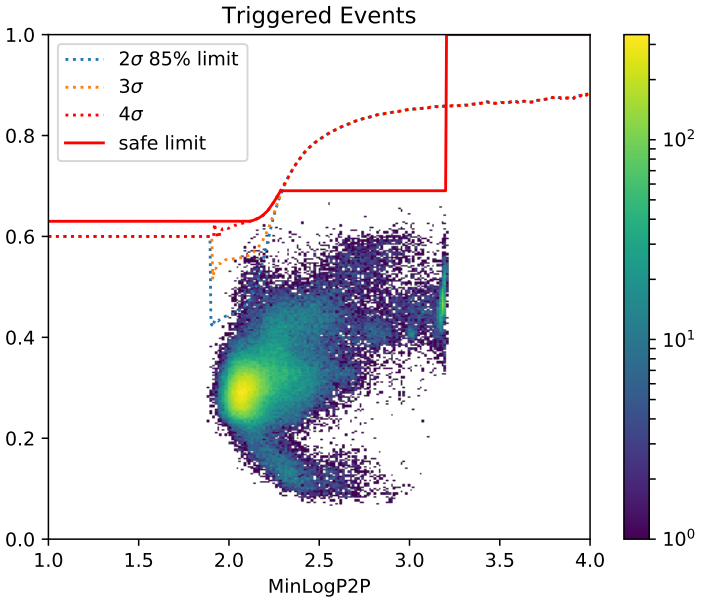

Figure 5.17: All triggered events in ARIANNA HRA stations with 100 series amps. Also showing 85% efficiency cuts for neutrino signals with 2σ, 3σ and 4σ thresholds. Note that only the 4σ and *safe* bounds exclude all background events.

As the threshold is reduced, the number of neutrino events which pass threshold increases rapidly (Figure 5.19a). Naively, one might expect that as the threshold is reduced the maximum radius for a triggering vertex would increase inversely, such that $V_{eff} \propto N_{\sigma}^{-3}$. Two effects prevent this relationship from holding for an ARIANNA type detector. Firstly, the exponential nature of the field attenuation (Equation 3.10) implies that at distances where $r > \ell$ the electric field amplitude will be dominated by attenuation, and the effect of reduced thresholds on V_{eff} will be reduced. Secondly, the shadow zone imposes a strong geometrical constriction on the location of event vertices, effectively masking much of the potential volume.

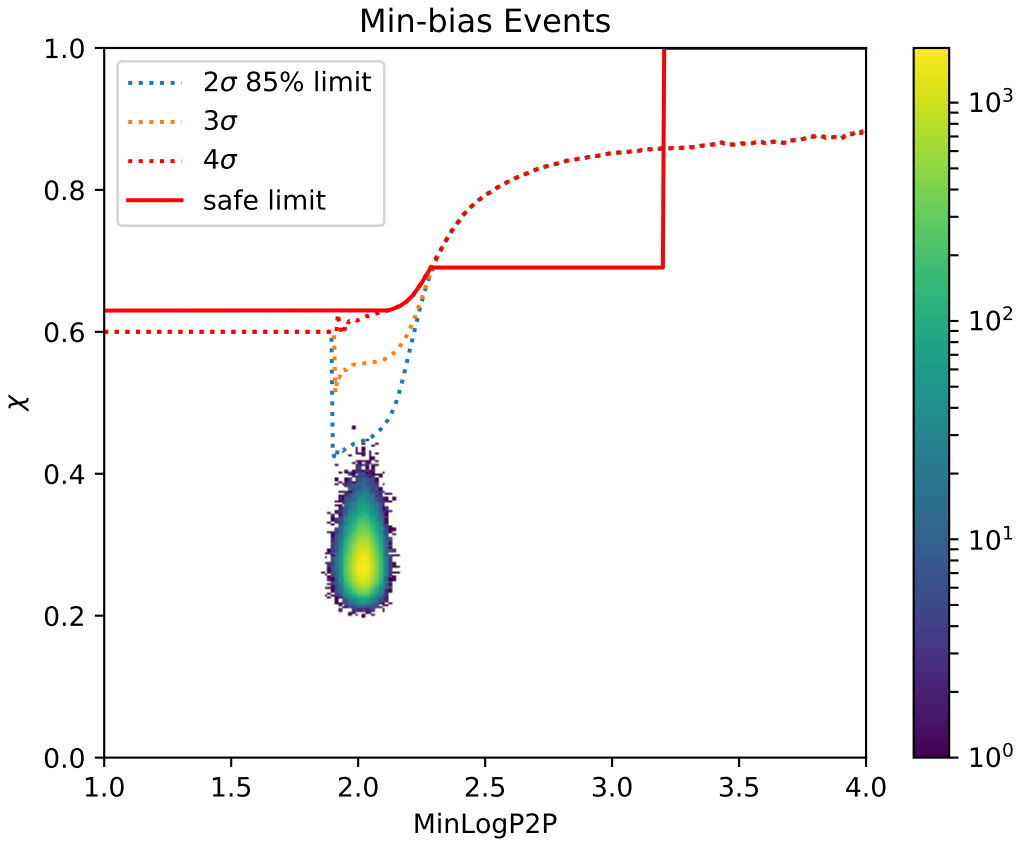

Figure 5.18: All forced trigger events in ARIANNA HRA stations with 100 series amps. Also showing 85% efficiency cuts for neutrino signals with 2σ, 3σ and 4σ thresholds.

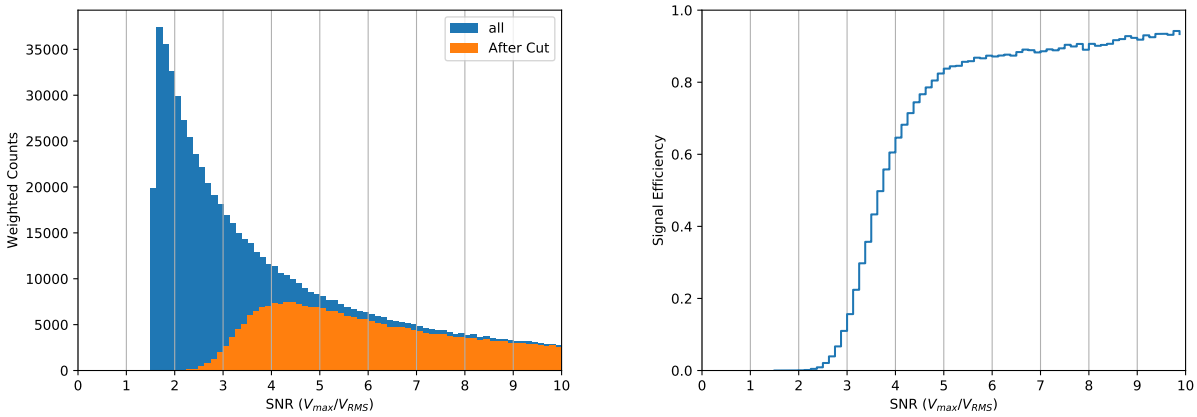

(a) (b)

Figure 5.19: (a) Weighted number of triggered neutrinos as a function of SNR, before and after the background cut (Solid red line in Figure 5.17). (b) Fraction of neutrino events that pass the cut, as a function of SNR. While the number of triggered events increased rapidly with decreasing threshold, the analysis efficiency decreases rapidly, particularly below 4σ.

Since lower energy neutrinos are naturally constrained closer to the detector by their lower implicit signal strength, they are less impacted by these two limiting factors. Therefore, proportionally more low energy neutrino triggers will result from lowering neutrino thresholds (Figure 5.20).

In this analysis, we see that as the SNR falls below 4σ the reduced analysis efficiency begins to out-pace the increase in triggered events brought on by lower thresholds (Figure 5.19a). The signal efficiency as a function of SNR falls to $\approx 10\%$ by $SNR = 3\sigma$, and is essentially negligible by 2σ (Figure 5.19b). This would seem to suggest that the point of diminishing returns, so far as effective volume is concerned, is reached at around 3σ in this analysis.

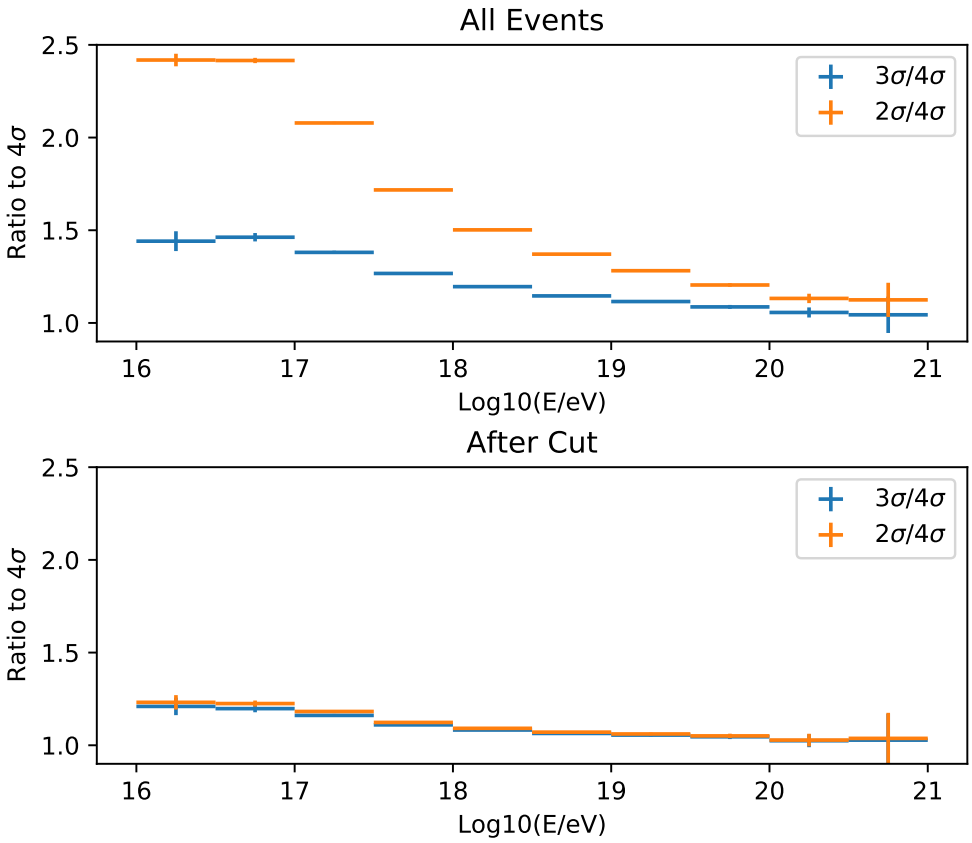

Figure 5.20: Weighted ratio of triggered events at various thresholds to the standard 4σ threshold, as a function of energy. Reducing the trigger threshold can potentially increase the number of triggered events, particularly at low energies, but few of these events pass background rejection in the current template matching analysis.

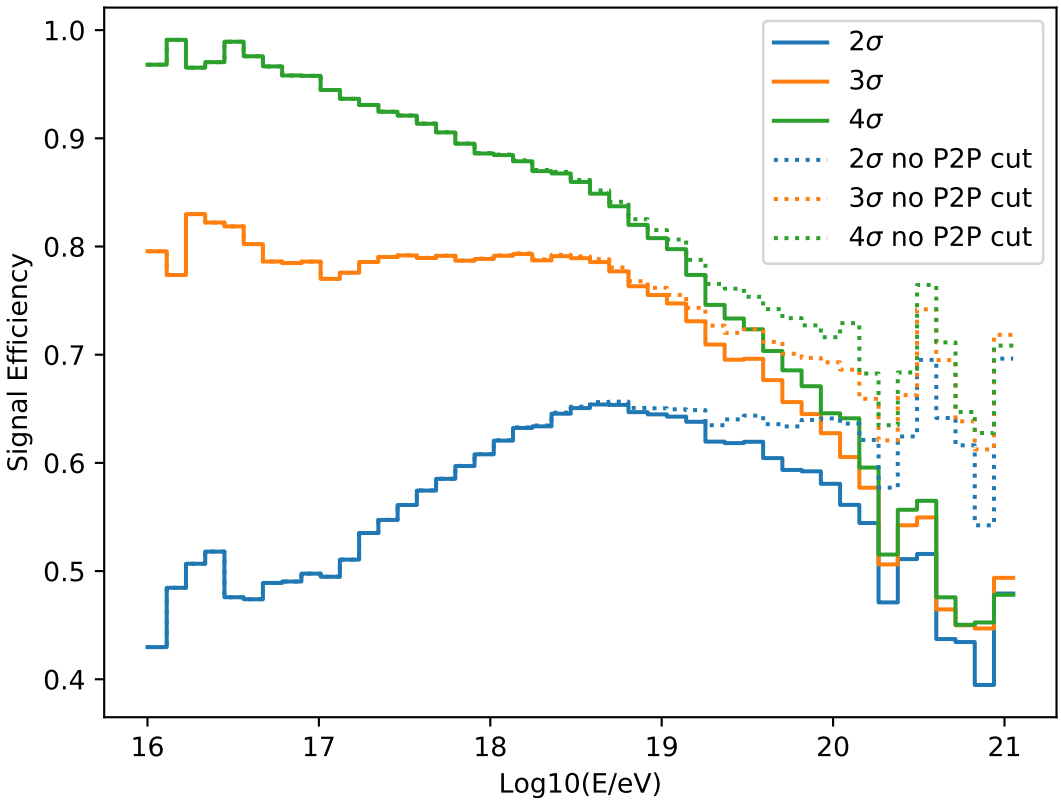

Figure 5.21: Analysis efficiency vs neutrino energy for various trigger thresholds. Solid lines represent events that pass a requirement $MinLogP2P < 3.2$ to account for the saturation of the amps at $\approx 800\,\mathrm{mV}$, while dashed lines do not require this cut.

There is some valid justification for reducing trigger thresholds below the point where reconstructible neutrinos are likely. Recording a greater number of background triggers allows for a more accurate assessment of the background environment, which is important in determining the significance of any events which lie in the signal region. Additionally, as techniques improve, ways of better identifying neutrino signal at lower SNR will inevitably be developed. Therefore, it is important to leave some room for improvement, and not to be unnecessarily limited by detector capabilities.

Chapter 6

Conclusions and Remarks

The ARIANNA pilot Hexagonal Radio Array has demonstrated reliable and stable operation since it's completion in 2014. The stations of the HRA, based on the SST data acquisition system, have demonstrated reliable operation over multiple Antarctic seasons. HRA stations achieved 90% uptime during normal operation while transferring event data to UCI in real time, and have demonstrated an average uptime of 145 days during the 2016-2017 summer season. The streamlined design philosophy of individual and autonomous neutrino detector stations has produced a scalable system, which can serve as a the backbone for a full scale neutrino telescope, capable of deeply challenging (and hopefully measuring) a wide range of models for the GZK neutrino flux.

Long term study of the Moore's Bay site has shown it to be a satisfactory environment for the radio detection of neutrinos. This has been demonstrated most clearly by the straightforward measuring and identification of UHE cosmic ray air showers without the need for an external trigger. Since the stations of the pilot array lack the upward facing antennas planned for the final design, these air showers remain a significant background, but all other noise sources are efficiently distinguished by a simple analysis based on template matching. An analysis of

1.5 years of combined HRA data clearly demonstrates that an analysis efficiency of 83.64% is achievable with a 4σ trigger threshold above V_{RMS}, given that CR air showers are reliably tagged.

Simulation of ARIANNA stations in the improved *ShelfMC* Monte Carlo predict that a relocation of an ARIANNA like array to the South Pole, along with some detector optimizations, should allow a 300 station surface array to meet the science goals of extending the astrophysical neutrino flux measured by IceCube to higher energies, while also achieving new levels of sensitivity to the GZK UHE neutrino flux over a 5 year deployment.

There is much work still to be done.

The HRA has collected over three years of operational data, with the final year's worth still to be processed at the time of this writing. A forthcoming publication will include this additional data into a combined analysis of the complete record from the HRA, which will lead to the penultimate flux limit for the ARIANNA pilot array, as the focus turns to the future.

There is certainly much room for refinement and improvement over the prototype analysis presented here. For instance, the wind-correlated events which are a main source of nuisance background have not been very well studied, and represent a non-thermal background which reduces the efficiency of the analysis. It may be possible to use advanced methods such as machine learning to reliably tag such events, similarly to what was done to classify transient noise in the Advanced LIGO detector [66]. Since ARIANNA and LIGO both use template matching procedures to analyze a time series signal, similar analysis techniques may be fruitful in both.

There are also places where additional hardware development can improve the capability of an ARIANNA like detector. Data transfer is currently a major source of deadtime for the ARIANNA pilot array. Improving the speed and reliability of data transfer could potentially

realize an up to 10% improvement in detector livetime. The addition of double buffering to the SST system would also allow for higher overall trigger rates, enabling better background monitoring and sub-threshold analysis without incurring additional deadtime. The continued development of wind power systems which can survive the Antarctic winter can potentially double the effective livetime of an autonomous detector array.

With a focus on multi-messenger astronomy, a real-time alert system would be an expectation for a full scale UHE neutrino telescope. This will fuel further development in real time analysis and reconstruction of potential neutrino signals. With improved computing capability on station, a preliminary analysis could be done on-board, prioritizing the transfer of promising events to the US for vetting.

Clearly, this is not an exhaustive list of all the challenges and opportunities involved in bringing up a pilot array to a world-class instrument for multi-messenger astronomy. Instead, it should illustrate the promise of this newly emerging field. The first steps have been taken, and they have met with solid purchase. The next steps will follow, and only time will tell how winding this path will be.

Bibliography

[1] A. M. Hillas, *The origin of ultra-high-energy cosmic rays*, *Annual Review of Astronomy and Astrophysics* **22** (sep, 1984) 425–444. https://doi.org/10.1146/annurev.aa.22.090184.002233.

[2] K. Kotera and A. V. Olinto, *The astrophysics of ultrahigh-energy cosmic rays*, *Annual Review of Astronomy and Astrophysics* **49** (sep, 2011) 119–153. https://doi.org/10.1146/annurev-astro-081710-102620.

[3] M. Ahlers and F. Halzen, *Opening a new window onto the universe with IceCube*, *Progress in Particle and Nuclear Physics* **102** (sep, 2018) 73–88. https://doi.org/10.1016/j.ppnp.2018.05.001.

[4] E. Waxman and J. Bahcall, *High energy neutrinos from astrophysical sources: An upper bound*, *Physical Review D* **59** (dec, 1998). https://doi.org/10.1103/physrevd.59.023002.

[5] M. Ackermann et al., *THE SPECTRUM OF ISOTROPIC DIFFUSE GAMMA-RAY EMISSION BETWEEN 100 MeV AND 820 GeV*, *The Astrophysical Journal* **799** (jan, 2015) 86. https://doi.org/10.1088/0004-637x/799/1/86.

[6] I. Valino, *The flux of ultra-high energy cosmic rays after ten years of operation of the pierre auger observatory*, in *Proceedings of The 34th International Cosmic Ray Conference — PoS(ICRC2015)*, Sissa Medialab, aug, 2016. https://doi.org/10.22323/1.236.0271.

[7] K. Fang and B. D. Metzger, *High-energy neutrinos from millisecond magnetars formed from the merger of binary neutron stars*, *The Astrophysical Journal* **849** (nov, 2017) 153. https://doi.org/10.3847/1538-4357/aa8b6a.

[8] A. Albert et al., *Search for high-energy neutrinos from binary neutron star merger GW170817 with ANTARES, IceCube, and the pierre auger observatory*, *The Astrophysical Journal* **850** (nov, 2017) L35. https://doi.org/10.3847/2041-8213/aa9aed.

[9] C. Glaser, "Hunting for cosmogenic neutrinos with the arianna experiment." Poster presented at the Neutrino2018 conference, Heidelberg, Germany, June, 2018. https://zenodo.org/record/1302899.

[10] A. Nelles, S. Buitink, A. Corstanje, J. Enriquez, H. Falcke, J. Hörandel, J. Rachen, L. Rossetto, P. Schellart, O. Scholten, S. ter Veen, S. Thoudam, and T. Trinh, *The radio emission pattern of air showers as measured with LOFAR—a tool for the reconstruction of the energy and the shower maximum*, *Journal of Cosmology and Astroparticle Physics* **2015** (may, 2015) 018–018. https://doi.org/10.1088/1475-7516/2015/05/018.

[11] **ANITA** Collaboration, P. W. Gorham et al., *Observations of the askaryan effect in ice*, *Physical Review Letters* **99** (oct, 2007). https://doi.org/10.1103/physrevlett.99.171101.

[12] K.-H. Kampert and M. Unger, *Measurements of the cosmic ray composition with air shower experiments*, *Astroparticle Physics* **35** (may, 2012) 660–678. https://doi.org/10.1016/j.astropartphys.2012.02.004.

[13] A. Nelles, "ARIANNA: Current developments and understanding the ice for neutrino detection." Talk presented at the ARENA conference, Catania, Italy, June, 2018. https://indico.cern.ch/event/667036/contributions/3004903/.

[14] **IceCube** Collaboration, M. Aartsen et al., *Atmospheric and astrophysical neutrinos above 1 TeV interacting in IceCube*, *Physical Review D* **91** (jan, 2015). https://doi.org/10.1103/physrevd.91.022001.

[15] C. Haack and C. W. and, *A measurement of the diffuse astrophysical muon neutrino flux using eight years of IceCube data.*, in *Proceedings of 35th International Cosmic Ray Conference — PoS(ICRC2017)*, Sissa Medialab, aug, 2017. https://doi.org/10.22323/1.301.1005.

[16] M. Aartsen, *Erratum: Constraints on ultrahigh-energy cosmic-ray sources from a search for neutrinos above 10 PeV with IceCube [phys. rev. lett. 117 , 241101 (2016)]*, *Physical Review Letters* **119** (dec, 2017). https://doi.org/10.1103/physrevlett.119.259902.

[17] **RICE** Collaboration, I. Kravchenko et al., *Updated results from the RICE experiment and future prospects for ultra-high energy neutrino detection at the south pole*, *Physical Review D* **85** (mar, 2012). https://doi.org/10.1103/physrevd.85.062004.

[18] **Pierre Auger Collaboration** Collaboration, A. Aab et al., *Improved limit to the diffuse flux of ultrahigh energy neutrinos from the pierre auger observatory*, *Phys. Rev. D* **91** (May, 2015) 092008. https://link.aps.org/doi/10.1103/PhysRevD.91.092008.

[19] **ANITA** Collaboration, P. W. Gorham et al., *Observational constraints on the ultrahigh energy cosmic neutrino flux from the second flight of the ANITA experiment*, *Physical Review D* **82** (jul, 2010). https://doi.org/10.1103/physrevd.82.022004.

[20] **ARIANNA** Collaboration, S. Barwick et al., *Radio detection of air showers with the ARIANNA experiment on the ross ice shelf*, *Astroparticle Physics* **90** (apr, 2017) 50–68. https://doi.org/10.1016/j.astropartphys.2017.02.003.

[21] *Google Maps*, 2018. [Online; accessed 27-August-2018 https://www.google.com/maps/@-78.3853509,163.1242104,196008m/data=!3m1!1e3].

[22] P. Allison et al., *Design and initial performance of the askaryan radio array prototype EeV neutrino detector at the south pole*, *Astroparticle Physics* **35** (feb, 2012) 457–477. https://doi.org/10.1016/j.astropartphys.2011.11.010.

[23] **ARIANNA** Collaboration, S. W. Barwick et al., *Time-domain response of the ARIANNA detector*, *Astroparticle Physics* **62** (Mar., 2015) 139–151, [arXiv:1406.0820].

[24] **ARIANNA** Collaboration, S. W. Barwick et al., *A first search for cosmogenic neutrinos with the ARIANNA Hexagonal Radio Array*, *Astroparticle Physics* **70** (Oct., 2015) 12–26.

[25] A. Connolly et al., *Calculation of high energy neutrino-nucleon cross sections and uncertainties using the martin-stirling-thorne-watt parton distribution functions and implications for future experiments*, *Physical Review D* **83** (jun, 2011). https://doi.org/10.1103/physrevd.83.113009.

[26] K. Greisen, *End to the cosmic-ray spectrum?*, *Physical Review Letters* **16** (apr, 1966) 748–750. https://doi.org/10.1103/physrevlett.16.748.

[27] G. Zatsepin and V. Kuz'min, *Upper limit of the spectrum of cosmic rays*, *JETP Letters* **4** (1966) 78.

[28] F. W. Stecker, *Ultrahigh Energy Photons, Electrons, and Neutrinos, the Microwave Background, and the Universal Cosmic-Ray Hypothesis*, *Astrophysics and Space Science* **20** (Jan., 1973) 47–57.

[29] M. Aartsen et al., *Flavor ratio of astrophysical neutrinos above 35 TeV in IceCube*, *Physical Review Letters* **114** (apr, 2015). https://doi.org/10.1103/physrevlett.114.171102.

[30] T. I. Collaboration et al., *Multimessenger observations of a flaring blazar coincident with high-energy neutrino IceCube-170922a*, *Science* (jul, 2018) eaat1378. https://doi.org/10.1126/science.aat1378.

[31] T. I. Collaboration, *Neutrino emission from the direction of the blazar TXS 0506+056 prior to the IceCube-170922a alert*, *Science* (jul, 2018) eaat2890. https://doi.org/10.1126/science.aat2890.

[32] B. P. Abbott et al., *Multi-messenger observations of a binary neutron star merger*, *The Astrophysical Journal* **848** (oct, 2017) L12. https://doi.org/10.3847/2041-8213/aa91c9.

[33] G. A. Askar'yan, *Coherent Radio Emission from Cosmic Showers in Air and in Dense Media*, *Soviet Journal of Experimental and Theoretical Physics* **21** (Sept., 1965) 658.

[34] T. Huege, M. Ludwig, and C. W. James, *Simulating radio emission from air showers with CoREAS*, in *American Institute of Physics Conference Series* (R. Lahmann, T. Eberl, K. Graf, C. James, T. Huege, T. Karg, and R. Nahnhauer, eds.), vol. 1535 of *American Institute of Physics Conference Series*, pp. 128–132, May, 2013.

[35] P. W. Gorham, D. P. Saltzberg, P. Schoessow, W. Gai, J. G. Power, R. Konecny, and M. E. Conde, *Radio-frequency measurements of coherent transition and cherenkov radiation: Implications for high-energy neutrino detection*, *Physical Review E* **62** (dec, 2000) 8590–8605. https://doi.org/10.1103/physreve.62.8590.

[36] D. Saltzberg, P. Gorham, D. Walz, C. Field, R. Iverson, A. Odian, G. Resch, P. Schoessow, and D. Williams, *Observation of the askaryan effect: Coherent microwave cherenkov emission from charge asymmetry in high-energy particle cascades*, *Physical Review Letters* **86** (mar, 2001) 2802–2805. https://doi.org/10.1103/physrevlett.86.2802.

[37] P. W. Gorham, D. Saltzberg, R. C. Field, E. Guillian, R. Milinčić, P. Miočinović, D. Walz, and D. Williams, *Accelerator measurements of the askaryan effect in rock salt: A roadmap toward teraton underground neutrino detectors*, *Physical Review D* **72** (jul, 2005). https://doi.org/10.1103/physrevd.72.023002.

[38] P. Miočinović, R. C. Field, P. W. Gorham, E. Guillian, R. Milinčić, D. Saltzberg, D. Walz, and D. Williams, *Time-domain measurement of broadband coherent cherenkov radiation*, *Physical Review D* **74** (aug, 2006). https://doi.org/10.1103/physrevd.74.043002.

[39] J. Abraham et al., *Properties and performance of the prototype instrument for the pierre auger observatory*, *Nuclear Instruments and Methods in Physics Research Section A: Accelerators, Spectrometers, Detectors and Associated Equipment* **523** (may, 2004) 50–95. https://doi.org/10.1016/j.nima.2003.12.012.

[40] **ARIANNA** Collaboration, S. W. Barwick et al., *Design and Performance of the ARIANNA Hexagonal Radio Array Systems*, *IEEE Transactions on Nuclear Science* (2015) [arXiv:1410.7369].

[41] T. Prakash, *A Fully-Synchronous Multi-GHz Analog Waveform Recording And Triggering Circuit*. PhD thesis, University of California, Irvine, 2017. https://escholarship.org/uc/item/5bt060dn.

[42] E. Chiem, *Multi-Gigahertz Synchronous Sampling and Triggering (SST) Circuit with Picosecond Timing Resolution*. PhD thesis, University of California, Irvine, 2017. https://escholarship.org/uc/item/1m29740h.

[43] B. Kolundzija, *Wipl-d: From university software to company product*, in *Proceedings of the 5th European Conference on Antennas and Propagation (EUCAP)*, p. 28442846, 2011.

[44] J. Tatar, *Performance of Sub-Array of ARIANNA Detector Stations during First Year of Operation*. PhD thesis, University of California, Irvine, 2013.

[45] A. Nelles and C. Persichilli, *Livetime and sensitivity of the ARIANNA hexagonal radio array*, in *Proceedings of the International Cosmic Ray Conference*, (The Hague, The Netherlands), 2015. http://arxiv.org/pdf/1509.00115.

[46] C. P. for the ARIANNA Collaboration, *Radio search for EHE neutrinos with the ARIANNA pilot array, and ARIANNA performance projections*, in *Proceedings of the International Cosmic Ray Conference*, (Busan, South Korea), 2017. PoS(ICRC2017)977.

[47] C.J. Reed for the ARIANNA Collaboration, *Performance of the Completed ARIANNA Hexagonal Radio Array*, *Proceedings of the International Cosmic Ray Conference* (2015).

[48] S. Wang et al., for the ARIANNA Collaboration, *Calibration, Performance, and Cosmic Ray Detection of ARIANNA-HCR Prototype Station*, in *Proceedings of the International Cosmic Ray Conference*, (Busan, South Korea), 2017. PoS(ICRC2017)358.

[49] K. Dookayka, *Characterizing the Search for Ultra-High Energy Neutrinos with the ARIANNA Detector*. PhD thesis, University of California, Irvine, 2011.

[50] J. Alvarez-Muñiz and E. Zas, *Cherenkov radio pulses from EeV neutrino interactions: the LPM effect*, *Physics Letters B* **411** (oct, 1997) 218–224. https://doi.org/10.1016/s0370-2693(97)01009-5.

[51] D. Besson et al., *In situ radioglaciological measurements near taylor dome, antarctica and implications for ultra-high energy (UHE) neutrino astronomy*, *Astroparticle Physics* **29** (mar, 2008) 130–157. https://doi.org/10.1016/j.astropartphys.2007.12.004.

[52] J. C. Hanson et al., *Radar absorption, basal reflection, thickness and polarization measurements from the ross ice shelf, antarctica*, *Journal of Glaciology* **61** (2015), no. 227 438–446. https://doi.org/10.3189/2015jog14j214.

[53] F. Wu, *Using ANITA-I to constrain ultra high energy neutrino-nucleon cross section*. PhD thesis, University of California, Irvine, 2009.

[54] S. Barwick, E. Berg, D. Besson, G. Gaswint, C. Glaser, A. Hallgren, J. Hanson, S. Klein, S. Kleinfelder, L. Köpke, I. Kravchenko, R. Lahmann, U. Latif, J. Nam, A. Nelles, C. Persichilli, P. Sandstrom, J. Tatar, and E. Unger, *Observation of classically `forbidden' electromagnetic wave propagation and implications for neutrino detection.*, *Journal of Cosmology and Astroparticle Physics* **2018** (jul, 2018) 055–055. https://doi.org/10.1088/1475-7516/2018/07/055.

[55] J. Alvarez-Muñiz, R. A. Vázquez, and E. Zas, *Calculation methods for radio pulses from high energy showers*, *Physical Review D* **62** (aug, 2000). https://doi.org/10.1103/physrevd.62.063001.

[56] E. Zas, F. Halzen, and T. Stanev, *Electromagnetic pulses from high-energy showers: Implications for neutrino detection*, *Phys. Rev. D* **45** (Jan, 1992) 362–376. https://link.aps.org/doi/10.1103/PhysRevD.45.362.

[57] J. Alvarez-Muñiz and E. Zas, *The LPM effect for EeV hadronic showers in ice: implications for radio detection of neutrinos*, *Physics Letters B* **434** (aug, 1998) 396–406. https://doi.org/10.1016/s0370-2693(98)00905-8.

[58] T. DeYoung, S. Razzaque, and D. Cowen, *Astrophysical tau neutrino detection in kilometer-scale cherenkov detectors via muonic tau decay*, *Astroparticle Physics* **27** (apr, 2007) 238–243. https://doi.org/10.1016/j.astropartphys.2006.11.003.

[59] F. Halzen and D. Saltzberg, *Tau neutrino appearance with a 1000 megaparsec baseline*, *Physical Review Letters* **81** (nov, 1998) 4305–4308. https://doi.org/10.1103/physrevlett.81.4305.

[60] J. Alvarez-Muñiz, A. Romero-Wolf, and E. Zas, *Practical and accurate calculations of askaryan radiation*, *Physical Review D* **84** (nov, 2011). https://doi.org/10.1103/physrevd.84.103003.

[61] A. Nelles for the ARIANNA Collaboration, *Cosmic-ray capabilities of the ARIANNA neutrino experiment*, in *Proceedings of the International Cosmic Ray Conference*, (Busan, South Korea), 2017. PoS(ICRC2017)399.

[62] R. Engel, D. Seckel, and T. Stanev, *Neutrinos from propagation of ultrahigh energy protons*, *Physical Review D* **64** (oct, 2001). https://doi.org/10.1103/physrevd.64.093010.

[63] Wikipedia contributors, *Pearson correlation coefficient — Wikipedia, the free encyclopedia*, 2018. [Online; accessed 25-August-2018 https://en.wikipedia.org/wiki/Pearson_correlation_coefficient].

[64] *Statistics Glossary: P — Electronic Statistics Textbook*, 2013. [Online; accessed 25-August-2018 http://www.statsoft.com/textbook/glosp.html#Pearson%20Correlation].

[65] G. J. Feldman and R. D. Cousins, *Unified approach to the classical statistical analysis of small signals*, *Physical Review D* **57** (apr, 1998) 3873–3889. https://doi.org/10.1103/physrevd.57.3873.

[66] J. Powell, D. Trifirò, E. Cuoco, I. S. Heng, and M. Cavaglià, *Classification methods for noise transients in advanced gravitational-wave detectors*, *Classical and Quantum Gravity* **32** (oct, 2015) 215012. https://doi.org/10.1088/0264-9381/32/21/215012.

Appendix A

Code Snippets

A.1 Python Code for Calculating Askaryan Emission in Ice

```
import numpy as np

def ShelfMCAskaryan(energy, theta, freqs, is_em_shower, n_index, R
    ):

    #ShelfMC Global Parameters
    X0ICE = 0.403
    ECICE = 63.7
    NICE = 1.78
    AEX_ICE = 1.
    JAIME_FACTOR = 1
    ALOG2 = 0.693147
```

```
LPM = is_em_shower

X0DEPTH = X0ICE
ECDEPTH = ECICE
NDEPTH = n_index
AEXDEPTH = AEX_ICE
changle = np.arccos(1 / n_index)
pnu = energy #in eV

nu0 = 1150.
nu0_modified = nu0 * (X0ICE / ECICE) / (X0DEPTH / ECDEPTH) *
    (1 / np.sqrt(NDEPTH * NDEPTH - 1.)) / (1 / np.sqrt(NICE *
    NICE - 1.))

factor = 1 / np.sqrt(1 - 1 / (NICE * NICE)) * 1 / nu0 *
    X0DEPTH / X0ICE *ECICE / ECDEPTH * AEXDEPTH / AEX_ICE

vmmhz1m = factor * (2.53E-7) * (pnu / 1.E12) * freqs * (1. /
    (1. + np.power(freqs / nu0_modified, 1.44))) * JAIME_FACTOR

vmmhz1m /= np.sqrt(2.)

vmmhz1m *= np.sin(theta) / np.sin(changle)

showerlength = 3.1
elpm = 2.E15 * (X0DEPTH / X0ICE)
nu0 = 500.E6 / 1.E6 * X0ICE / X0DEPTH
```

```
eshower = pnu
n_depth = n_index

if is_em_shower:

    if (eshower < elpm) or (LPM==False):
        showerlength /= np.power((eshower / elpm), -0.03)
    else:
        showerlength /= np.power(elpm / (0.14 * (eshower) +
           elpm), 0.3)

    deltheta = 12.32 / np.sqrt(np.power(n_depth, 2) - 1) * (
       nu0 / freqs) * np.deg2rad(1) / showerlength

else:
    epsilon = np.log10(eshower / 1.E12)
    if (eshower >= 1E12 and eshower < 100.E12):
        deltheta = 1.473 / np.sqrt(np.power(n_depth, 2) - 1) *
            nu0 / freqs * np.deg2rad(1) * (2.07 - 0.33 *
           epsilon + (7.5e-2) * epsilon * epsilon)
    elif (eshower < 100.E15):
        deltheta = 1.473 / np.sqrt(np.power(n_depth, 2) - 1) *
            nu0 / freqs * np.deg2rad(1) * (1.744 - (1.21e-2) *
            epsilon)
    elif (eshower < 10.E18):
        deltheta = 1.473 / np.sqrt(np.power(n_depth, 2) - 1) *
            nu0 / freqs * np.deg2rad(1) * (4.23 - 0.785 *
```

```
                epsilon + (5.5e-2) * epsilon * epsilon)
        else:
            deltheta = 1.473 / np.sqrt(np.power(n_depth, 2) - 1) *
                nu0 / freqs * np.deg2rad(1) * (4.23 - 0.785 * 7. +
                5.5e-2 * 49.)
            deltheta = deltheta * (1. + (epsilon - 7.) * 0.075)

    dangle = theta - changle
    #print('deltheta = {}'.format(deltheta))
    #print('dangle = {}'.format(dangle))
    vmmhz1m = vmmhz1m * np.exp(-ALOG2 *  dangle*dangle / (deltheta
        *deltheta))

    return vmmhz1m/R
```

A.2 Python Code for the Pearson cross-correlation

```
import numpy

def pearsonr_correlate(x,y,mode='full'):
    '''
    args
    x, y: array-like
        input sequences
    mode: {valid, same, full}, optional
        refer to documentation for numpy.correlate.  default is '
            full'
```

```
    returns: array
        discrete cross-correlation using the Pearson Correlation
            with values -1 - 1
    ref:
        http://www.statsoft.com/textbook/glosp.html#Pearson%20
            Correlation
    '''

    #subtract the means from each input sequences
    x_sub = numpy.array(x) - numpy.mean(x)
    y_sub = numpy.array(y) - numpy.mean(y)

    #find cross-correlation of mean-subtracted arrays
    corr = numpy.correlate(x_sub,y_sub,mode=mode)

    #normalize the distribution
    corr /= numpy.sqrt(numpy.sum(numpy.square(x_sub))*numpy.sum(
        numpy.square(y_sub)))

    return corr
```